Ministry of Higher Education and Scientific Research
University of Baghdad
Institute of Laser for Postgraduate Studies

Investigation of Thermal Gradient in Tumors Subjected to Nano-Antenna Assisted Laser Processing

A Thesis Submitted to the Institute of Laser for Postgraduate Studies, University of Baghdad in Partial Fulfillment of the Requirements for the Degree of Doctor of Philosophy in Laser / Electronic and Communication Engineering

by

Rasha Hashim Mahdi

B. Sc. Laser and Optoelectronics Engineering - 2010

M. Sc. Laser and Optoelectronics Engineering - 2014

Supervisor

Asst. Prof. Dr. Hussein Ali Jawad

2019 AD 1440 AH

Ministry of Higher Education and Scientific Research
University of Baghdad
Institute of Laser for Postgraduate Studies

Investigation of Thermal Gradient in Tumors Subjected to Nano-Antenna Assisted Laser Processing

A Thesis Submitted to the Institute of Laser for Postgraduate Studies, University of Baghdad in Partial Fulfillment of the Requirements for the Degree of Doctor of Philosophy in Laser / Electronic and Communication Engineering

by

Rasha Hashim Mahdi

B. Sc. Laser and Optoelectronics Engineering - 2010

M. Sc. Laser and Optoelectronics Engineering - 2014

Supervisor

Asst. Prof. Dr. Hussein Ali Jawad

2019 AD **1440 AH**

بسم الله الرحمن الرحيم

"قالُواْ سُبْحَانَكَ لاَ عِلْمَ لَنَا إِلاَّ مَا عَلَّمْتَنَا إِنَّكَ أَنتَ الْعَلِيمُ الْحَكِيمُ"

صدق الله العظيم

سـورة البقرة – الأيـة ٣٢

Certification

I certify that this thesis was prepared under our supervision at the Institute of Laser for Postgraduate Studies, University of Baghdad, in partial fulfillment of requirements for the degree of a Doctor of Philosophy in Laser/ Electronic and Communication Engineering.

Signature: Hussa.

Name: **Dr. Hussein Ali Jawad**

Title: Assistant Professor

Address: Institute of laser for postgraduate studies,

University of Baghdad

Date: 16/ 7/ 2019

(Supervisor)

In view of the available recommendation, I forward this thesis for debate by Examining Committee.

Signature: Hanan

Name: **Asst. Prof. Dr. Hanan Jaafer Taher**

Title: Head of the Scientific Committee.

Address: Institute of Laser for Postgraduate Studies,

University of Baghdad.

Date: 17/ 7/ 2019

Examination Committee Certificate

We certify that we have read this thesis "Investigation of Thermal Gradiant in Tumors Subjected to Nano-Antenna Assisted Laser Processing" and as examination committee we examined the student in its contents and in our opinion it is adequate with standards as a thesis for the degree of Doctor of Philosophy in Laser/ Electronic and Communication Engineering.

Signature:
Name: **Dr. Abdul Hadi M. Al-Janabi**
Title: Professor
Address: Institute of Laser for Postgraduate Studies, University of Baghdad.
Date: 25/12/2019
(Chairman)

Signature:
Name: **Dr. Raad Sami Fyath**
Title: Professor
Address: College of Engineering, Al-Nahrain University.
Date: 25/12/2019
(Member)

Signature:
Name: **Dr. yasin Yousif Muhammad**
Title: Assistant Professor
Address: College of Engineering, Al-Mustansiriyah University.
Date: 17/12/2019
(Member)

Signature:
Name: **Dr. Anas Ail Hussien**
Title: Assistant Professor
Address: College of Engineering, Al-Nahrain University.
Date: 15/12/2019
(Member)

Signature:
Name: **Dr. Tahreer Safaa Mansour**
Title: Assistant Professor
Address: Institute of Laser for Postgraduate Studies, University of Baghdad
Date: / /2019
(Member)

Signature:
Name: **Dr. Hussein Ali Jawad**
Title: Assistant Professor
Address: Institute of Laser for Postgraduate Studies, University of Baghdad
Date: 15/12/2019
(Supervisor)

Approved by the deanship of Institute of Laser for Postgraduate Studies, University of Baghdad

Signature:
Name: **Dr. Hussein Ali Jawad**
Title: Dean
Address: Institute of Laser for Postgraduate Studies, University of Baghdad.
Date: 26/12/2019

Dedication

To ... my Parents who care for me and made it possible to complete this work.

To ... my four sisters Rawaa, Yassmin, Zaineb, and Nooralhuda for all their support.

To ... my two brothers Zaid and Ali who are always beside me.

Rasha Hashim Mahdi

2019

Acknowledgment

I would like to express my sincere appreciation and thanks to my supervisor **Assistant Prof. Hussein Ali Jawad** for his thoughtful guidance, continuous support and unwavering encouragement during this work.

I would also like to thank the dean of the Institute of Laser for postgraduate studies **Prof. Abdul Hadi M. Al-Janabi** for his help and support during the Ph.D. courses and after.

I am thankful for **Asst. Prof Dr. Ziad Ayad Taha**, former head of the Engineering and Industrial Applications Branch and **Asst. Prof. Dr. Mohamed K. Dhahir**, the current head of the Branch for their support during my research work.

Also, Special thanks to all members of my institute.

Finally, I am deeply grateful to my family for all their support and encouragement over the years.

Abstract

Opto-thermal therapy of live tissues faces sophisticated obstacles due to the confinement of the light sources in a side and the nature of tissue cells in another. Serious attempts are accomplished to overcome partially this issue especially using lasers directly on the diseased tissue which represents the advance in this field of application, but it is still restricted by the diffraction limit while dimensions of the cells in the subwavelength scale. It is worth to mention that the absorption is the penetration depth dependent for a certain tissue. Plasmonic nano-antenna is a convenient candidate because of its ability to generate optical high field intensity in nano-dimensions. The computer simulation technology studio suite packaged version(2017, 2018 and 2019) was used to carry out the design of both nano-antennas and the proposed skin tissue. Gold nano-structure and silicon carbide dioxide are the material used in the design of Bowtie shape. Two wavelengths (532 and 1064) nm, which are the wavelengths of Nd:YAG laser and its second harmonic were examined because they represent the superficial and deep skin absorption respectively. The design includes single and pairs of bowtie shaped array (2×2, 3×3 and 4×4) structures, in addition, half wavelength distance between two adjacent gap antennas also considered for array samples. All designs were subjected to particle swarm optimization and sweeping processes. Parametric studies for all designed samples are done. The performance of all samples including reflectivity, near-field, and far-field are accomplished for both wavelengths. The time period in the irradiated tissues that is required to killing tumor cells was estimated via the calculation of the specific absorption rate. The results showed that the maximum reflectivity of the optimized single nano-antenna at the resonance wavelength 532 nm is (-50.57 dB), while the higher reflectivity is (-58.39 dB) for half wavelength antennas, clear variations of reflectivity were observed with an enhancement in some arrays but the resonance wavelengths

are shifted. Red shift with higher reflectivity was detected for an array of two pairs for 532 nm and reduced for more than a couple of pairs. The near-field measurements revealed that the intensity fields is the higher (3.27×10^{8} V/m) at 532 nm for single nano-antennas while in array structures, the field intensity is more enhanced for the half wavelength array (3×3) at 1064 nm (7.47×10^{8} V/m). The sharper and higher far-field distribution is observed at 532 nm of (7.79×10^{6} V/m). The far-field is enhanced for both wavelengths using array structures related to the single unit while more effect is observed in the case of half wavelength (2.54×10^{7} V/m) at 1064 nm. The field intensity is more effective at a closer distance (100 nm) where it is (1.3×10^{8} V/m) at 532 nm while at half wavelength (4×4) array (3.04×10^{8} V/m) is the higher. The maximum surface absorption rate is (2.2×10^{11} W/kg) for single antenna for(100 nm) at resonance wavelength 1064 nm and the highest is detected for the half wavelength structures (5.31×10^{11} W/kg) at 532 nm. The calculated time period desired to destroy the tumor cell is shorter at the closer distance (100 nm) from the tissue. The shorter time period for a single unit is (5.26 μs) at 1064 nm while (1.42 μs) for (2×2) array at 532 nm.

LIST OF CONTENTS

CONTENTS	PAGE
Chapter Two: Design Methodology of a Proposed Nano-Antenna and Skin Tissue Model	

LIST OF SYMBOLS

SYMBOLS	DESCRIPTION	UNITS
ε	permittivity	F/m
ω	angular frequency	rad/sec
τ	mean free time of free electron	sec
ω_ρ	plasma frequency	rad/sec
E	electric field	V/m
B	flux density	T
H	magnetic field	A/m
D	dielectric displacement	C/m^2
μ	permeability	H/m
k	wave vector	1/m
t	time	sec
ξ	PSO function	-
$x_{a,j}$	position of particle a, at time t	-
$v_{a,j}$	velocity of particle a, at time t	m/sec
$y_{a,j}$	personal best position of particle a, at time t	-
F	fitness function	-
w	iteration weight	-
c	acceleration constants	-
r	random variable	-
c	speed of light	m/sec
β	phase shift	rad/sec
α	attenuation	dB/cm
n	real part of complex index	-
k	imaginary part of complex index	-
N	complex index	-
σ	conductivity	S/m
λ_0	Wavelength of the optical beam in free space	nm
E	Root Mean Square	V/m
ρ	density	kg/m^3
Q	thermal energy	J
V	volume	m^3
C	specific heat	J /K. kg
T	temperature	K

LIST OF ABBREVIATIONS

ABBREVIATION	DESCRIPTION
2D	Two Dimensions
3D	Three Dimensions
THz	Tera-Hertz
nm	nano-meter
EM	Electromagnetic
EMF	Electromagnetic Field
DNA	Deoxyribonucleic Acid
PNAs	Plasmonic Nano-Antennas
LSPR	Localized Surface Plasmon Resonance
PONAs	plasmonic Optical Nano-Antennas
SERS	Surface-Enhanced Raman Spectroscopy
BNAs	Bowtie Nano-Antennas
PBNAs	Plasmonic Bowtie Nano-Antennas
CST	Computer Simulation Technology
SPR	Surface Plasmon Resonance
SPs	Surface Plasmons
PSPR	Propagating SPR
NAs	Nano-Antennas
ONAs	Optical Nano-Antennas
MNAs	Metal Nano-Antennas
AuNPs	Gold Nano-particles
FDTD	Finite-Difference Time-Domain
FEM	Finite Element Method
FIT	Finite Integration Technique
PSO	Particle Swarm Optimization
SAR	Specific Absorption Rate
CRBPNAs	Cavity Resonance Based Plasmonic Nano-Antennas
Au	Gold
SiO_2	Silicon dioxide
VO_2	vanadium dioxide
AlGaAs	Aluminium Gallium Arsenide
SHG	Second Harmonic Generation
THG	Third Harmonic Generation
SiNx	Silicon Nitride

LIST OF TABLES

LIST OF FIGURES

CHAPTER ONE

Introduction and Basic Concepts

1.1 Introduction

Extensive researches have been carried out in the approaches for eliminating cancer cells lesion including radiotherapy, thermotherapy, chemotherapy, in addition to the surgical treatment. Photo-induced thermotherapy is one of the important techniques especially the lasers due to their unique such as properties but the size of the treatment is still determined by the wavelength due to the diffraction limit. That means the confinement and controlling the light in smaller size incomparable to the molecular cancer cells is a big challenge.

Plasmonics attract significant attention of the researchers due to Plasmon's surpassing ability to match free space electromagnetic (EM) excitation into the nano-scale size and conduct the light-tissue interaction in this scale. Plasmonic nano-antennas (PNAs) is a coupling of EM waves into Localized Surface Plasmon Resonance (LSPR) which is considered as an interesting subject for theoretical and experimental study [1]. This presents a new concept of the confinement of light in subwavelength scales with huge local fields which can generate very high near field intensities because of their LSPR. The generated field is invested in various applications that are depending on near field enhancement produced by plasmonic optical nano-antennas (PONAs) such as Surface-Enhanced Raman Spectroscopy (SERS), biosensing, spectral imaging and cancer treatment [2].

The heat produced and the thermal diffusion in the plasmonic structure are not richly investigated might be due to the shortage in the experiments. Vigorous potentials are conducted into the development of new techniques for the controlled temperature at the nano-scale and the destroying cell by the temperature rise due to the converting heat is also included.

Bowtie shape PNAs (PBNAs) can transfer the light field efficiently by converting the light from external space into a subwavelength spectral region with the improvement at an optical wavelength in a tiny area between its antenna arms [3,4]. The local EM field production in a gap area is the main reason to suggest PBNAs shape if the frequency of the incident EM waves coincide the structural resonance peak so it is acting as a tunable hot spot [5,6,7].

The nano-structures of metals with around area included in any design of optimized parameters need mainly the optical properties of PNAs especially in the medical field [8,9]. Among many metals, gold is a perfect metal against high-temperature oxidation with the best plasmonic characteristics and especially suitable for biocompatible applications.

1.1.1 Aim of the work

The main goal of the thesis is to design plasmonic nano-antennas working at the optical frequency for tumor cells treatment. This work could be accomplished through the following procedure:

1- Design a certain structure to be applied for the killing of tumor cells at both resonance wavelengths.

2- The performance of the proposed design's structure will be examined through the sweeping steps.

3- The optimization of all design structures will be carried out.

4- Design a virtual tumor in a skin tissue then will be subjected to various designs of plasmonic antennas.

5- The time required to destroy tumor cells in the proposed tissue could be estimated using a specific absorption rate.

1.1.2 Layout of the thesis

This thesis is divided into four chapters.

Chapter one introduces the basic concepts of the topics related to the main aspects of the research work. They include the concept of plasmonics involving the principle of structure, the optical characteristics, the generation of the distinguished local electric field, its importance in subwavelength applications, and the effective role in the medical treatment. In addition, the optical nano-antenna is regarded too. The features, the dimensions, and the shape are described in brief. The specifications of the skin tissue are illustrated followed by the effect of the nano-antenna on the proposed tissue. The literature survey of the updating published works is listed sequentially.

Chapter two shows the design of single and an array of nano-antenna at two resonance wavelengths (532 and 1064) nm using a numerical method via CST studio version (2017, 2018, and 2019). All designs are optimized through the sweeping and optimization processes. Tumor tissue is proposed and the design structure in certain skin tissue is also presented. The temperature elevated in the tissue after exposure to the optical antenna is estimated through its specific absorption rate.

Chapter three presents the obtained results for all the stages of the work. The performance parameters are presented and discussed for both single and array designs of nano-antennas. The near and far-field results of all cases are given and discussed. Finally, after the subjecting of the tissues to the design structures, the calculated specific absorption rate is introduced and discussed followed by the estimation of time required for killing tumor cells in tissues.

Chapter four lists the important conclusions of the obtained results and some of the suggestions that could be done in the future are mentioned.

1.2 Plasmonics

The interaction of an intense electromagnetic field with electrons ejected freely at the interface between dielectric/metal results in a quantum electromagnetic phenomenon called surface plasmon resonance (SPR). plasmonic is a field that deals with SPR. The energy transported by photons, under certain conditions, is turned into a collection of excited electrons at the interface namely surface plasmons (SPs). When the momentum of photon matched that of the plasmon, the energy transferred could occur at a specific wavelength [10]. The applications of plasmonics extend from UV to far IR reaching to THz spectral region [11,12]. The intensity of the light, the dimensions of the components, and the material used are the essential parameters that produce plasmons excited by optical frequency [13]. The suitable matters for this type of excitation are noble metals (i.e.gold (Au), silver (Ag), copper (Cu), and aluminum (Al)) so result in an important enhancement of the design and devices for twenty years ago [14,15]. The interesting potential for engineering many devices and patterns involving nano-photonic devices are based on plasmonic nano-structures [16]. Light-harvesting of the light and [17], biomedical sensors [18], metamaterials [19], tools used in advanced surgery [20], treatment of cancer tumor [21,22], heat generated via photothermal mechanism [23], the detection of DNA [24], and various applications of Surface-Enhanced Roman Spectroscopy (SERS) [24, 25].

1.2.1 Surface plasmon resonance

It is important to concentrate on the essential proportion of SPR in different forms of structures at the subwavelength scale. The SPRs excited are localized across the interface.

A sharp end in the reflectivity behavior at a certain wavelength is due to SPR, this resulted from the optical energy absorbed in the metal. SP waves are strongly bonded to the interfaces between dielectric/metal that penetrate 10 nm approximately into the metal (the skin depth) while in the dielectric, it could be more than 100 nm (corresponding to the applied wavelength). It concentrates EM waves in an are smaller than its wavelength, this feature suggests the fabrication of nano-scale photonic circuits operating at optical frequencies is possible [26].

Extended and localized are the types of SPs related to the direction of propagation. The engineering of the nano-structure became possible because of the large development of nano-science, so the LSPR becomes an interest during the last decade. The distance of microns to several microns is the propagation of the Plasmon along with the interface between metal and dielectric in the case of propagating SPR (PSPR). The degradation of SPR in the direction normal to the interface with the length of about to a half of the wavelength (200 nm in the visible spectrum) [27].

The resonance wavelength of the Plasmon could be shifted due to the interaction between the metal confined waves and the molecular layer.

1.2.2 Localized surface plasmon resonance

The light interacts with particles much smaller than the incident wavelength that leads to the oscillation of the plasmon surrounded the nano-metals with the wavelength of LSPR. They are excited in metallic structures with lateral dimensions less than half wavelength of the exciting wave. The LSPR is to change in the dielectric environment variations affect directly on LSPR. Most of the researches detected the wavelength shift of LSPR to measure the variation of the dielectric environment. Fig 1.1 [27].

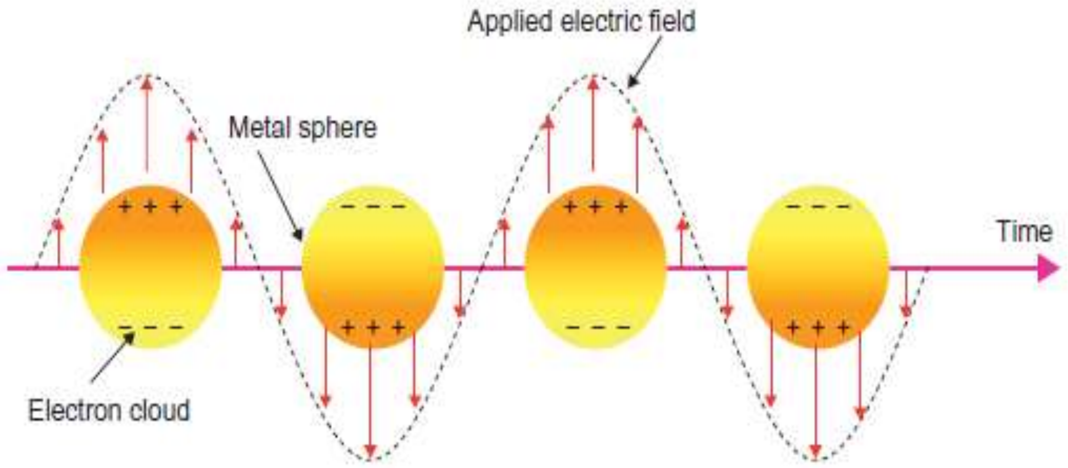

Fig. 1.1 Free electron oscillation at the surface of a nano-sphere [27].

LSPR spectroscopy can provide the sensitivity less than that of variations in the index of refraction for bulk material in PSPR. While in the short scale measurement changes in the index of refraction corresponding to the molecular layer absorption, the response of these two techniques becomes comparable. LSPR sensors offer much smaller sensing volume as the degradation length of EM, so it represents a range of (40-50) times shorter than the sensors of PSPR. The new fabrication techniques allow researchers to tune the localized resonance wavelength through the visible, near-infrared and infrared regions of the EM spectrum, by varying size, shape, and materials of nano-particle (NP) that support the LSPR [27].

1.2.3 Fundamental of plasmonics

The optical properties of SPRs in various subwavelength structures could be understood through understanding the spectral response of noble metals.

The plasma model explains the optical properties of metals in a wide range of frequencies. In this model, a free electron travels toward positive ions. The optical properties of metals are described by the responsivity of those electrons to the incident electric field.

Complex permittivity of metals as a function of frequency can be obtained using the Drude model for metals in the following equation [28]:

$$\varepsilon(\omega) = 1 - \frac{\omega_\rho^2}{\omega^2(\frac{i}{\omega_\tau}+1)} \tag{1.1}$$

Where τ is mean free time of free electron and $\omega_\rho$is the plasma frequency of the corresponding bulk metals. The valence electrons are regarded to be free in this model of metals considering free electrons are accelerated when an electric field is applied then subject collisions with the characteristic scattering time [29]. If the collision and scattering parameters are neglected and supposing a loss-less medium, then:

$$\varepsilon(\omega) = 1 - \frac{\omega_\rho^2}{\omega^2} \tag{1.2}$$

When the frequency is lower than ω_ρ, means the permittivity is negative.

A substance of a positive permittivity faces a metal with negative permittivity, at their interface related to Maxwell's equations the EM could be restricted at the interface as (see Fig1.2), [30].

$$\nabla \times \boldsymbol{E} = i\omega\boldsymbol{B}$$

$$\nabla \times \boldsymbol{H} = -i\omega\boldsymbol{D}$$

$$\nabla . \boldsymbol{E} = 0$$

$$\nabla . \boldsymbol{H} = 0 \tag{1.3}$$

The identical TM equations are:

$$\frac{\partial E_x}{\partial Z} - \frac{\partial E_z}{\partial x} = i\omega\mu_0 H_y$$

$$-\frac{\partial H_y}{\partial z} = -i\omega\varepsilon_0\varepsilon E_x$$

$$-\frac{\partial H_y}{\partial x} = -i\,\omega\varepsilon_0\varepsilon E_z \tag{1.4}$$

Where the corresponding TM wave equation is:

$$\frac{\partial^2 H_y}{\partial z^2} + (k_0^2\varepsilon - k_x^2)H_y = 0 \tag{1.5}$$

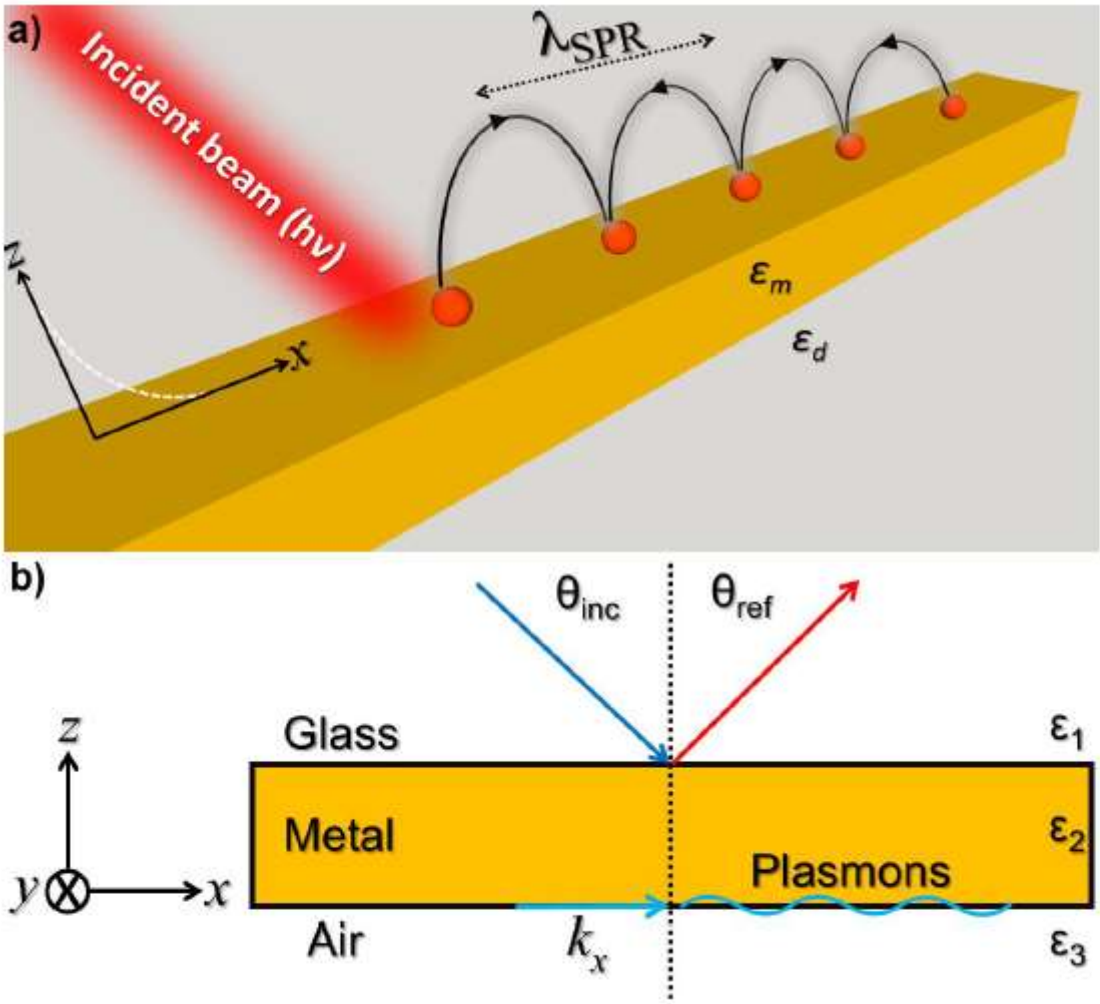

Fig. 1.2 The excitation of SPR. (a) Schematic, and (b) cross-sectional sketch for the excitation[28].

So, the metallic surface when the electric field and magnetic field components above $(z > 0)$ and inside $(z < 0)$ are:

$$\begin{cases} H_{y=} A\, exp(-k_1 z)\, exp(ik_x x), \\ E_x = \frac{Ak_1}{i\omega\varepsilon_0\varepsilon}\, exp(-k_1 z)\, exp(ik_x x)\,, \\ E_z = -\frac{Ak_x}{i\omega\varepsilon_0\varepsilon} exp(-k_1 z) exp\,(ik_x x). \end{cases} \qquad (z > 0) \qquad (1.6)$$

where ; k_1=$\sqrt{k_x^2 - k_0^2}\,\varepsilon_1$

And,

$$\begin{cases} H_y = B\, exp(-k_2 z)\, exp(ik_x x)\,, \\ E_x = \frac{Bk_2}{i\omega\varepsilon_0\, \varepsilon} exp(-k_2 z)\, exp(ik_x x)\,, \\ E_z = -\frac{Bk_x}{i\omega\varepsilon_0\varepsilon} exp(-k_2 z)\, exp(ik_x x)\,. \end{cases} \qquad (z < 0) \qquad (1.7)$$

where ; k_2=$\sqrt{k_x^2 - k_0^2\varepsilon_2}$

Regarding the boundary conditions:

$D_\perp^1 = D_\perp^2$

$$E_\parallel^1 = E_\parallel^2 \qquad (1.8)$$

Then, we have:

$A = B$

$$\frac{Ak_1}{\varepsilon_1} + \frac{Ak_2}{\varepsilon_2} = 0 \qquad (1.9)$$

By considering the expressions for $k_1$and $k_2$as above, the dispersion relation equation is given by:

$$\frac{k_x^2 c^2}{\omega_\rho^2} = \frac{\frac{\omega^2}{\omega_\rho^2}\left(\frac{\omega^2}{\omega_\rho^2}-1\right)}{2\,\frac{\omega^2}{\omega_\rho^2}-1}\,; \qquad \begin{cases} \epsilon_2 = 1 - \frac{\omega^2}{\omega_\rho^2} \\ k_x^2 = \frac{\omega^2}{c^2}\left(\frac{\varepsilon_1\varepsilon_2}{\varepsilon_{1+}\varepsilon_2}\right) \end{cases} \qquad (1.10)$$

The frequency-dependent complex permittivity could be written as mentioned in equation (1.2).

In addition, the complex wave vector $k = k_x' + ik_x''$ for the direction of the propagation, considering aforementioned equations as:

$$\begin{cases} k_x' = \frac{\omega}{c}\left[\frac{\varepsilon_1'\varepsilon_2}{\varepsilon_1'+\varepsilon_2}\right]^{1/2} \\ k_x'' = \frac{\omega}{c}\left(\frac{\varepsilon_1''}{2(\varepsilon_1')^2}\right)\left[\frac{\varepsilon_1'\varepsilon_2}{\varepsilon_1'+\varepsilon_2}\right]^{1/2} \end{cases} \tag{1.11}$$

Where the complex permittivity of the dielectric medium is $\varepsilon_1 = \varepsilon_1' + i\varepsilon_1''$

Now, the complex wave vector is:

$$k_x = k_x' + ik_x'' = \frac{\omega}{c}\left[\frac{\varepsilon_m\varepsilon_d}{\varepsilon_m+\varepsilon_d}\right]^{1/2} \tag{1.12}$$

Where ε_m and ε_d are the permittivities of metal and dielectric media. Noticing that for the Plasmon's excitation, it isn't easy to create fluctuations of the electron from the space of the beam due to the miscor rspondance of the momentum. It is observed that the dispersion relation little bit approaches the line field at (k_x) as shown in Fig (1.2), which expresses the transformation of nonradiative plasmon resonances into EM wave cannot take place. at large (k_x) and regarding $\varepsilon_1' \to -\varepsilon_2$, it can write :

$$\omega_{spr} = \sqrt{\frac{\omega_\rho}{1+\varepsilon_2}} \tag{1.13}$$

The SPR looks like a localized oscillation of electron plasma because of the phase and group velocities decrease dramatically and approach to zero [28].

1.3 Nano-Antenna

Conventionally, the confinement of optical waves is represented by the field of photonics. While the EM field controlling at different structures especially in the subwavelength scale is performed via what so-called antennas.

The links between an emitter and free-space propagation of light are called Nano-antennas (NAs). Considerable attention is observed for these structures over the past few years by reducing well-known concepts of the high-frequency electromagnetic spectral region into the nano-scale optical region. different designs including nano-rods, bowtie antenna, patch antennas or planar Yagi–Uda antennas are investigated [31].

The NAs can control the light beam in a subwavelength scale. Therefore its ability to transfer the propagating EM radiation into localized energy has gotten numerous researches in various applications such as sensing, photodetection, metasurfaces, medicine, photovoltaics, and energy harvesting applications [32].

The essential parameter for those applications is the electric field enhancement. It is influenced by the material quality and nano-structure dimensions, including the non-ideality of both. A numerical method is done to design these structures for a certain purpose, and for optimized fabrication with supposed optical properties [33].

The aim of designs in Fig. 1.3 of both antennas is similar. This shows the optimization of the energy convert between a receiver and the free- space electric field [34].

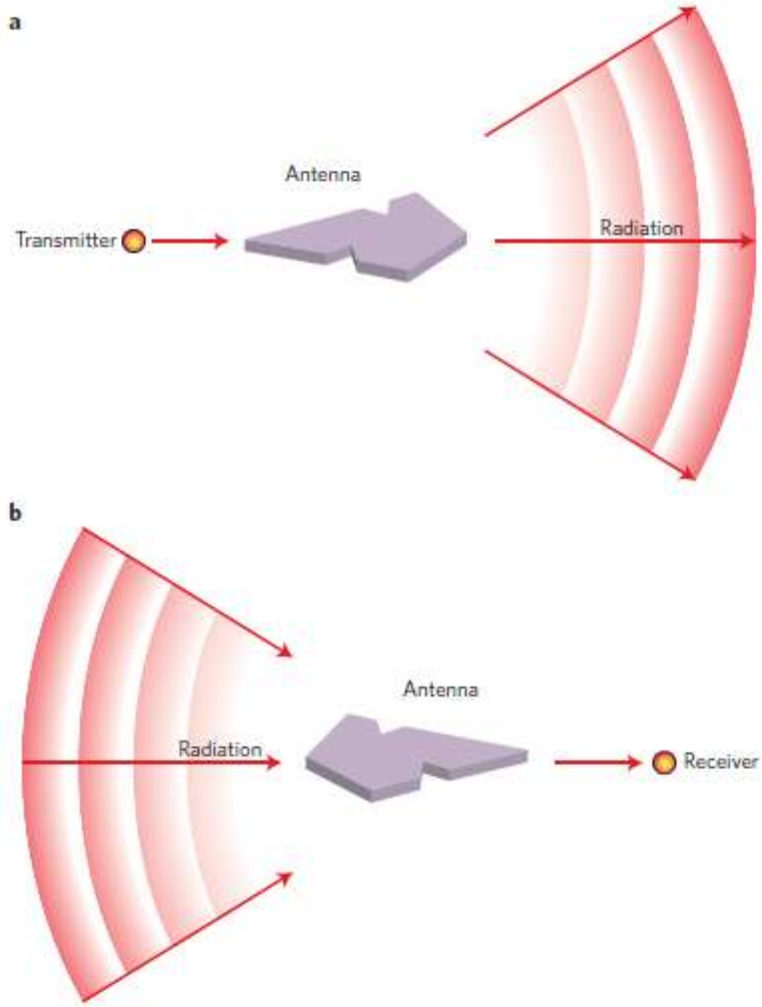

Fig.1.3 Design of an antenna for both (transmittance, receiving) at (a) and (b) respectively regarding the field direction [34].

1.4 Optical nano-antenna

The optical field could be transformed into localized energy via a structure called optical nano-antennas (ONAs). Their structures have an ability to control and manipulate the optical field at subwavelength scales. ONAs is the subject of the development of several numbers of research fields, and the efficiency of spectroscopy can improve sensing and heat transfer. Because of their small size, they became the first choice of new technologies in spite of the wide use of radio wave and microwave antennas [34].

ONAs require engineering accuracies of the characteristic dimensions down to a few nano-meters while about to the wavelength scale in other antennas. ONAs are fabricated by what so-called top-down nano-fabrication tools such as focused ion beam milling or electron-beam lithography [35, 36, 37, 38], and sometimes via bottom-up self-assembly technique [39, 40]. An important property of ONAs is overcoming the diffraction limit down to the nano-meter scale, which represents the distinguishing characteristics for novel photonic applications. However, this downscaling holds the technological challenges of nano-scale antenna engineering. The antenna performance can be strongly enhanced by plasmon resonances that lead to high and confined fields [34].

The optical excitation of ONAs with a suitable wavelength can produce very high near-field because of their LSPR. The miscorresponding between the diffraction-limited the exciting wavelength and molecules fluorescence are enhanced due to existing of metallic nano-meter size in ONAs. In addition, the excitation and emission rates of molecules could be increased via ONAs [37].

Passive ONAs are observed in the first time in the microwave region by Grober and coworkers. Also, mid-IR passive antennas and bowtie antenna are built. Near-field improvement created by ONAs is important for SERS. Metallic nano-structures are useful in biosensing, near-field probes, solar applications, and cancer treatment [41].

1.5 Plasmonics nano-antenna

Plasmonic nano-antennas (PNAs), are able to controlling and confining EM field at the nano-scale. The performance evaluation of PNAs is depending on two important parameters, the absorption of the light and field improvement locally. A wide research areas invest the high light absorption, such as thermal emitters, solar thermal applications, thermal photoluminescences, and sensors. The improved electric fields at resonance wavelength can modulate the optical properties in the vicinity of molecules, so that, enhancing their light-matter interactions [42].

The tuning of the plasmon resonance for both absorption and emission to the excitation or the emission of species is the interesting research recently. The exciting EM field is enhanced several order of magnitude due to the production of what so-called hot spots when perfect nano-structures are designed. The structures working at plasmonic resonances open the ability to implement antennas working in the visible. The hot areas could be used to excite the effects at nonlinear regime so to match the EM field effectively. SERS and tip-enhanced Raman spectroscopy are the practical techniques that show the influence of such hot areas to observe the emitters with its sensitivity down to a single molecule [43].

The construction structure of PNAs is depending mainly on putting a gap at the sub-wavelength scale between two metallic areas, are gained distinguishable importance. This is mainly because of the hot spots in PNAs produce intensive EM field in nano-size overcoming the restriction of the diffraction. The confinement of the light field by BNAs is observed to be several order of magnitudes in the nano-scale smaller than the incident wavelength, as improved by the dimensions of the gap [44].

The resonance wavelength decisively depends on the shape, dimensions, and material of the antenna, a numerous variation of plasmonic antenna structures published proposed, such as bowties, nano-rings, nano-rod, and Yagi-Uda antennae. The sharp resonance wavelengths with narrow-band spectra with sharp are a major challenge for applications that require devices operating over a wide range of frequencies. For example, antennas used to improve energy harvesting efficiency of photovoltaic devices. Broadband PNAs are also highly wanted for SERs, fluorescence enhancement, and higher harmonic generation, which are multi-wavelength and broadband in nature [45].

1.5.1 Metal nano-antennas

Distinguished spectroscopic features (spatial, spectral) are observed in noble metal nano-antennas (MNAs) such as Au NPs and Ag NPs. MNAs have those features resulting from the oscillations of electrons collectively in the conduction band, which is LSPR [42].

MNAs can confine and improve near IR and visible field in superficially by the excitation of LSPR. The 'EM hot region (spot)' that could be created on the nano-antennas has excessively utilized the absorption of light locally leading to an increase the weak intensity in the nonlinear optical process [46].

Au nano-particles (Au NPs) could effectively absorb IR and visible field energy in quite concentrated sizes, getting them properly controllable heat source in subwavelength size. In addition to the great importance the mechanism of those phenomena to be investigated, the capability to generate point like heat nano-heat encourage a broad area of research in physics, chemistry, and biology. The aforementioned properties of Au NPs especially as a nano-sources are promising researchers in the catalysis at nano-size, photonics, and in the field of medicine for cancer cells destroying photothermally [47].

1.6 Heat generation in nano-antenna

PNAs cause an exaggerated heat produced in the metal after the excitation of the external light source, producing a side hot areas – i.e., the elevation of the temperature in a restricted region which is a mainly undesirable effect in various research namely spectroscopy, sensing, and optical signal processing. Localized heat of PNAs, in another hand, is very useful in a group of applications such as nano-engineering, cancer treatment, nano-manipulation, hot vapor generation, and catalysis [46].

The local temperature elevation of MNAs is quite low thermal radiation in the mid-to-far IR wavelength spectral region. In addition, if (the mean free path) of the substrate materials is larger than the nano-antenna size, the heat converted the volume of metal volume may be reduced [48]. It is well known that the metals in nano-size create regional temperature gradients after external light exposure, quite enough to generate subwavelength areas of super-heated water surrounding the species [49].

Photo-induced heating of nano-antennas can vary their geometry because of the metal melting. The melting process can minimize the nano-range properties so, directly nano-antennas becomes nano-spheres if temperature increment is established. The variation of the morphology may affect on the antennas' spectral response and can decrease the near-field generation. The melting temperature of metal can take place at higher surface melting temperatures of nano-antennas [50, 51].

The pioneering author is previously shown that the structures of hybrid plasmonic have good selectivity and huge improvement of the near-field intensity due to effective trapping with re-cycling of photons in near IR and visible in photonic modes [52, 53, 54].

The IR thermal radiation could be produced and enhanced by the selection of the optimum parameters of materials and the dimensions regarding the geometry on a range at or under the emitted thermal peak resonance wavelength [46]. The convective and radiative cooling represent other ways to diffuse heat intensity from nano-sizes, where became effective if the thermal conductivity is disturbed because of the particles in the nano-size [55].

1.7 Numerical methods

This section presents in brief, a well-known and promising numerical methods which support to understand the type of problem-related to sub-wavelength systems. The design of different shapes and dimensions working in various resonance frequencies especially the optical needs recommended procedures. The Finite-Difference Time-Domain (FDTD) algorithm is convenient for the modeling of structures including plasmon resonances with nano-photonic characteristics due to supporting distinguished feasibility and matrix free nature [56, 57]. The Finite Element Method (FEM) is a popular tool to execute the numerical analysis in the domain of photonics, it provides a precise calculation of EM field in Maxwell's equations [56, 58]. Finite Integration Technique (FIT) is the encouraged technique which is utilized for investigating the different aspects of the proposed structures. It is worth mentioned that the numerical methods are depending on the differential form to solve Maxwell's equations [59].

1.7.1 Finite integration technique

The Finite integration technique is developed by Weiland in 1977 which introduce a separate rewrite of Maxwell's equations in the integral form convenient for computers [59]. The real-word EM field problems with sophisticated geometries. The finite volume-type discretization scheme for Maxwell's equations depends on the utilization of integral forms. So, the stability and conservation features of the separate fields also before numerical calculations are begun. Such features get the improvement of high stability numerical time integration schemes or precise. The last researches showed that, the language of differential forms and concepts of algebraic topology are used to investigate Maxwell's equations. They paraphrase close to those separate formulations of the FIT, regarding, it is found for more than twenty years [60].

Algebraic analogs to Maxwell's equations could be exactly generated by FIT, where the physical characteristics of fields that are confined in the separate space could be conserved, and giving a single solution. Using assigned voltages on the edges and fluxes in front of a grid ("primary grid") and magnetic voltages on the edges and magnetic fluxes in front of a second grid ("dual grid") enable Maxwell's equations and related equations of materials could be converted from continuous to the separate space. It is worth to mention that the use of voltages and fluxes (integral degree of freedom), instead of field components (such as used in FDTD), presents not only a quite convenient method of writing the matrix form of Maxwell's equations but great significance algorithmic-theoretical and numerical results [61].

1.8 Sweeping technique

The Parameter sweep technique introduces an easy and effective way to accomplish several simulations with various structure parameter values. For each simulation, previously specified results will be stored. After the simulations have finished, these results could be plotted in relation to their parameters.

By applying a sweeping technique using a certain algorithm to sweep the geometric parameters over the supposed range the following steps are done:-

(i) Set the initial values of the parameters unit over a range

(ii) Appling sweeping tool simulated.

(iii) Record the properties of the performance.

(iv) Select the values of geometric parameters that yield suitable at the required wavelength.

(v) Study the performance of geometric parameters.

1.9 Particle swarm optimization technique

Particle Swarm Optimization (PSO) is a population-based stochastic optimization algorithm which is usually used in the specific problems, application experience and numerous experiment tests [62].

PSO belongs to a range of evolutionary techniques developed solver global optimization. The PSO algorithm has the appeal of simplicity and evidence of good performance in a variety of application domains. It is more computationally effective than the genetic algorithm [63]. A swarm is a disorganized population of traveling singles that face to cluster together while every single seem to traveling in an unlimited direction. Every particle in the swarm has the ability of interaction with the other particles, in spite of abilities of every particle are restricted by a group of rules.

The operation principle of the basic PSO technique can be described as follows [64]. Consider files consist of individuals of during an N-dimensional space to be searched, knowing that an effective solution of the optimization is represented by the location of every individual. Each particle a in the swarm,

$\xi = \{x_1, .., x_a, .., x_s\}$, is represented be following characteristics

$x_{a,j}(t)$: jth-dimensional component of the position of particle a, at time t.

$v_{a,j}(t)$: jth-dimensional component of the velocity of particle a, at time t.

$y_{a,j}(t)$: jth-dimensional component of the personal best (p best) position of particle a, at time t.

$\hat{y}_{a,j}(t)$: jth-dimensional component of the global best position of the swarm, at time t.

Let F denotes the fitness function to be optimized. Then the personal best of particle a can be updated in iteration $t+1$ as,

$$y_{a,j}(t+1) = \begin{Bmatrix} y_{a,j}(t) \ \text{ if } F(x_a(t+1)) > F(y_a(t)) \\ x_{a,j}(t+1) \ \ else \end{Bmatrix} \forall j \in [1, N] \quad (1.14)$$

Since g best is the index of the global best (GB) particle, then $\hat{y}(t) = y_{gbest}(t) = \min(y_1(t), \ldots, y_s(t))$. Then for every repetition in a PSO, updating the positions are accomplished for every particle, $a \in [1, S]$ and along with every dimensional component, $j \in [1, N]$, as follows

$$v_{a,j}(t+1) = w(t)v_{a,j}(t) + c_1 r_{1,j}(t)(y_{a,j}(t) - x_{a,j}(t)) + c_2 r_{2,j}(t)(\hat{y}_{a,j}(t) - x_{a,j}(t)) \quad (1.15)$$

$$x_{a,j}(t+1) = x_{a,j}(t) + v_{a,j}(t+1) \quad (1.16)$$

where w is the iteration weight, and c_1, c_2 are the acceleration constants. $r_{1,j}$ and $r_{2,j}$ are random variable lie between 0 and 1 with a uniform distribution. The memory part is represented in the first term of the summation is , which regards the participation of prior velocity, while the cognitive component is written in the second term, where considers the experience of particle alone and last the social component is represented in the third term during which the particle is ‘guided’ by the g best particle against the GB solution so far founded.

PSO could be summarized as a population-based optimization technique where the swarm is a collection of particles. Each particle has both positions (represents a candidate solution to the problem space) and velocity (which is used to move the particle from one position to another) [65]. The basic algorithm of PSO can be listed as follows:-

(i) Initialize the swarm from the solution space.
(ii) Evaluate the fitness of each particle.
(iii) Update individual and global bests.
(iv) Update velocity and position of each particle.
(v) Go to step (ii), and repeat until termination condition.

PSO technique is applied to the designed of nano-antenna to enhance the characteristics and performance.

1.10 Types of skin cancer

The abnormal cells are cancer, where the block is built by the body's basic. The human body normally creates new cells to support us grow, compensate exhausted tissues. The cells usually die in an organized way.

In addition, the growth of cell could not occurred, where they are splited and died in an ordinary way. This regards the main reason to find lymph fluid or blood which is abnormal, or due to a lymph nominated a tumor.

A tumor could be either malignant or benign.

- **Benign tumor –** It is not regarded as cancer. A group of cells concentrate in a certain region and have not the ability to diffuse to another part of the human body.
- **Malignant tumor –** This tumor makes up of cancerous cells, where the ability of diffusion is the main feature of those cells by traveling through the lymph fluid or blood stream [66]. See Fig 1.4.

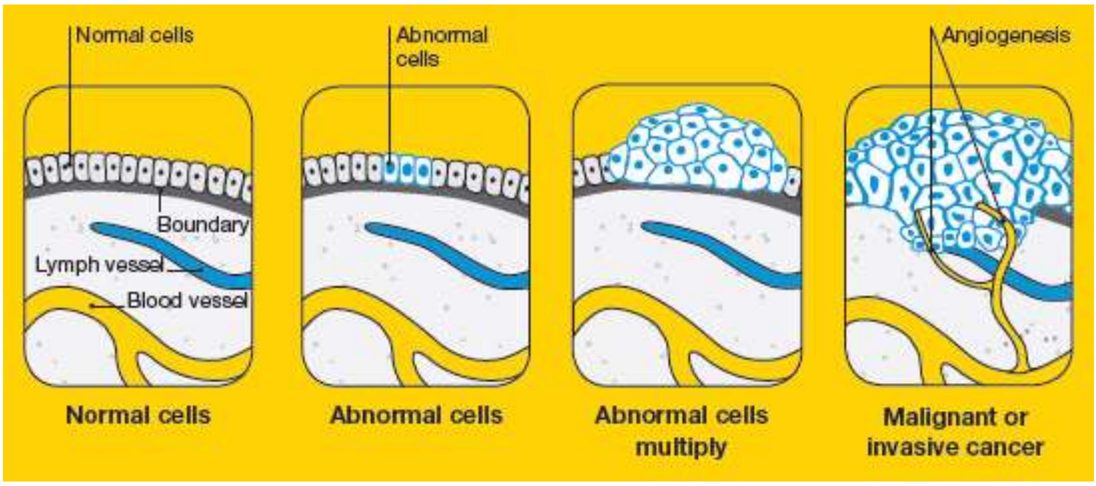

Fig. 1.4 The starting steps of cancer [66].

The primary cancer is considered that grows in an organ for the first time. When any tissue or organ influenced, it is called a malignant tumor.

It is important to mention that there is another type of tumor called a localized tumor which is not diffused to other parts.

The secondary cancer is the formation of another tumor during the growth of the cancerous cells. One of the popular cases is skin cancer. The metastatic skin cancer is a type that spreads to lymph nodes. Knowing that the squamous cell carcinoma has the ability to diffuse, while there is a type called basal cell carcinoma which rarely diffuses [66]. See Fig 1.5.

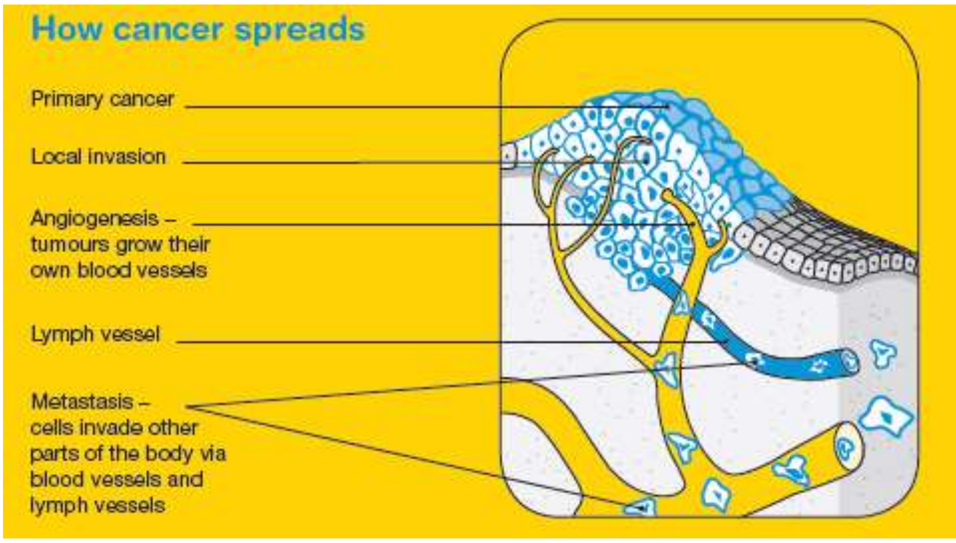

Fig. 1.5 The stages of cancer spread [66].

Skin cancer is the most commonly diagnosed cancer, and rates have been rising for the past 30 years.

There are three main types of skin cancer [66, 67]:

1- Melanoma – begins in the melanocytes and is the deadliest form of skin cancer.

2- Squamous cell cancers – starts in the squamous cells of the skin and typically appear on sun-exposed areas.

3- Basal cell cancers – begins in the basal cell layer of the skin and its growth seems slowly.

1.11 Treatment of tumors

The elevation temperature above its ordinary state in any part of the human body due to an external effect for a limited time is regarded a thermal treatment. An important role was observed for the temperature in the thermodynamic of both cells and the complex one (organs, tissue) [68]. One of the more essential indications for the existence of a certain disease is the temperature elevation above the ordinary human body temperature (37° C) which definitely causes fever and even the organs could be damaged irreversibly [69]. In the similar time, if the elevation temperature is controlled and confined, positive influences on the patient could be observed, such as destroying cancer cells. Interested and enormous potentials are performed, in last years, to develop new techniques for confinement and locally controlling the heat diffusion. In addition, important efforts are done to understand and analyze the mechanisms that depend on the principle of photo-thermal induced cell damage and destroying [70]. It is concluded that this concept of temperature-induced cause changes at the cellular level which is affected by two factors the light intensity and the duration. Owing to the value of the temperature increment, thermal therapy and related influences on tumors could be divided into several durations [71], as illustrated in Fig. 1.6.

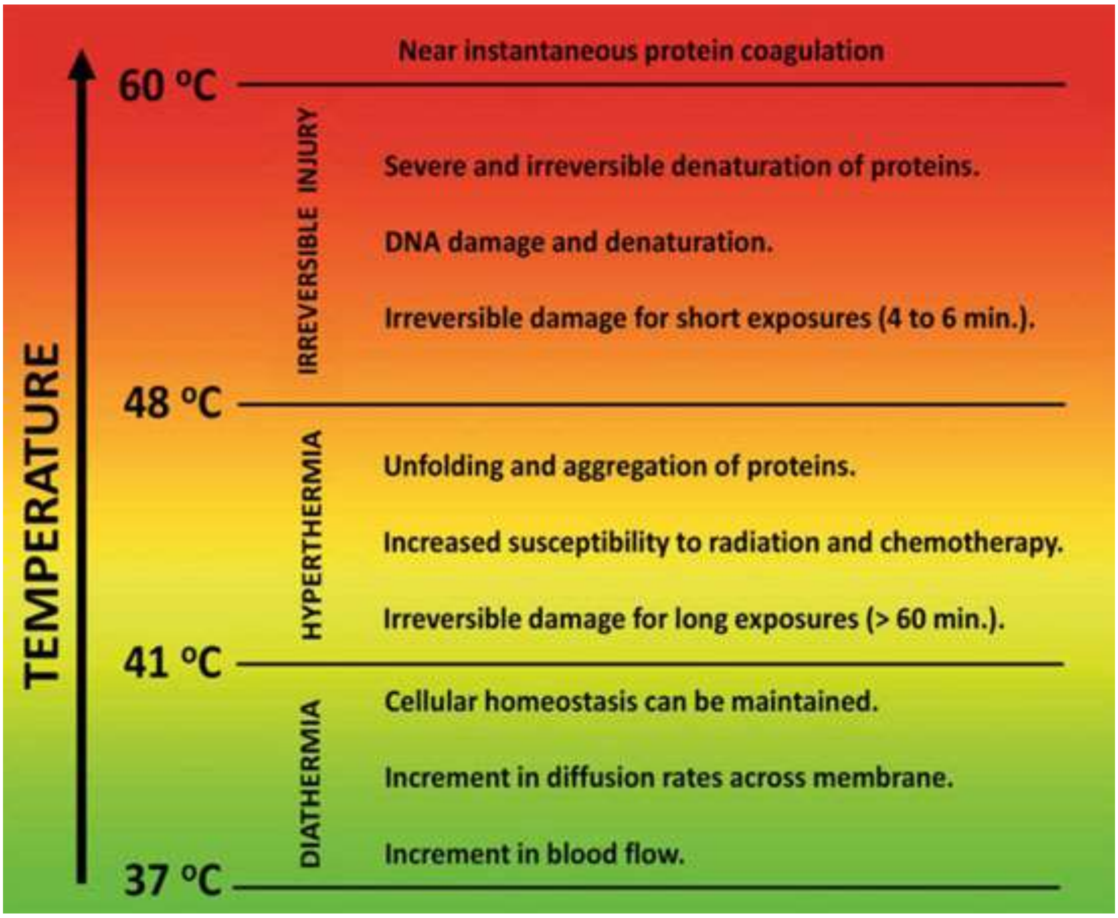

Fig. 1.6 Schematic diagram of various effects caused by the different thermal treatment as classified by the corresponding operating temperature [72].

Irreversible damage therapy could take place if the temperature of the tumor increased above (48° C) through a limited time. So that, a severe activity of cell death is performed. Now, if the temperature rises above (60° C), an irreversible protein denaturation will be occurred. Although those therapies are regarded quite effective but the main drawback that is noticed in the adjacent tissues is the collateral injury. Knowing that hyperthermia therapy of the tumor would occur Within (41-48° C). A pertinent influences at the cellular level are induced if the temperature becomes up to (41° C), which is useful in the pain relief therapy and in physiotherapy that needs relax of the muscle [73].

1.11.1 Treatment by nano-particle

Great attention has attracted due to the unique properties of NPs which have the ability to generate an effective heat via the laser exposure. Interesting results are obtained in the treatment of cancer phoyothermally, investing the plasmonic properties of Au nano-structure in near-IR region through the mechanism of non- radiative effect. Different types of gold nano-structures are studied using opto-thermal therapy. The main parameters that should be considered when selecting a nano-structure for photothermal therapy for cancer cells are the size of NPs, absorption cross-section, and resonance wavelengths [74].

Tunable plasmonic nano-materials are interesting due to large optical absorption coefficients and possibility as NAs that face tumors and transfer EM energy into thermal state locally for the ablation process. Practically, various methods were performed to conduct the ablation of the tumor, radio wave, lasers, and the focusing of ultrasound. The main problem that faces all those procedures is the capability to select the tumor cells from the surrounding environment. Potential researches are concentrated to look for an external source that could select tumors through its geometry, but they are still a challenge [75].

NAs is another and recommended choice for because they represent a specific heat external source has an ability to select tumor tissue leaving the healthy ones unaffected, knowing that this technique still needs more researches yo be practical. It is useful to mention that the external pulse light source may present a theoretical case to perform tumor-targeted nano-antennas for select single cell accurately. It could be deduced that this procedure opens up a precision operation rather than that of conventional technique which means that the complex tumor in sensitive tissues may be the next goal [76].

1.12 Effects of tissue on nano-antenna

The passing of the electromagnetic field through the human body is depending on the thickness and the real structure of biological tissues. The human body is a multilayer medium. Each layer has its own dielectric characteristics. These properties are important to conduct an interaction between NAs and tissues. The characterization of the tissue response to electromagnetic waves, the permittivity ε_r and the conductivity σ should be well-known. It is worth to mention that the absorption of the skin is depending on the depth of those layers from the surface (i.e. not all layers absorb similar wavelength), as illustrated in Fig 1.7. Essential characteristics of the dielectric properties are significant variations in permittivity and conductivity of around some frequencies because of dielectric relaxation phenomena, high permittivity values at lower frequencies and large variations in optical properties between the tissues [77].

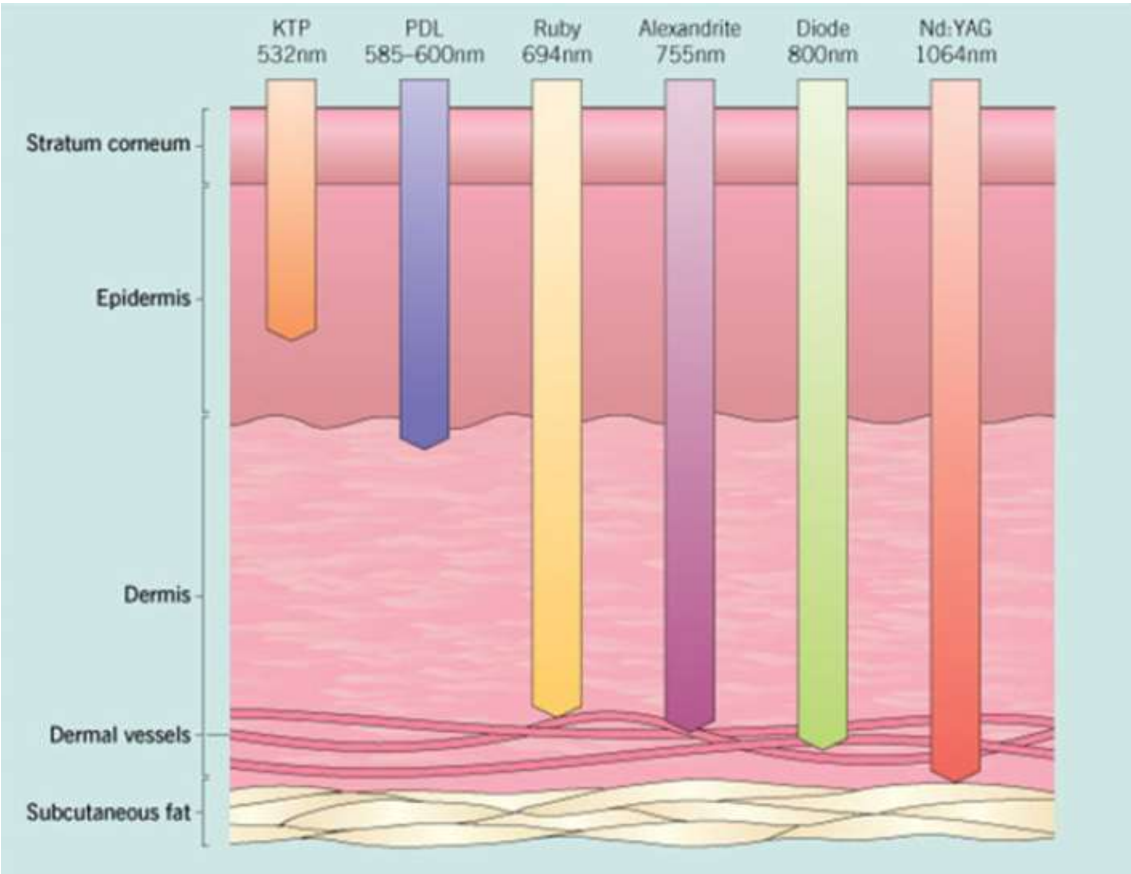

Fig 1.7 Absorption spectrum of the skin [78].

Mathematical modeling of the interaction of electromagnetic fields with various tissues requires the information of the properties of the radiation source. In addition, the geometry of the body exposed as well as its electrical properties should be taken into account like conductivity, permittivity, and permeability which is equal to that of vacuum for biological tissues. The electrical permittivity and electrical conductivity are specific to each tissue and depend on many factors such as the frequency and the temperature. The behavior of the electromagnetic field created by an excitation source and propagating towards a biological medium can be described by the Maxwell equations using simple geometric configurations. The wave vector is equal to:-[79].

$$k = \frac{\omega}{c}\, n + j\kappa \; = \beta + j\alpha \qquad (1.17)$$

Where: n and κ represent the real part and the imaginary part of the complex index N of a medium, such as:

$$\text{N}= \text{n}+\text{j}\kappa = \sqrt{\varepsilon_r (1 - \frac{j\alpha}{\omega\varepsilon})} \qquad (1.18)$$

Where n is the index of refraction characterizing the propagation of the wave and κ represents the extinction index that characterizes the damping of the wave in the direction of propagation due to energy losses in the medium. While: $\alpha = \kappa \frac{\omega}{c}$ is the linear attenuation and $\beta = n \frac{\omega}{c}$ is the linear phase shift (rad/m).

Phase and group velocities are depending on β while the signal attenuation in the medium considered depends on α. The values of α and β are calculated from the complex expression of the wave vector and become:

$$\alpha = \; \omega \sqrt{\frac{\varepsilon\mu_0}{2} [\sqrt{1 + \frac{\sigma^2}{\varepsilon^2 \omega^2}} - 1]} \qquad (1.19)$$

$$\beta = \omega\sqrt{\frac{\varepsilon\mu_0}{2}[\sqrt{1+\frac{\sigma^2}{\varepsilon^2\omega^2}}+1]} \quad (1.20)$$

So, the wavelength of signal in the medium is given by:

$$\lambda = \frac{2\pi}{\beta} = \frac{\lambda_0}{\sqrt{\frac{\varepsilon_r}{2}[\sqrt{1+\frac{\sigma^2}{\varepsilon^2\omega^2}}+1}} \quad (1.21)$$

With: $\lambda_0 = \frac{c}{f}$

The penetration depth of electromagnetic fields in the tissues is limited because of the skin effect and the diffusion of energy in the media. The skin effect produces a reduction of the field $E\ (z)$ at a distance z from the interface according to the relation: $E\ (z) = E_0 e^{-\alpha z}$ with E_0 is the amplitude of the field at the interface level.

The penetration depth (or skin depth) corresponds to the distance at the end of which the amplitude of the wave is decreased to $1/e$ of its initial value, whether:

$$\delta = \frac{1}{\alpha} = \frac{1}{\omega\sqrt{\frac{\varepsilon\mu_0}{2}[\sqrt{1+\frac{\sigma^2}{\varepsilon^2\omega^2}}-1]}} \quad (1.22)$$

The incident light passing through the skin is presented in Figure 1.8. The light passes the epidermis where the melanin pigment either absorb or scatter the incident light. The direction propagation of the light is varied whenever a variation in the refractive index takes place in its traveling path. The direction of light through the skin is changed slightly because there is a difference in the refractive indices of organelles and cell membrane resulting in the scattering by the layers of the epidermis. It is targeted toward the dermis. A fraction of incident light is absorbed by melanin, corresponding to the size of tissues occupied by melanosomes. The light could be scattered when entering the dermis tissue because of Rayleigh scattering in a small region of collagen fibrils, the light may be back scattered toward epidermis again, so the scattering occurs towards the skin surface and out of it. The light is scattered after penetrating reticular dermis in a wide area of collagen fibers (Mie scattering) directed toward the deep layers. A fraction of incident light is absorbed by hemoglobin in the dermis, related to its volume of the tissues. Regarding Mie scattering, the penetrated light in the reticular dermis is reaching subcutis and is emitted again backward and crosses two parts of fibers (hemoglobin, melanin) then it is again reflected and suffer from scattering by the air in the interface region. The detected light passes two times through the filters of melanin and hemoglobin [80].

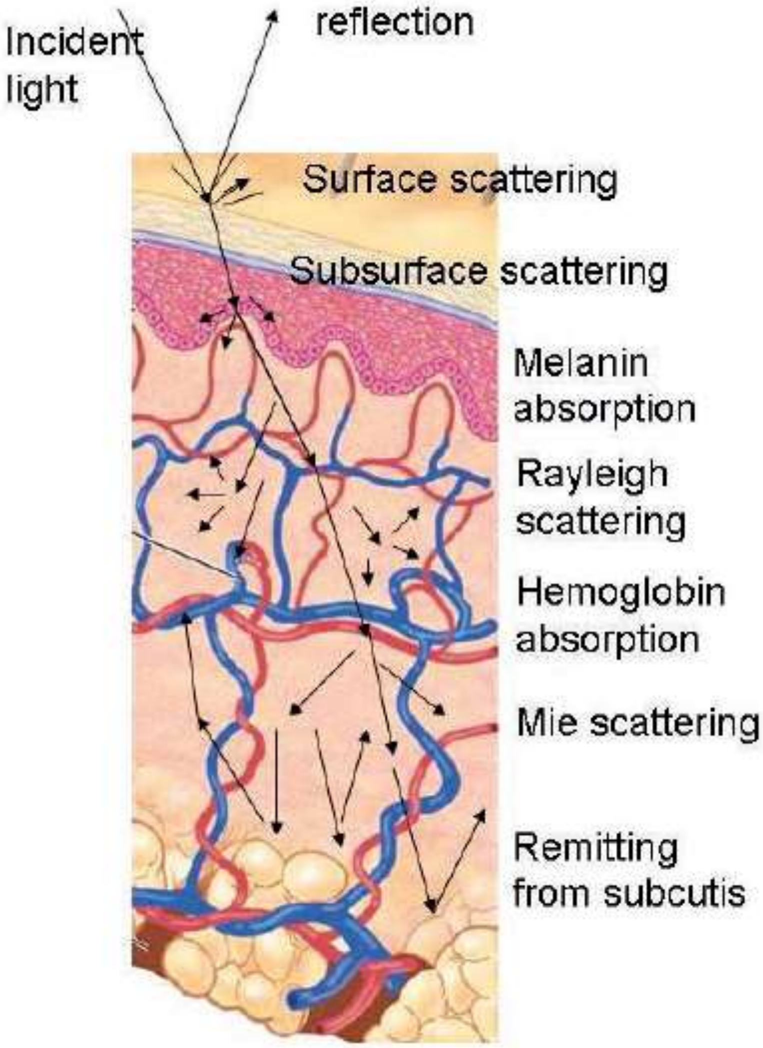

Fig. 1.8 The optical track of visible light through the skin [80].

When the human tissues are irradiated by the electromagnetic fields, the energy generated by the EM wave is mainly absorbed by the biological tissues. The expected reaction of the biological tissue that exposed to the EM field is of quite an importance in the design or develop a certain system. The extension result of the EM field is the elevation temperature of the tissue in a limited region caused by the generated heat which could affect on the biological system. The heat diffusion and its influence on the tissue are specified by the Specific Absorption Rate (SAR). SAR magnitude can not increase above the level of irradiation which becomes harmful. SAR magnitude is depending mainly on various factors such as the position of the antenna related the human tissue, the intensity field of the antenna, and the power [81].

Tissues optical properties namely; Permittivity, Permeability (which is equal to 1 because the tissue is non-magnetic), Electrical Conductivity, Absorption, Scattering, Anisotropy, and real refractive index should be taken into account. The thermal properties that are used in the mathematical model might be selected from the database related to the selected tissue. Some of these thermal properties are density, heat capacity at constant pressure, thermal conductivity, and the heat source [82].

1.13 Specific absorption rate

The specific absorption rate (SAR) is an indication tool of absorption where the EM field exposure in the human body could estimated. SAR is mainly used to measure the absorbed power in the tissues after irradiation by external field so that it gets the heat of tissue to be increased. The biological tissue heat could be checked via a safe method which is mainly depending on measuring the temperature elevation in tissues. It is mentioned that the temperature and SAR are evaluated in the human tissues so the precaution measures are verified. SAR is a function of many factors. Those factors affect on the absorption of EM field. SAR variations are depending on the properties of the wave, properties of the body and environment properties. Regarding the properties of the wave, the extent of SAR changes is depending directly on the features of the signal, such as frequency and polarization. In another side the dependence with the tissue human body, the SAR value depends on the type of tissue (e.g., geometry, size, age, and dielectric properties) and tissue orientation/exact location (e.g., the situation of the body; front or back incidence). SAR, in addition, depends on the exposure states, e.g., environmental exposure (indoor and outdoor) and influences of other objects in the field near the exposed body [83].

It is important to understand SAR calculation with respect to averaging design. There are two procedures to accomplish SAR calculations: first is point SAR, and second is averaging SAR (i.e mass or volume). Point SAR is the value regardless of the averaging of the mass and the maximum SAR of all the grid cells is provided. When the absorbed power in each grid divided by grid mass, the point SAR is evaluated. While in the averaged SAR, a cube of known mass, e.g., 1 g or 10 g, is utilized for every point, then the loss of the power density is integrated on this region. Then, the power loss in the integral form is divided by the mass cube [83, 84].

The absorption of EM field that is transferred to heat in the human body depending on the incident EM power density is measured via SAR. It is written as Eq. (1.23) [84].

$$SAR = \sigma |E|^2 / 2\rho \quad \text{(Kg/w)} \tag{1.23}$$

Where:-

σ = conductivity of the tissue-simulating material (S/m)

E = total Root Mean Square (RMS) field strength (V/m)

ρ = mass density of tissue-simulating material (kg/m^3)

Because the electric field is usually not spatially uniform, SAR is averaged over a volume of tissue regarding the type of the source. It is useful to mention that the electric field is not fixed in time, so that, the probe is used for short-term time-averaging [84].

1.14 Time period estimation

The temperature is elevated in human tissues due to the absorption of power from EM fields. An irreversible damage of the tissue can take place due to the absorption of high power. The dielectric and thermal features of the proposed tissue model are used to evaluate the relationship between the temperature and the point SAR, it could be estimated considering the equation of heat (1.24) [85].

$$dQ = \rho\, V\, C\, dT \tag{1.24}$$

Where:-

Q = the thermal energy (J)

V = the volume (m^3)

C = the specific heat (J /K. kg)

T = the temperature in Kelvin (K)

Both sides in (1.24) could be divided by ($\rho\ V\ dt$), then the terms are rearranged, so the following equation could be written as:

$$(dQ/dt)/\ \rho\, V = C.\ dT/dt \tag{1.25}$$

The SAR value is represented in the left side, so that the thermal distribution in tissues for a period of (Δt) can be determined.

It can rewrite Eq. (1.25) [85] as:

$$\Delta T = (SAR \times \Delta t)/\ C \tag{1.26}$$

1.15 Literature survey

In 2008, H. Fischer and O. J. F. Martin [86] designed two types of plasmonic NAs (dipole and bowtie) using a numerical method. The optical properties are regarded, in addition to the design parameters namely bowtie angles, length, gap, substrate thickness, and background indices are studied. The results revealed that the calculated bowtie structures have a sharper tip (20 nm) than the calculated dipole structures (40 nm). Despite the stronger field enhancement of the dipole antenna, the bowtie structures showed stronger sensitivity to environmental index changes.

In 2009, D. D. Gupta et al. [87] proposed a mathematical model for laser-induced NAs was developed to destroy the tumor cells regarding the rise temperature estimation in comparison to in vivo experiments. The principal properties of photo-energy transport in addition to heat diffusion for plasmonic NAs through live tissues were considered. A simulation program was built to analyze the practical results to be reproduced precisely. A clear understanding of the thermodynamic phenomenon is expected. The model provided a primary step against the expression of the multistage processes of the mechanism that depends on photothermal ablation. The model of “nano-surgeries” becomes possible where the using a pulsed laser source and NAs have the ability to create thermal gradients in nano-scale volume spectacularly that could provide the specification of single-cell treatment.

In 2010, S. V. Boriskina and L. D. Negro [88] investigated grating-assisted nano-antennas that give multiwavelength focusing in a single subwavelength spot. The concentration of the light in spot area in the range of subwavelength is the main purpose of this type of NAs, which are structured via implementing conventional bowtie NAs into repetitive gratings. A new implementation was added which is the combination between LSPRs of a couple of antennas and the gratings of periodic mode, involving the operation several wavelengths with the field enhancement.

In 2011, J. Chen et al. [89] demonstrated directly the experimental findings that various shapes and sizes of pure ferromagnetic nickel NAs proved the existence of dipolar plasmonic mode, which opened up important trends for new possibilities. The calculations via numerical method revealed that the comparison between the images of near field wavelength and the spectrum of the far-field indicated a significant difference between far and near fields spectra nickel NAs.The results revealed that a clear red shift was observed in the resonance of near field in comparison to that of far-field, this influence does not appear before so it indicates obviously the role of nobel metal antenna.

In 2012, M. Mivelle et al. [90] successful engineering of nano-aperture BNAs at the end of tapered optical fiber was performed practically. Using a single molecule as an optical nano-sensor connected to antennas, the three-dimensional near field regenerating from those nano-structures was measured. The results demonstrated that the field could be confined to the dimensions scale smaller than 80 nm in the area of the gap by BNAs while the total enhancement in throughput rather than the old subwavelength is about to $\sim 10^3\times$ that could be allowed by the whole probe. This is because of the precise location of the BNAs near the cutoff fiber cutoff area guiding to an increment of the value of the electric field matching the BNAs, in another side, the field generated by the tapering area of popular probes suffers from great reduction.

In 2013, J. M. Jornet et al. [91] a new design of graphene-based plasmonic NAs is presented and investigated that could be used in the communication. The supposed NAs is composed of a nano-ribbon from thin graphene and reconstruction a strip of NAs. It is regarded as a plasmonic resonant cavity and founded its wavelength response. The conductivity of graphene nano-ribbon of semi finite size as a function of its width was analyzed and computed for the first time. The results showed the graphen based NAs could work at quite low frequency rather than the same volume of the conventional antenna if the compression of a high wave of SPP waves is invested.

In 2013, Z. J. Coppens et al. [92] described new methods for designing and thermally probing thermo-plasmonic structures. A general design rationale, based on Babinet's principle, is developed for understanding how the complementary version of ideal electromagnetic antennae can yield efficient nano-scale heat sources with maximized current density. Using this methodology, they demonstrated that highly localized and enhanced thermal hot spots can be realized by incorporating the diabolo antenna into a plasmonic lens using FDTD numerical method.

In 2014, J. Calderón et al. [93] described on the first polarimetric plasmonic biosensor based on arrays of bowtie nano-antennas. Using the Finite Element Method (FEM) to study the phase retardation between the axis of the nano-antennas. After optimized them for high volumetric sensitivity at a wavelength of 780 nm, sensitivities ~5 rad/RIU are obtained.

In 2015, Q. Wang et al [94] studied a temperature-responsive BNAs device by coating the plasmonic dimers with a submicron-thick thermoresponsive hydrogel. The index of refraction variations could be detected from shift in the resonance spectrum due to high field improvement of the modes in the BNAs. The obtained findings proved that a resonance shift at 16.2 nm was noticed when hydrogels coated BNAs are used, uncoated bare one while a shift of 3 nm is observed. The results suggested the ability of fabrication a plasmonic device that is sensitive to the environment out of the coupling between the materials which are sensitive to an environment with plasmonic nano-structures.

In 2016, Y. F. C. Chau et al. [95] a general analysis of the proposed structure of a two-dimensional repetitive couple of array (Au CRBPNAs) was done. The study included geometry and material factors that strengthen the intensity of near-field in addition to resonances mode in the optical spectral region using the 3D FEM of Maxwell's equations. The wanted resonance wavelength could be precisely tuned by changing the filling dielectric media and thickness inside the CRBPNAs regarding the range of 300–1800 nm in EM spectra. It is found that sensitivity increment is depending mainly on the intensity of the hot spot due to the existence of hot spots in CRBPNAs to sensitized molecules in nano-scale size. The proposed CRBPNAs showed spectral response showed a good coincidence with the 'optical window' of biomaterial.

In 2016, Y. F. C. Chau et al. [1] analyzed numerically and quantitatively compared the near-field intensities and absorption spectra of SPR modes on a periodic array of BNAs performed by finite element method tuned regarding the range of 400–3000 nm of the optical EM spectrum. They obtained that increasing the number of hollows in BNAs affect on the reduction of the resonance width because the fact that enhancement of the resonance in cavity plasmon is produced from hollow regions. It is worth to mention that the main benefit is the independence of polarization in comparison to the less number of hollows. It is concluded that the main factor for the improvement of the resonance in the Plasmon cavity related to the hotspot region in BNAs is the hollow number. The study of the proposed structure was focused on the shift in the working wavelength, in addition, the improvement of the local fields via the variations in the filling dielectric medium, the thickness of the film, and the number of hollows in BNAs.

In 2017, P. B. Savaliya et al. [96] demonstrated a structure design of vanadium dioxide embedded in Au nano-material to be used as switchable plasmonic NAs working at near-IR optical spectrum. These nano-antennas demonstrate switching the intensity of the electric field improvement between an On and Off states, considering that electrical, thermal, and optical induction could be used. They employed the FDTD numerical method. The findings revealed that the maximum intensity switching ratio at the peak represents the occurring of the tunning (resonance peaks). Knowing, the model investigated a limited range of wavelengths 900-1300 nm was in the near IR spectral region by manipulation of the parameters geometry.

In 2018, V. F. Gili et al. [97] used a structure of single AlGaAs nano-pillar as a hybrid NAs, characterizing a resonant of an apole mode considering the pumping wavelength, surrounded by the designed a ring of Au to enhance the coupling of the light to the nano-structure. Second and third-order harmonic nonlinear efficiency could be enhanced. The enhancement factors were measured to be about to 30 for the second harmonic process while for the third harmonic process is 15. Results revealed that the possibility to achieve tunable metamixers via enhancing the emission efficiency and pump coupling because of the apole mode excitation.

In 2018, E. Sakat et al. [98] demonstrated that a thermal emission enhancement for a SiNx nano-emitter is higher than four orders of magnitude, designed dimer nano-antenna. This result opened the way to the realization of arrays of nano-emitters that could be heated locally and inserted in the gap of resonant nano-antennas, allowing a high modulation rate together with an enhanced thermal emission.

In 2019, M. Hren et al. [99] investigated the optimization steps within the nano-antenna's design used CST studio to perform electromagnetic simulations by modeling various bowtie nano-antenna geometries to obtain an optimized structure based on varying gap distances, side lengths, and layer thicknesses. Their findings are the side lengths of the nano-antennas ranging from 80-110 nano-meters, the gap distances between the nano-antenna pairs ranging from 20-40 nm, and the gold thickness layer ranging from 15-45 nm. The optimized design was found of a 90 nm side dimension followed by a 20 nm gap distance with a 15 nm gold thickness and it is used to aid in biochemical reaction detection.

In 2019, S. V. Gaponenko et al. [100] investigated the possibility of controlling of the excited state decay rate of chlorophyl utilizing the structure design of NAs composed of a single metal and semiconductor NP. It is worth mentioned that the used metal and semiconductor NPs have the ability of suppression reaching to one order of magnitude for radiative decay rate by one order of the magnitude in comparison to that in a vacuum. Considering that the overall suppression decay could not be performed via a metal nano-sphere cannot be performed since the radiative decay slowing down takes place along the similar growth of its nonradiative counterpart only. An improvement of one order of magnitude of radiative decay during the visible range by Si NPs at the normal direction of the emitter dipole moment to the surface of NPs.

CHAPTER TWO

Design Methodology of a Proposed Nano-Antenna and Skin Tissue Model

A numerical method to design a bowtie shaped plasmonic nano-antenna is presented using CST studio suite versions (2017, 2018 and 2019) assisted by Matlab version (9.1.0.441655-R2016b). The first part consists of the suggested design of nano-antennas in two forms single and an array (2×2, 3×3, and 4×4) at two different resonance wavelengths (532 and 1064) nm. The sweeping process was done for all designs to select the best one for tumor cell treatment. The final step is the optimization of the structure dimensions to get the optimum designed nano-antenna for the proposed tumor tissue. The performance of every design is investigated. The second part is to design a proposed tumor in the skin tissue model with certain dimensions regarding the environment (air). This structure is exposed to the plasmonic nano-antenna structure to show the mutual influence for all designs. The third part is to calculate the generated temperature inside the tumor through the estimation of the specific absorption rate and the time required for killing tumor cells.

2.1 Design of nano-antenna

From the various type of optical nano-antenna, the bowtie shape is the preferred choice in this study, as compared with a dipole [86]. Plasmonic BNAs is usually designed due to the confinement of the electric field in the gap region, working at higher frequencies, and keeping the whole size much smaller (nano-meter) [41]. Regarding the sharp tips of the two arms of the bowtie antenna, the group and phase velocities of surface plasmonic waves decrease with the distance of propagation and finally become zero [101]. BNAs are expected to possess a relatively broad bandwidth because they represent the two-dimensional analogue of a biconical antenna [93]. The localized plasmonic near-field, which is highly sensitive to the refractive index of its surrounding medium can be tuned by adapting the nano-structure shape. Geometrical parameters such as size, gap distance, height, and bowtie apex angle have a direct effect in the LSPR [102].

2.1.1 Single unit plasmonic bowtie nano-antenna

First of all, initial dimensions are selected to design primary bowtie shape nano-antenna by sitting the length of nano-antenna is (L), the width is (W), the thickness is (T), the apex width is (A), the gap width is (G) and the bowtie apex angle is (Θ^o) [103], as shown in Figure. 2.1.a.

The bowtie structure is normally illuminated by linearly polarized waveguide excitation source along the x-axis (x-polarization). The surrounding environment of the design structure is assumed to be air. as shown in Figure 2.1.b.

(a)

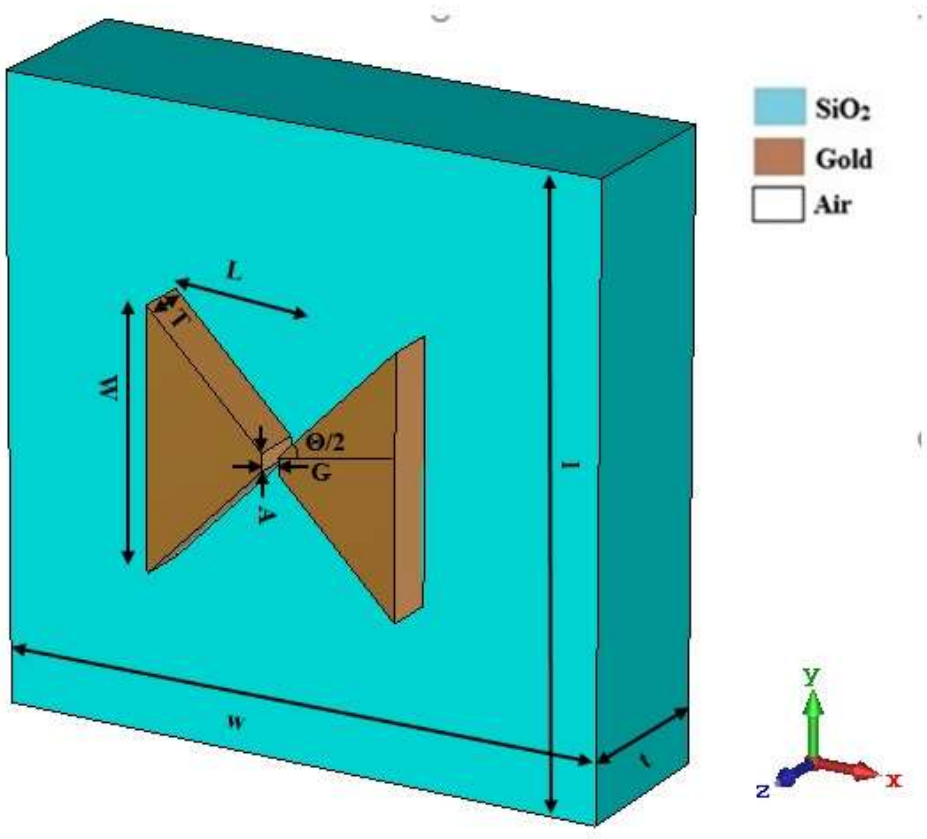

(b)

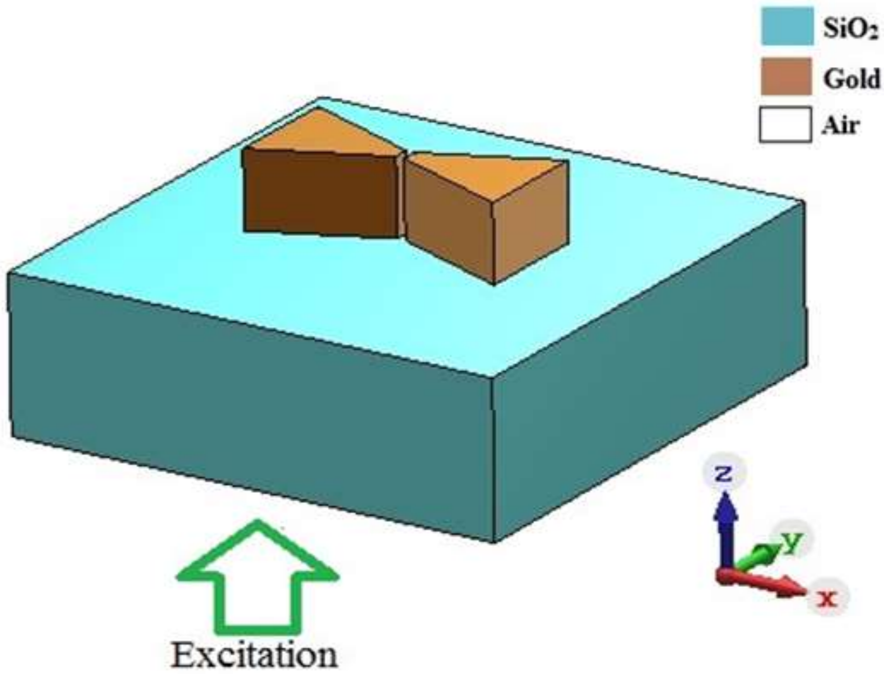

Fig. 2.1 (a): Schematic diagram of single 3D plasmonic nano-antenna with dimensions of the length of nano-antenna is (L), the width is (W), the thickness is (T), the apex width is (A), the gap width is (G) for the Gold and the length (l), width (w), thickness (t) for the SiO_2. (b): The direction of excitation.

2.1.2 Material specification

The gold metal is regarded the suitable choice in the plasmonic structure for the medical applications because of different reasons, non-toxic material, anti oxidized and working at a resonance wavelength of 530 nm. The optical wavelength gives a higher intensity field which represents a good nano-source to treat the tumor cells. The SiO_2 material is selected as a substrate in the designed structure.

The designed nano-antenna (metal/dielectric) consists of the metal Gold (Au) on a substrate of silicon dioxide (SiO_2). The real and imaginary parts of the Au dielectric function with respect to different incident wavelengths are used from experimental data as illustrated in Table (2.1). The refractive index of SiO_2 is 1.5.

Table 2.1. The dielectric constant of Gold at incident wavelengths [104].

Material	Wavelength (nm)	The real part of dielectric constant	The imaginary part of dielectric constant
Gold	532	-4.68	2.42
	1064	-48.45	3.60

2.2 Numerical method

CST studio is allocated to fast and accurate 3D EM simulation of high-frequency problems. The module includes a variety of solvers operating in time and frequency domains.

The time-domain (transient) solver in CST is based on the so-called finite integration technique (FIT). The sequence of the simulation process in CST is illustrated in Figure 2.2.

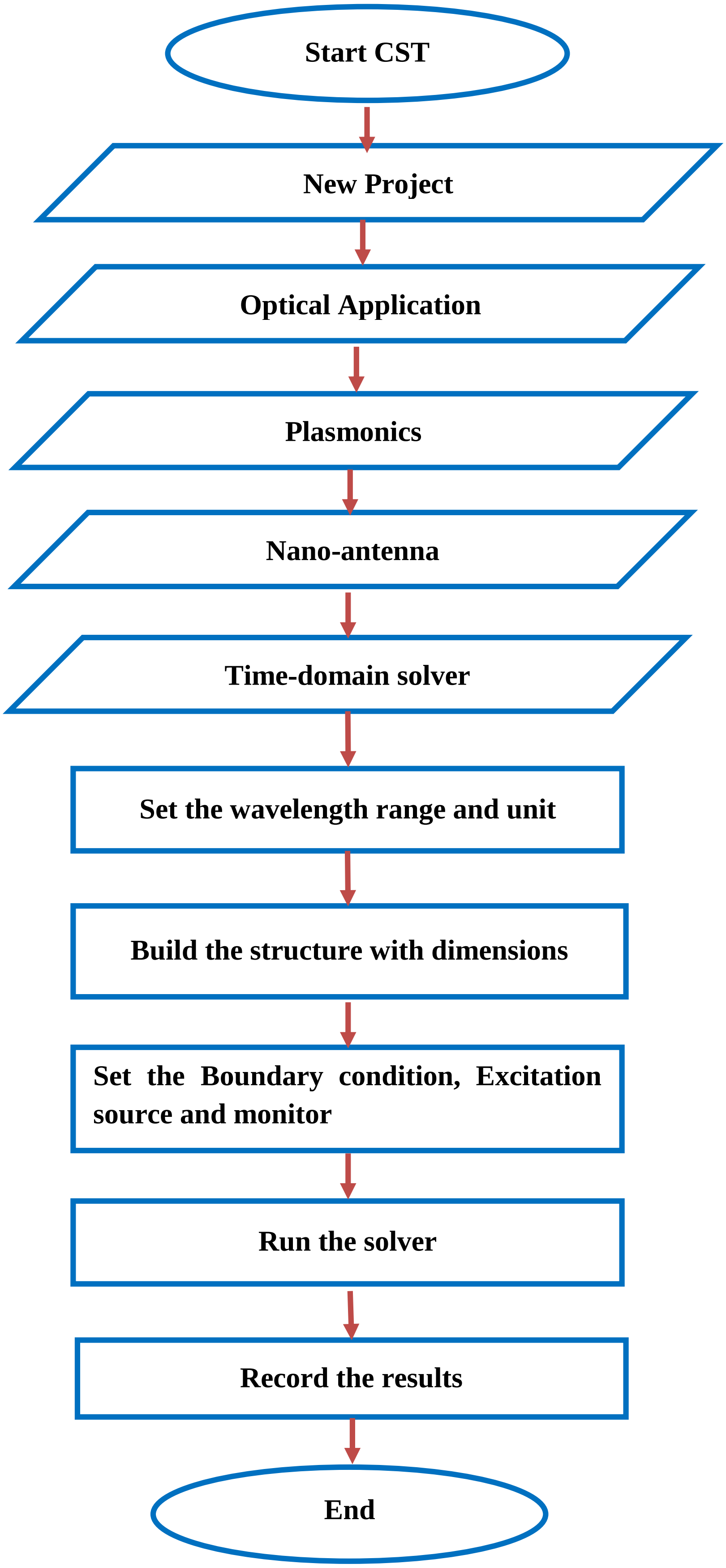

Fig. 2.2 The steps followed during design and simulation in the CST program.

2.3 Sweeping process of plasmonic bowtie nano-antenna

The designed nano-antenna was swept in the CST program for the resonance wavelengths (532 and 1064) nm as shown in Figure 2.3. For each designed nano-antenna unit (i.e., single-nano-antenna), five geometrical parameters are varied over a certain range during the sweeping process. These parameters are (L, G, T, A and Θ°). The sweeping process is applied for all designed NAs (single and an array) for the resonance wavelengths (532 and 1064) nm. The results of this process will be presented in chapter three.

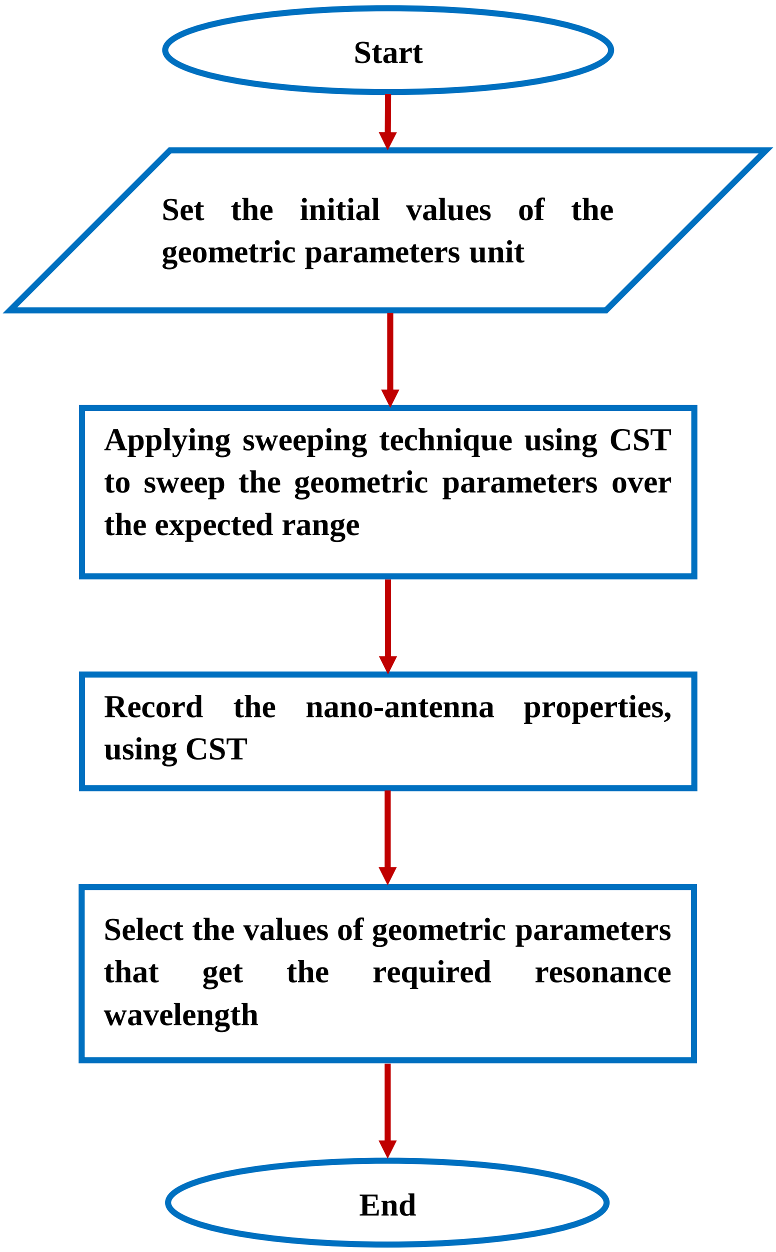

Fig. 2.3 The steps followed to swept the nano-antenna single unit using the CST program.

2.4 Particle swarm optimization of plasmonic bowtie nano-antenna

Particle swarm optimization technique is applied to the designed nano-antenna to optimize the supposed dimensions. For each designed nano-antenna unit (i.e., single-nano-antenna and an array), five geometric parameters are regarded in the PSO process. These parameters are (L, G, T, A and Θ^{o}). The PSO is applied at two resonance wavelengths (532 and 1064 nm).

The following steps are done to optimize the nano-antenna:-

(i) Each nano-antenna is optimized over five-dimensional space representing its geometric parameters using PSO algorithm. The initial values used to run the algorithm are taken from the design based on the parametric study given in section 2.3.

(ii) The results obtained in step (i) initiate the PSO algorithm used to optimize the designed nano-antenna. The PSO trys to get the optimized performance over ten-dimensional space corresponding to the given parameters for two wavelengths (532 and 1064) nm.

The PSO process is applied for the single and an array units of the designed structures for two resonance wavelengths (532 and 1064) nm. The simulation results are obtained using CST packaged will be shown in chapter three (see Figure 2.4). The objective function used in the optimization process is to minimize the reflection coefficient (S_{11}) at the resonance wavelengths.

$$F = \text{Min}\, S_{11} \,|_{\text{resonance wavelength}}$$

The simulation results are obtained using CST packaged and take about 24 hours for single design nano-antenna and about 72 hours for array design nano-antennas. Personal computer DELL (INSPIRON 15-5000 series) having RAM 16 GB and processor Intel Core i7, CPU 2.40 GHz, is used to perform the PSO simulation.

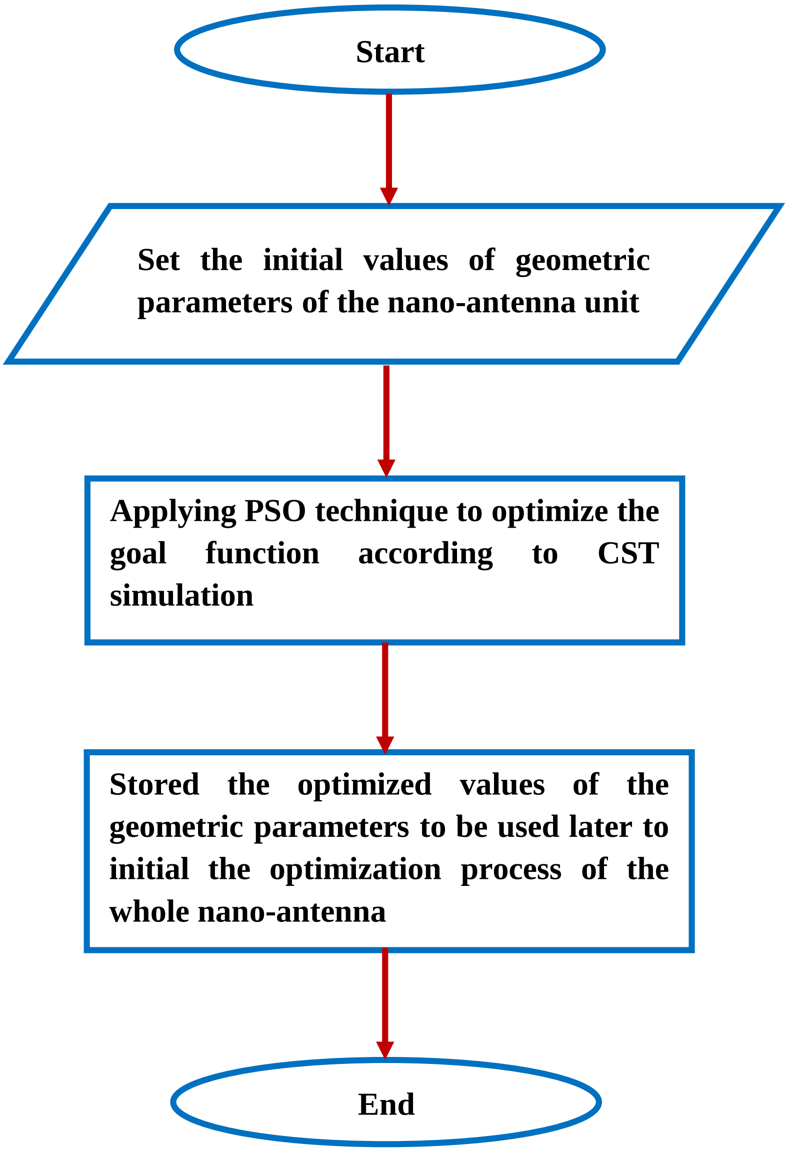

Fig. 2.4 The steps followed to optimize the nano-antenna units using the CST program.

2.5 Initial design of nano-antenna

Based on the single unit of the designed plasmonic nano-antenna, the initial structure of bowtie nano-antenna will be done in both single and an array design working at resonance wavelength (532 and 1064) nm using CST.

2.5.1 Design of single plasmonic bowtie nano-antenna

The designed of plasmonic nano-antenna working in the visible range is directly influenced by different parameters namely (the shape, the length, and the gap dimensions). The more effective parameter in the design of nano-antenna is the gap width. It is useful to mention that the variation of every parameter affects directly on the others so, the comparison between those parameters should be regarded.

2.5.1.1 Single plasmonic nano-antenna working at 532 nm

The dimensions of the designed structure that verifies the resonance wavelength of 532 nm is shown in Figure 2.1 (a). The length of nano-antenna is (L=75 nm), the width is (W=72.13 nm), the thickness is (T=50 nm), the apex width is (A=10 nm), the gap width is (G=5 nm) and the bowtie apex angle is (Θ=35^o) and the length (l), the width (w), and the thickness (t) of the SiO_2 substrate was set as (300, 300, and100) nm respectively.

2.5.1.2 Single plasmonic nano-antenna working at 1064 nm

Figure 2.1 (a) used to indicate the geometry of designed nano-antenna working at resonance wavelength 1064 nm with the length (L=137 nm), width (W=294 nm), thickness (T=60 nm), the apex width (A=20 nm), the gap width (G=20 nm) and the bowtie apex angle ($\Theta=90^o$), and the length (l), the width (w), and the thickness (t) of the SiO_2 substrate was set as (700, 700, and 200) nm respectively.

2.5.2 Array design of plasmonic bowtie nano-antenna

To study the array shape of a nano-antenna, different structures are performed including (2×2, 3×3, and 4×4) arrays. The effect of shape and the behavior are regarded for different resonance wavelengths (532 and 1064) nm. The designed structures are based on the shape of a single unit.

2.5.2.1 Array of bowtie nano-antenna working at 532 nm

The design reported in sections 2.5.1.1 is used as a guideline to design an array of bowtie nano-antenna (2×2), (3×3) and (4×4) structures. See Figure (2.5: a, b, and c) respectively.

The spacing distance between the elements in the designed an array structure is considered to be 300 nm equal to the length of the substrate of the designed nano-antenna working at 532 nm.

(a)

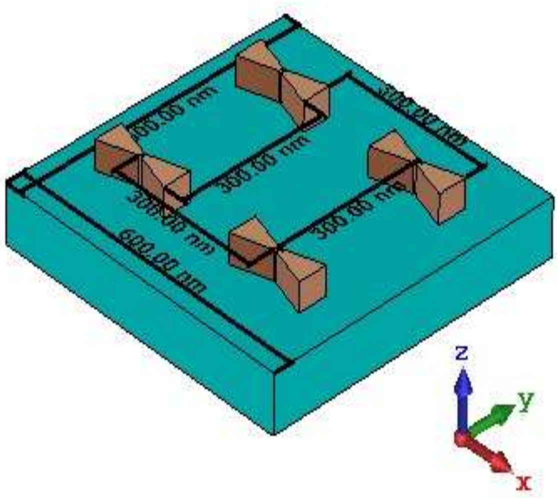

(b)

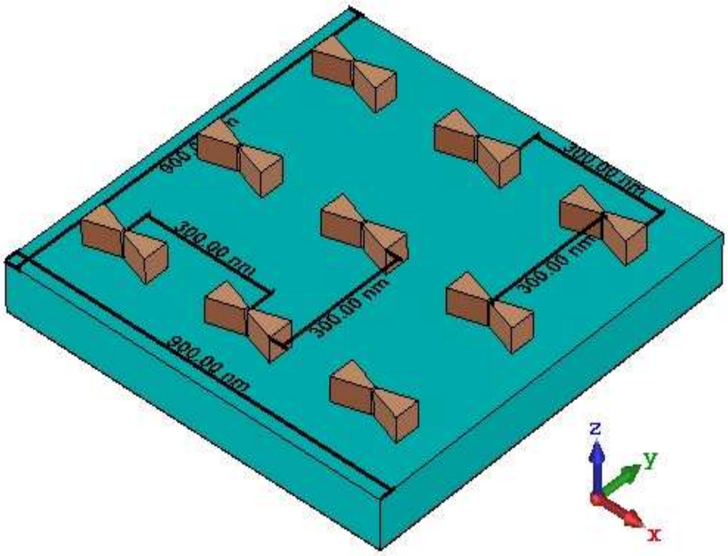

(c)

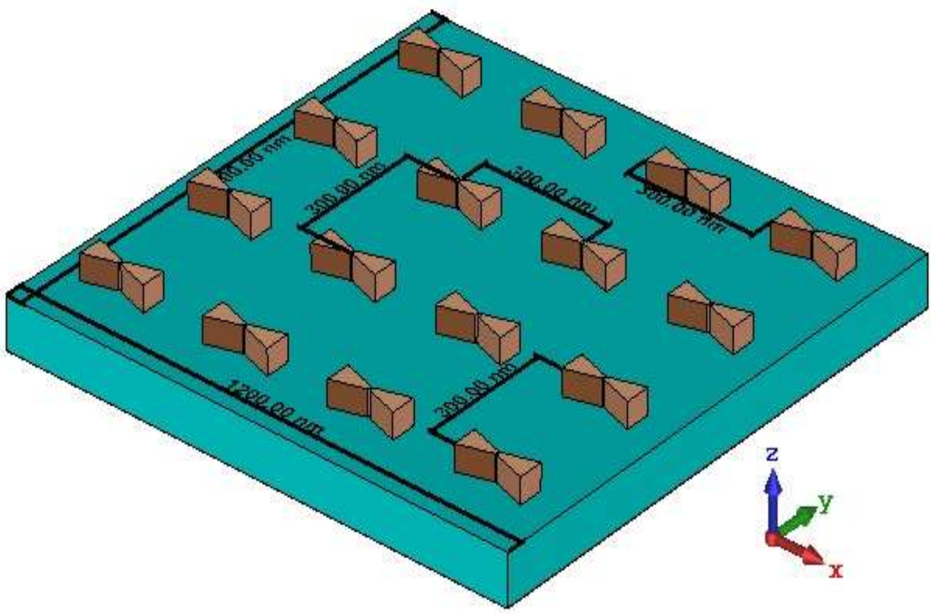

Fig. 2.5 An array of BNAs (a)- (2×2), (b)- (3×3) and (c)- (4×4) structures based on the single unit of the initial design of nano-antenna working at wavelength 532 nm.

Now, the array design with the spacing distance between the gap elements is as the half of the wavelength of 532. The spacing distance becomes 266 nm, so for sure the behavior and the performance of the new design are varied as will be presented in chapter three.

2.5.2.2 Array nano-antenna working at 1064 nm

For array nano-antenna working at 1064 nm the spacing distance between the elements is set at 700 nm similar to the length of the substrate of the single unit structure related to the design reported in section 2.5.1.2 of resonance wavelength 1064 nm. And the spacing distance becomes 532 nm for the half-wavelength distance between each two-gap antennas. The obtained performance of these array structures will be shown in chapter three.

2.6 Final design of nano-antennas

The final design is the obtained optimum design of plasmonic BNAs based on PSO method to new dimensions of the designed structure at a resonance wavelength (532 and 1064) nm for both single and an array structure nano-antenna.

2.6.1 Optimum design of single bowtie nano-antenna

The resonance wavelength is obtained after applied the PSO on the single structure nano-antenna in section 2.5. for both resonance wavelength (532 and 1064) nm.

2.6.1.1 Single design at resonance wavelength 532 nm

The optimum dimensions of the designed structure at a resonance wavelength of 532 nm are illustrated with the dimensions as mention in Fig.2.1 (a) as the length of nano-antenna is (L=80.015 nm), the width is (W=61.22 nm), the thickness is (T=54.13 nm), the apex width is (A=9.74 nm), the gap width is (G=4.65 nm) and the bowtie apex angle is (Θ=35.667°) considering the length (l), the width (w), and the thickness (t) of the SiO_2 substrate are set as (300, 300, and 100) nm respectively.

In the case when the substrate dimension becomes half of the resonance wavelength 532 nm, so for sure the behavior and the performance of the new design single structure will vary as will be presented in chapter three.

2.6.1.2 Single design at resonance wavelength 1064 nm

The optimum dimensions of designed nano-antenna working at 1064 nm with length (L=135.985 nm), the width (W=290.46nm), thickness (T=65.28 nm), the apex width (A=18.62 nm), the gap width (G=20.20 nm) and the bowtie apex angle (Θ=89.97°), regarding the length, the width, and the thickness of the SiO_2 substrate are set as (700, 700, and 200) nm respectively.

As the dimension of the substrate become half of the resonance wavelength 1064 nm the structure of single NA will be change and the performance will be show in chapter three.

2.6.2. Optimum of array design for plasmonic bowtie nano-antenna

The PSO is applied to the array structure of nano-antenna, different structures are performed including (2×2, 3×3, and 4×4) arrays for two resonance wavelengths (532 and 1064) nm. The designed structures are based on the structure of a single unit design in section 2.6, and the performance of these array structures will be presented in chapter three.

2.6.2.1 Array of nano-antenna at resonance wavelength 532 nm

The PSO of an array of BNAs (2×2), (3×3) and (4×4) structures as in the section 2.5.2.1 with the spacing distance between gap elements 300 and 266 nm for the wavelength of 532 nm was designed and the performance of this array NA will be presented in chapter three.

2.6.2.2 Array of nano-antennas at resonance wavelength 1064 nm

The optimum array BNAs (2×2), (3×3) and (4×4) structures as in section 2.5.2.2 with the spacing distance between the gap elements 700 and 532 nm based on PSO for 1064 resonance wavelength was built and the characteristic will show in chapter three.

2.7 The proposed tumor tissue model

The proposed tumor represents cancer cells in the skin tissue located in the center of the skin structure as shown in Figure 2.6.

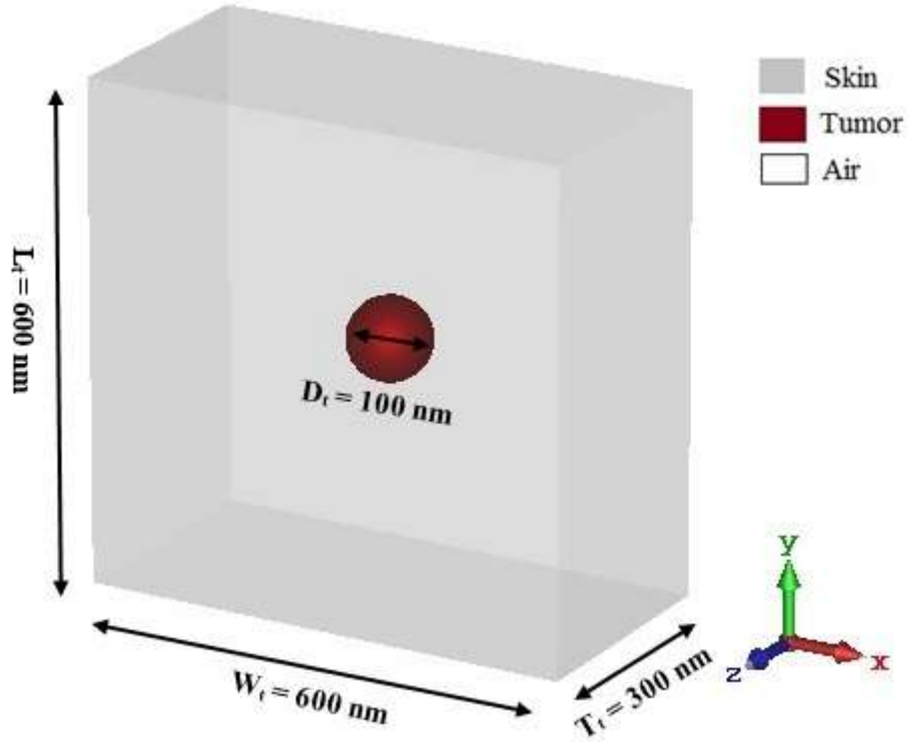

Fig. 2.6 3D Schematic view of the tumor embedded in the skin tissue. The dimensions are (L=W=600 nm and T= 300 nm).

The thermal properties of the tissue are listed in Table 2.2. In addition, the dielectric properties of the tissue play an important role in the investigation of the propagation characteristic of the plasmonic optical nano-antenna. These properties are mainly depending on tissue type and the wavelength of interest.

Table 2.2. The properties of the tissues [105].

Tissue	Thermal Conductivity K (W/m)	Specific Heat C (kJ/K/kg)	Mass Density ρ (kg/m3)
Skin	0.2	3.6	1200
Tumor	0.5	3.6	1050

2.7.1 Exposing the tumor to the designed nano-antenna

The designed tissue is subjected to the plasmonic nano-antenna (single and an array) radiation at different distances, the resulted pattern is shown in Figure 2.7.

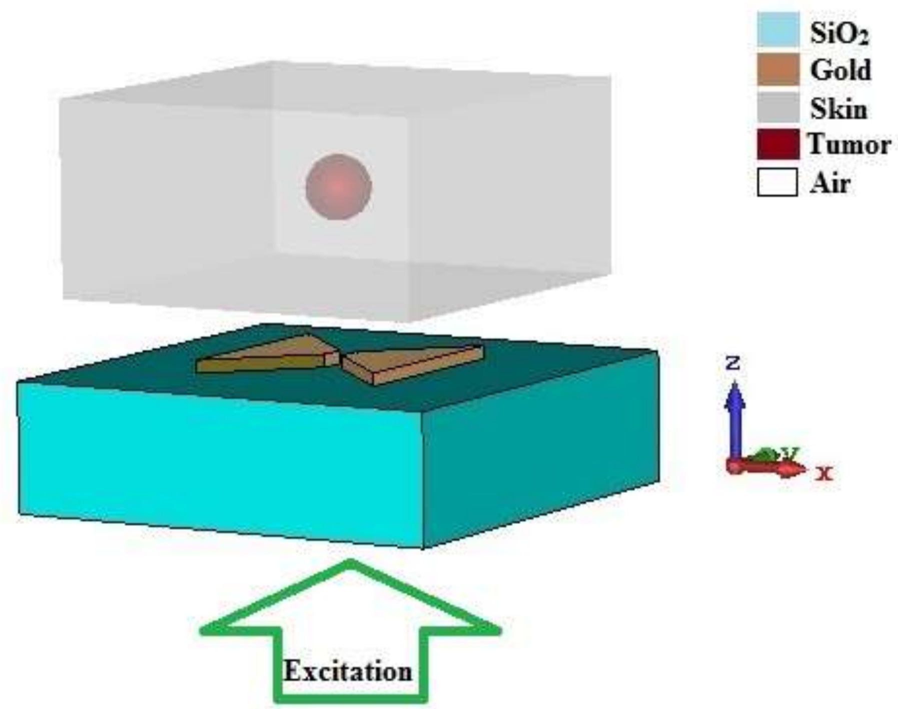

Fig. 2.7 The final pattern of bowtie nano-antenna in front of the designed tissue.

The designed structure was illuminated normally by a waveguide source linearly polarized along the x-axis as shown in Fig. 2.7. The proposed tissue is located in the upper edge of the antenna and centered in front of the gap of the nano-antenna. The structure is surrounded by the air.

2.8 Specific absorption rate

The absorption power from electromagnetic fields causes a temperature rise in tissues. The high levels of absorbed power can cause irreversible tissue damage. The temperature could be calculated from the SAR according to the equations in section 1.14.

For the wavelengths and half wavelengths of (532 and 1064) nm of the optimum designed nano-antenna (single and an array), the SAR and time required for killing tumor cells could be estimated in the proposed design tissue. The result for each case will be presented in chapter three. The point SAR inside the proposed tissue could be estimated at distances (100, 200, 300, and 400) nm respectively. Then, the temperature distribution in the tumor could be calculated.

The side views of proposed tissue model exposed to the designed nano-antenna in case of single unit (and so on in case of an array) to calculate the maximum point SAR of a proposed tissue model for different distances (d= 100, 200, 300, and 400) nm is shown in Fig. 2.8.

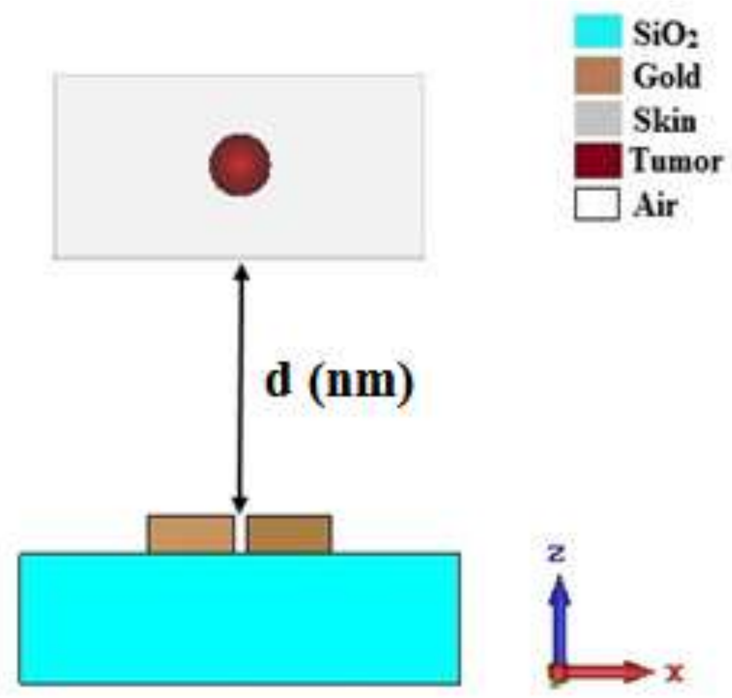

Fig. 2.8 Side view of the proposed tissue exposed to BNAs at distances (d) 100 - 400 nm.

CHAPTER THREE

Results and Discussion

This chapter presents the obtained results for the optimized designed symbols for both single and an array structures using PSO process. The parameters that affect on the performance of the structures NAs are studied through the sweeping process. The results of the performance for all structures including the reflectivity, the near-field intensity and far-field behavior are presented and discussed. Then the effect of the proposed tumor tissue at different distance and types of NAs are investigated. The final step is to calculate the specific absorption rate and hence the temperature estimation is calculated and discussed.

3.1 Optimization design of nano-antennas

It is well known that the supposed dimensions for each design do not represent the perfect case, so, we could not investigate them unless we provide the optimized results. The current research work selects the bowtie shape NAs in different structures (single, an array, and half wavelength array). This design is regarded due to the gap region is a hot spot point source in addition, the group and phase velocities of surface plasmonic waves decreases with the distance of propagation become zero at the sharp tips [72]. The optimization process using the PSO technique was done to find the modified and optimized dimensions for all designs to be recommended in the study.

3.1.1 Optimization of single nano-antennas

The optimum geometrical parameters that obtained via the PSO process in comparison to that supposed initially are listed in Table 3.1. Two wavelengths are investigated (532 and 1064) nm, which represent the wavelength of Nd: YAG laser and its second harmonic, where the two-photo absorption could be taken place. The selection wavelengths attributed to the higher intensity field of optical frequency which could be used to treat the tumor cells.

Table 3.1 The optimum geometrical parameters using PSO technique.

Wavelength (nm)	**Geometric parameter**	**Value (nm)**	
		Before PSO (Initial)	**After PSO (Final)**
532	L	75	80.015
	G	5	4.65
	T	50	54.13
	A	10	9.74
	Θ^o	35	35.667
1064	L	137	135.985
	G	20	20.20
	T	60	65.28
	A	20	18.62
	Θ^o	90	89.972

3.1.2 Optimization of an array nano-antennas

The initial of the parameters are used to estimate the optimum parameters for arrays NAs and for half wavelength arrays. Tables 3.2 and 3.3 illustrates the calculated parameters for both cases. It is well observed that all parameters are varied, so the array structure is built based on these parameters. Regarding the distance between two single NAs, also new parameters are appeared which indicates that very parameters. It is shown that the variation is not equaled owing to its effect.

Table 3.2 The optimum geometrical parameters of an array NAs using PSO technique.

Wavelength (nm)	**Geometric parameter**	**Value (nm)**			
		Before PSO (Initial)	**After PSO (Final) 2×2**	**After PSO (Final) 3×3**	**After PSO (Final) 4×4**
532	L	75	80.013	80.015	80.013
	G	5	4.65	4.65	4.65
	T	50	54.129	54.13	54.129
	A	10	9.735	9.74	9.735
	Θ^o	35	35.667	35.667	35.667
1064	L	137	126.386	124.99	125.611
	G	20	21.829	18.461	18.505
	T	60	60.026	60.236	60.421
	A	20	20.155	20.634	18.370
	Θ^o	90	85.638	82.200	81.171

Table 3.3 The optimum geometrical parameters of half wavelength array NAs using PSO technique.

Wavelength (nm)	Geometric parameter	Value (nm)			
		Before PSO (Initial)	After PSO (Final) 2×2	After PSO (Final) 3×3	After PSO (Final) 4×4
half 532	L	75	82.146	82.431	82.325
	G	5	5.309	4.7	4.73
	T	50	53.826	54.262	53.237
	A	10	10.159	10.925	10.490
	Θ^{o}	35	38.41	38.4	36.623
half 1064	L	137	126.386	124.99	125.611
	G	20	21.829	18.461	18.505
	T	60	60.026	60.236	60.421
	A	20	20.155	20.634	18.370
	Θ^{o}	90	85.638	82.200	81.171

3.2 Parametric study

The influence of geometrical parameters on the performance of the design structures should be considered. The effect of each parameter on the resonance wavelength and the reflectivity is investigated in details.

3.2.1 Single nano-antenna

The optimized parameters effect for both single designs (532 and 1064) nm on the resonance wavelength and reflectivity (S_{11}) are presented.

3.2.1.1 Resonance wavelength 532 nm

Figure 3.1 shows the influence of five parameters on the resonance wavelength of 532 nm.

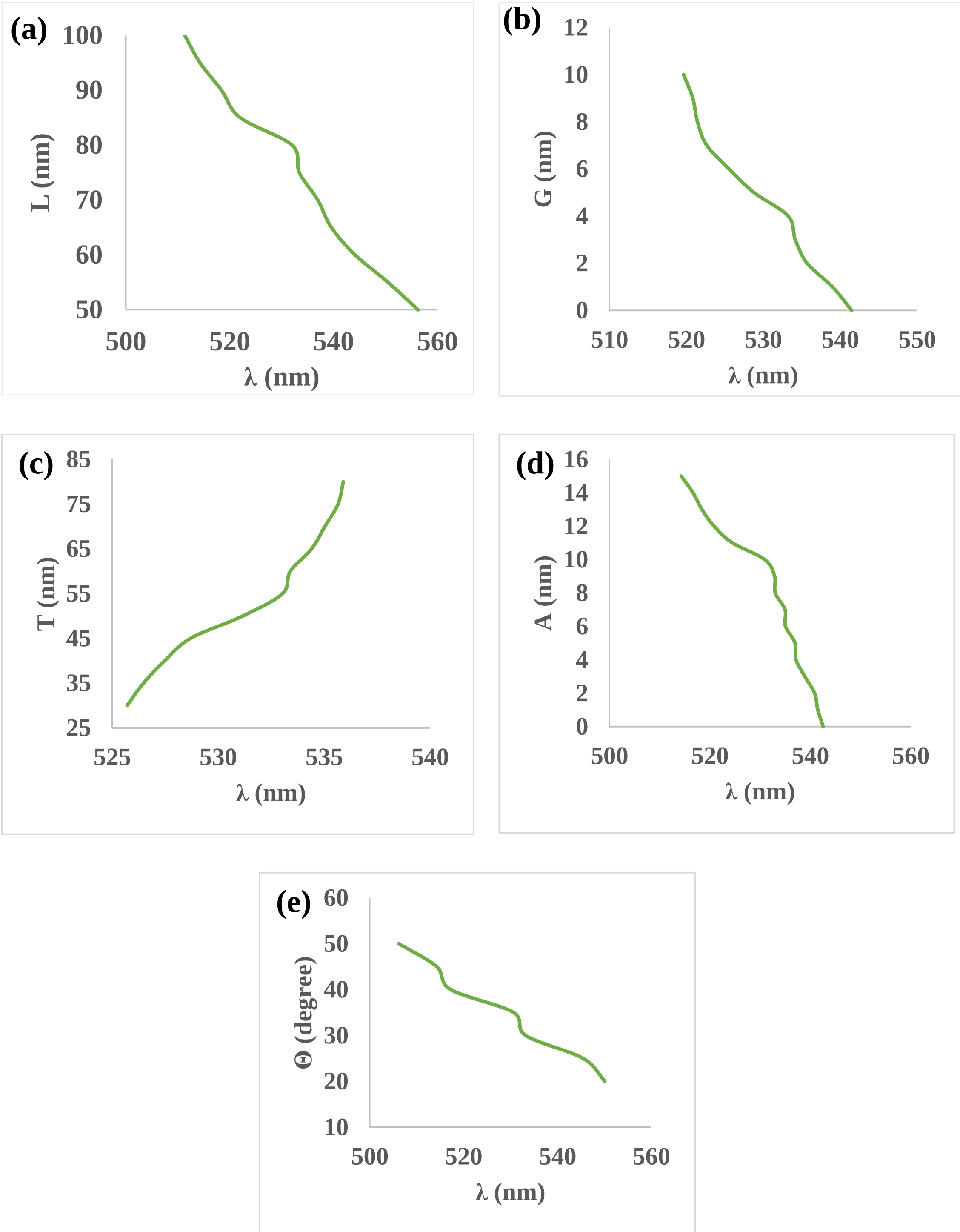

Fig. 3.1 Effect of the geometrical parameters (a) Length L, (b) Gap width G, (c) Thickness T, (d) Apex width A, and (e) Apex angel Θ° on the wavelength.

The behavior of the length as a function of the resonance wavelength is shown in Figure 3.1 (a). It seems that the increment of the length above the resonance rely to a blue shift in the wavelength while the decrease to red shift.

Figure 3.1 (b) shows the effect of the gap as a function of the wavelength. Clear variation was observed in the wavelength due to the changes in the gap or maybe regarded similar to that of the length of NA effect on the resonance wavelength.

The thickness of the gold as a function of the wavelength is also presented in Figure 3.1 (c). Opposite effect is noticed where the increment in the thickness produces red shift while the reduction in it goes to blue shift.

The bowtie apex width also investigated as a function of the wavelength. Obvious influence is noticed where the increase in the apex width above the resonance causes a blue shift while the decrease causes red shift as illustrated in Figure 3.1 (d).

Figure 3.1 (e) presents the behavior of the apex angle as a function of the wavelength. Similar effect was shown to that for apex width which means that the two parameters are related to each other.

The influence of the mentioned parameters on the reflectivity of NAs is considered too.

Figure 3.2 presents the effect of different parameters on the reflectivity at the resonance wavelength of 532 nm. The maximum reflectivity is (-50.57 dB) at the following parameters, L= 80.015 nm, G= 4.65 nm, T= 54.13 nm, A= 9.74 nm and the apex angle is 35.667o.

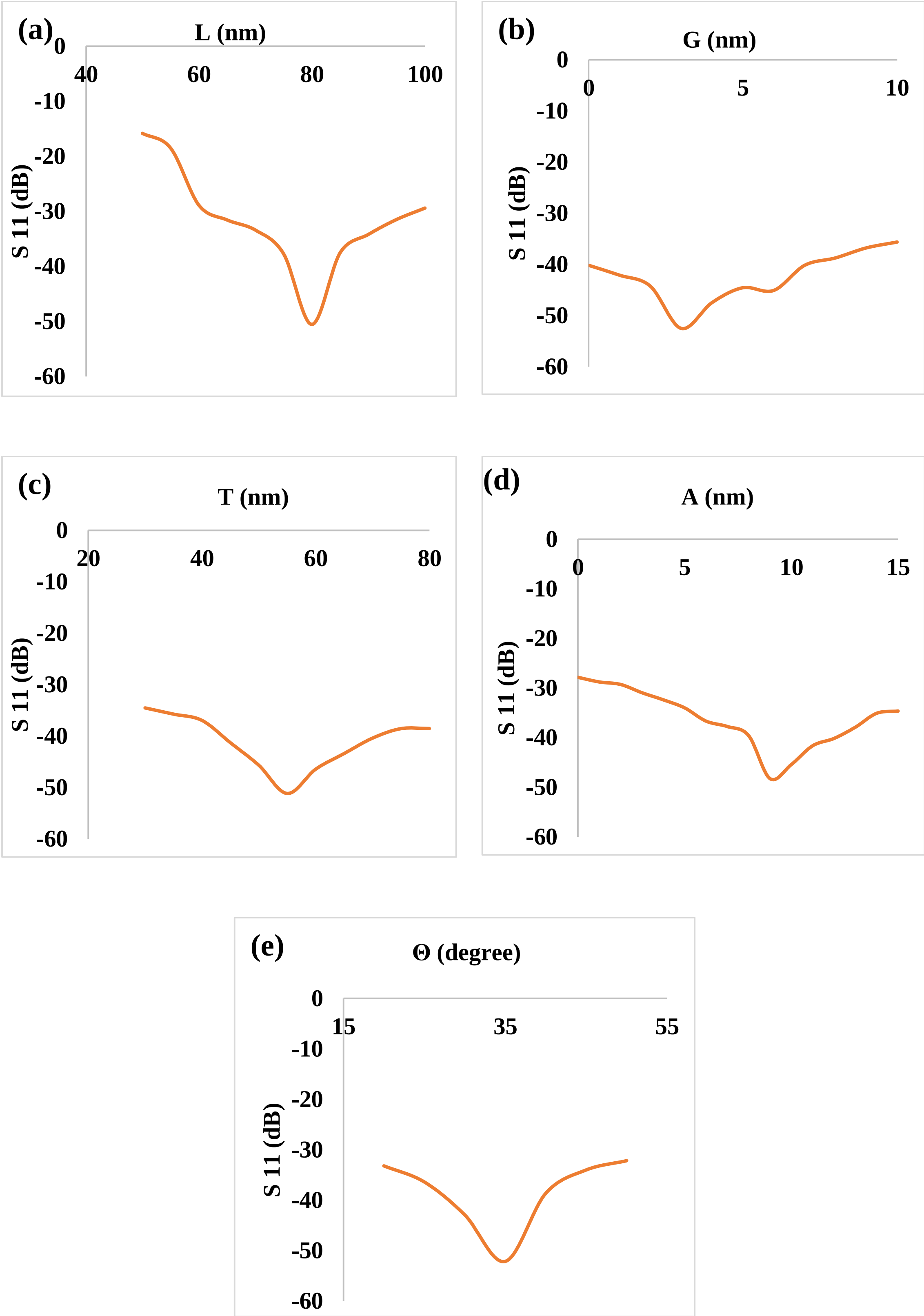

Fig. 3.2 Effect of the geometrical parameters on the reflectivity in dB at the resonance wavelength of 532 nm. (a) Length L, (b) Gap width G, (c) Thickness T, (d) Apex width A, and (e) Apex angel Θ^o**.**

In general, the influence of various parameters on the reflectivity is different but the more effective parameters is the length where the variation is about to 35 dB. Other parameters show that the changes in the reflectivity is about to 15 dB. The dip of all behavior curves is clear which represents the resonance.

3.2.1.2 Resonance wavelength 1064 nm

The second choice of the resonance wavelength is 1064 nm because it represents the half frequency of 532 nm and deeply absorbed by the skin. Similar steps were applied for this wavelength to observe the influence of the geometrical parameters on the resonance wavelength.

Figure 3.3 (a, b, c, d and e) generally presents the behavior of all investigated parameters on the reflectivity of NAs at the resonance wavelength 1064 nm.

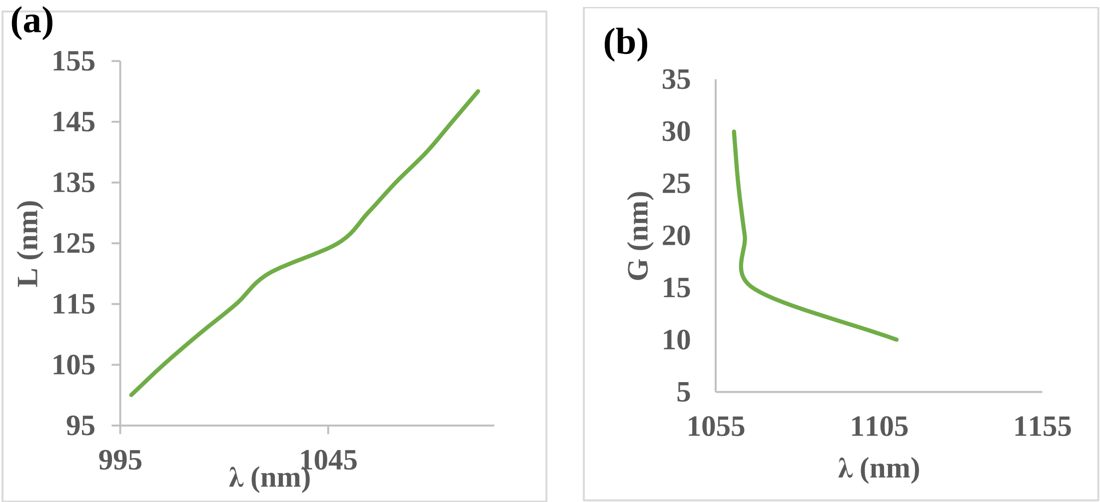

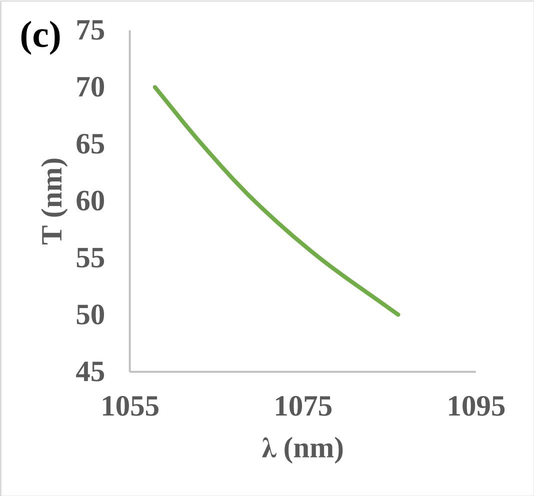

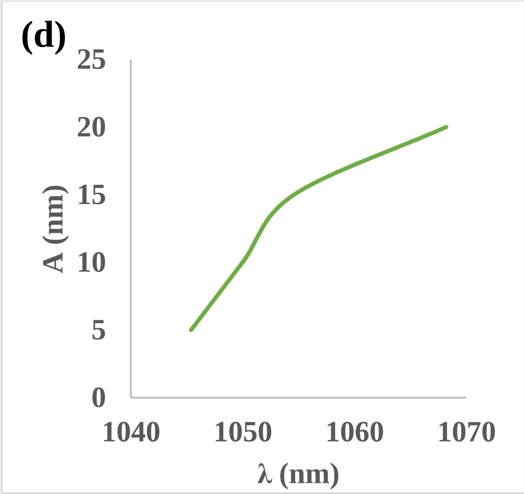

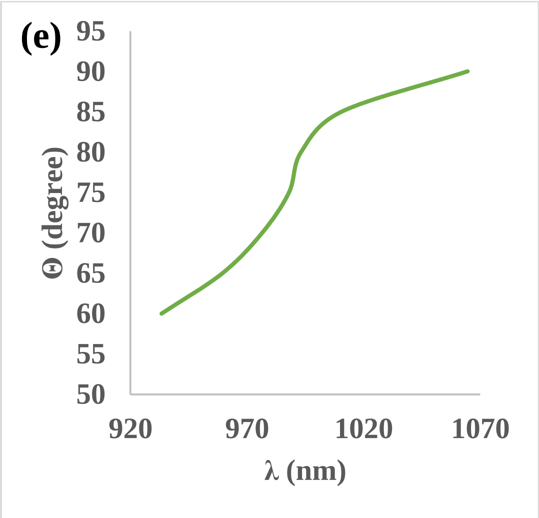

Fig. 3.3 Effect of the geometrical parameters on the resonance wavelength: (a) Length L, (b) Gap width G, (c) Thickness T, (d) Apex width A and (e) apex angel Θ^o.

The effect of the length as a function of the resonance wavelength is shown in Figure 3.3 (a). It is mainly observed that the influence is sharp in both sides (red and blue) where the wavelength is red shifted when the length is increased above the resonance while blue shifted in the case of reduction in the wavelength. So this parameter represents the more effective one due to the clear effect.

Figure 3.3 (b) illustrates the manner of the gap as a function of the resonance wavelength. It is clearly observed the gap width is little bit blue shift then abruptly red shifted in the reduction of the gap width while no important variation in the case of increment in the gap width toward shorter wavelength.

The thickness of the gold seems to be influenced as a function of the wavelength as observed in Figure 3.3 (c). Clear linear behavior is detected where red shift is noticed in the decrease of the thickness below the resonance while the opposite effect in increase of the thickness.

Now the apex width and angle are investigated in Figure3.3 (d). The increment in the apex width causes red shift while blue shift is observed in the decrease of apex width. Figure 3.3 (e) represents the effect of the apex angle on the resonance wavelength. Distinguished behavior is shown where the blue shift takes place when the angle is reduced to 85 degree then no variation is observed till 70 degree then goes down again toward lower degrees (60) degree.

The absorption behavior represented by the reflectivity is regarded. Figure 3.4 (a, b, c, d and e) is the studied parameters as a function of the reflectivity at the resonance wavelength 1064 nm.

The maximum reflectivity is (-35.79 dB) at L=135.985, G= 20.20, T= 65.28 nm, A= 18.62 nm and the apex angle is 89.972°. The reflectivity value is less than that detected for 532 nm which was expected due to less absorption in that wavelength.

It is well noticed that all parameters affect on the reflectivity in different rates but the length is more effective.

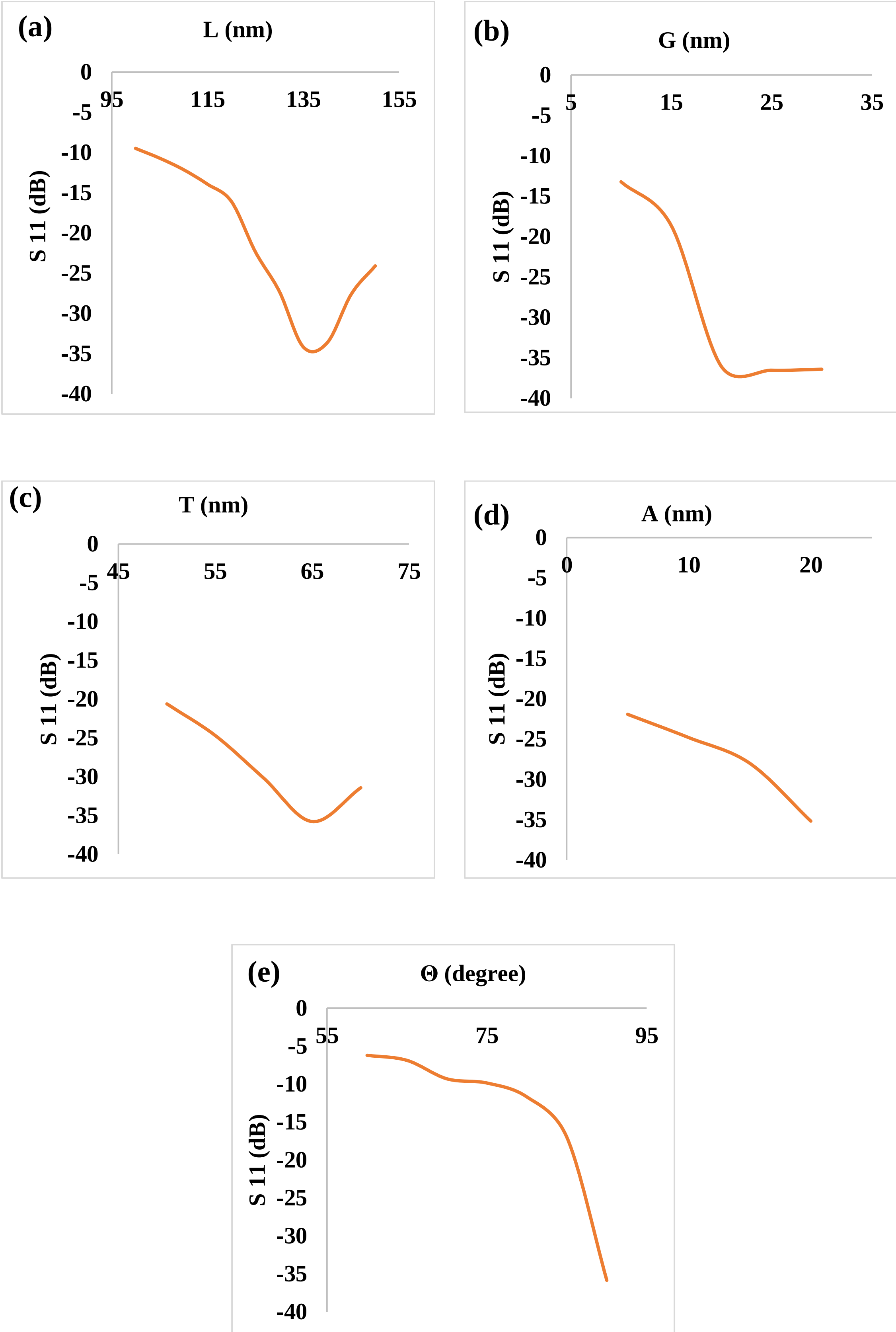

Fig. 3.4 Effect of the geometrical parameters on the reflectivity in dB at the resonance wavelength of 1064 nm. (a) Length L, (b) Gap width G, (c) Thickness T, (d) Apex width A, and (e) Apex angel Θ°**.**

It is observed clearly from the results of optimization that the difference between two values (before and after) the optimization seems little for all parameters but it indicates the accuracy of results and how much affects on the performance of the designs later.

3.3 Performance of nano-antennas

The performance of every design should be investigated well because its importance in each system. So that all design structures are studied in details regarding the reflectivity, near-field and far-field.

3.3.1 Reflectivity of nano-antennas

The reflectivity (S_{11}) behavior of optimized designs including single unite of NA, an array structures (2×2, 3×3 and 4×4) and the array in the half-wavelength distance between two adjacent gaps were investigated.

3.3.1.1 Single unit at two wavelengths (532 and 1064) nm

Figure (3.5) shows the maximum reflectivity at the resonance wavelength of 532 nm for the optimized design. The value of the reflectivity is (-50.57 dB).

The reflectivity behavior of the optimized design at the resonance wavelength 1064 nm is shown in Figure 3.6. The maximum value of the reflectivity at the resonance wavelength is (-35.79 dB). It is clearly observed that there a decrease in the reflectivity which means less absorption because the resonance of the gold is located at about to 530 nm.

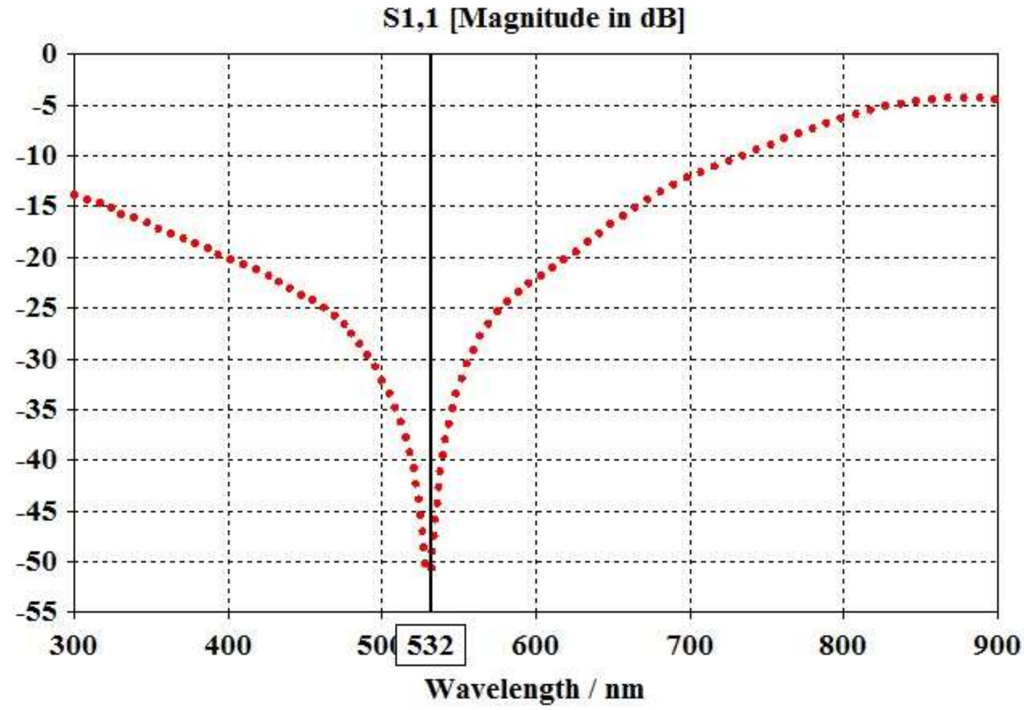

Fig. 3.5 The reflectivity of single NA at the resonance wavelength of 532 nm.

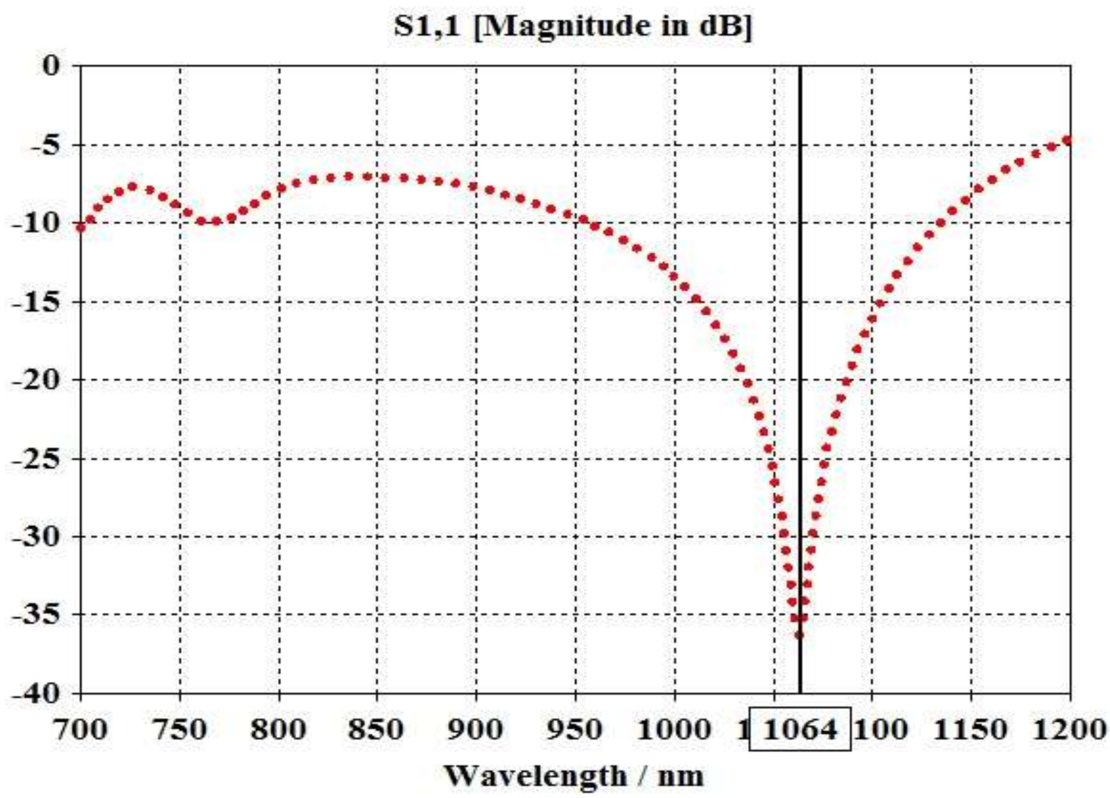

Fig. 3.6 The reflectivity of a single unit of NA at 1064 nm.

3.3.1.2 An Array nano-antenna (2×2, 3×3 and 4×4) at 532 nm

Regarding the optimized design of the single unit a pair of arrays (2×2, 3×3 and 4×4) NAs structures were built as shown in Figure (3.7). It is observed in the arrangement of (2×2) an array that the reflectivity is blue shifted but the behavior is not similar to the single design (see Figure 3.7). The maximum reflectivity is (-17.39 dB).

The second arrangement is composed of (3×3) an array NAs. The maximum reflectivity is (-37.08 dB). It is obvious that the resonance is red shifted to be 661.76 nm but the behavior is well defined. Again, the reflectivity still below the value of the single unit

The third structure is the array of (4×4) NAs. The detected reflectivity is (-33.82 dB). The resonance is red shifted from the resonance of the incident light 669.6 nm but little bit red shifted from the the (3×3) an array.

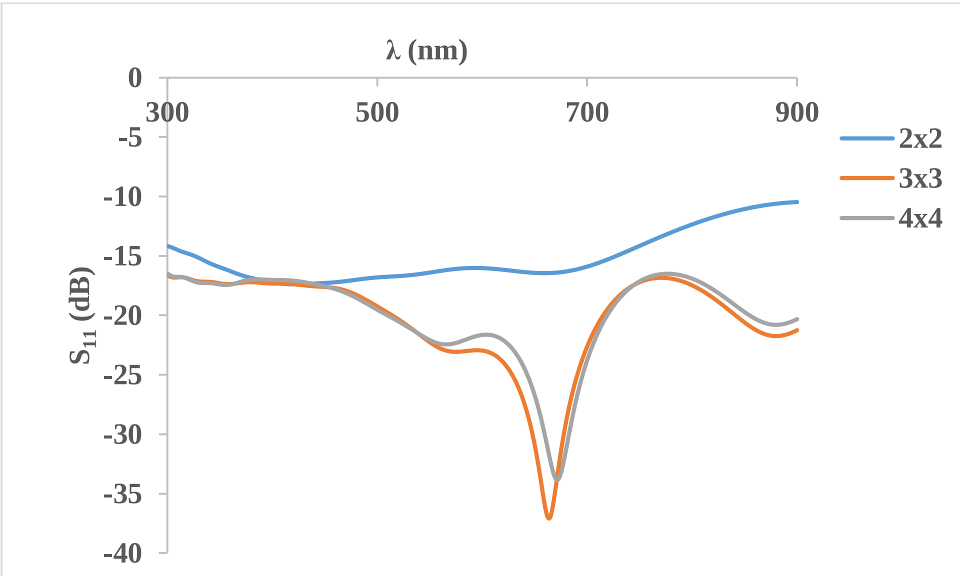

Fig. 3.7 The reflectivity of different NAs array structures (2×2, 3×3 and 4×4) as a function of the wavelength for 532 nm.

3.3.1.3 Half wavelength array (2×2, 3×3 and 4×4) at 532 nm

The other designs of an array NAs consider the distance between two single units of optimized NA equal to half wavelength of the resonance wavelength, so, the reflectivity is definitely varied.

Figure 3.8 shows the behavior of the reflectivity as a function of wavelength for (2×2, 3×3 and 4×4) an array NAs at 532 nm. It is well clear that the behavior and the value of the reflectivity are enhanced in comparison to the previous case where it becomes (-54.73 dB) as observed in Figure (3.8) which means that the distance between single NAs plays an important role in the light absorption in the array structure. It is also observed that resonance wavelength is red shifted to be 853.89 nm while it was blue shifted in the distance larger than the half wavelength.

The reflectivity of other arrays of NAs (3×3 and 4×4) are regarded too. It is shown that the reflectivity is about (-39.59 dB) and (-58.39 dB) for both cases . The resonance wavelength is red shifted similar to the previous case where the shift is 556.93 nm and 690.18 nm for the array NAs (3×3) and (4×4) respectively.

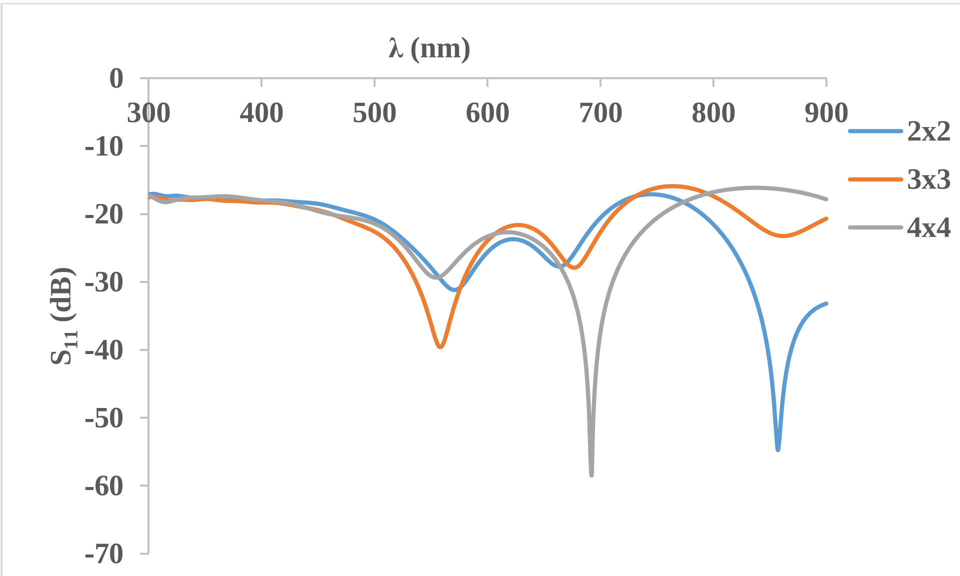

Fig. 3.8 The reflectivity of (2×2, 3×3 and 4×4) an array NAs at the half wavelength as a function of the wavelength for 532 nm.

From the three NAs arrays (2×2, 3×3 and 4×4) at a distance of half wavelength, we can notice obviously that the new PSO structure improves the array with a good reflectivity performance compare to the three NAs arrays (2×2, 3×3 and 4×4). The highest reflectivity is detected at the resonance wavelength (690.18 nm) which represents the larger red shift but still in the visible spectral range. The nature of the spectral shifts in plasmonic nano-structures is still a widely unexplored , with only a few studies aiming at acceptable describing the underlying mechanism.

3.3.1.4 An array nano-antenna (2×2, 3×3 and 4×4) at 1064 nm

Similar steps are done at wavelength 1064 nm to observe the variations that occur for different structures of arrays (2×2, 3×3 and 4×4) in comparison to the single unit.

Figure 3.9 shows the behavior of the reflectivity at three structures of NAs array (2×2, 3×3 and 4×4). Regarding the array of (2×2) arrangement, it seems that the reflectivity is reduced clearly, in addition, no sharp tip is observed may be due to low absorption in this resonance wavelength, however the resonance is little red shifted 1139 nm. The maximum reflectivity is (-13.11 dB).

The array of (3×3) NAs is built and its performance of the reflectivity is detected. It is observed that the resonance is 1151.5 nm red shifted also but less than that of (2×2) an array. The maximum reflectivity is (-9.32 dB).

The array of (4×4) NAs is also presented to show the difference in both the reflectivity and the shifted resonance wavelength. The minimum reflectivity is (-8.52 dB) as illustrated in Figure 3.9 while the resonance is red shifted 1172.4 nm.

It is worth mentioned that all the reflectivity values are less than that for a single design Which means the array designs do not improve the performance.

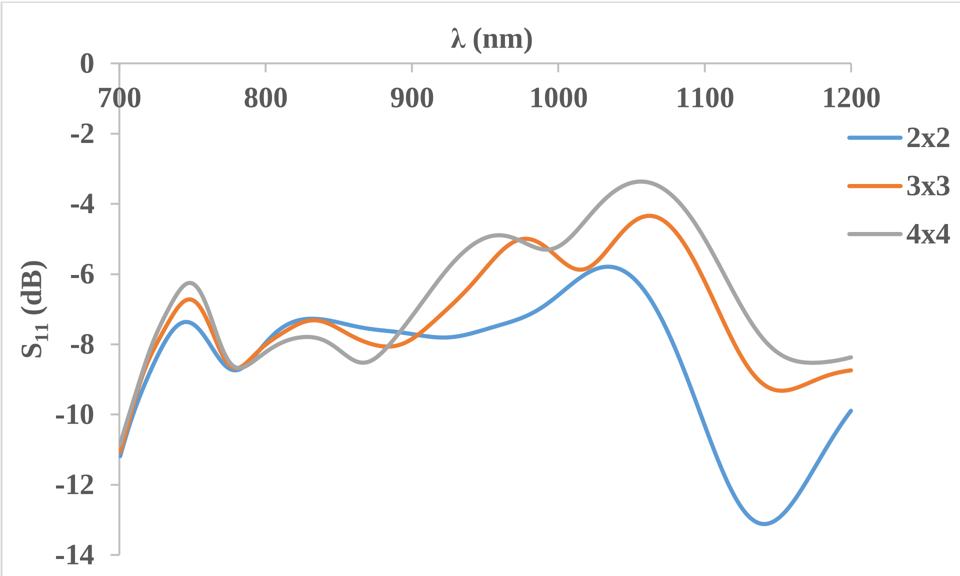

Fig. 3.9 The reflectivity of three NAs arrays (2×2, 3×3 and 4×4) as a function of the wavelength at 1064 nm.

3.3.1.5 Half wavelength array (2×2, 3×3 and 4×4) at 1064 nm

Similar steps were done for the array NAs (2×2, 3×3 and 4×4) at the resonance wavelength 1064 nm regarding the distance between two adjacent single NAs is half of the resonance wavelength.

Figure 3.10 demonstrates the behavior of the reflectivity of those arrays. Considering the array (2×2) NAs at the half resonance wavelength of 1064 nm. Good profile of the reflectivity is noticed while its value (-34.26 dB) is improved related to the array structures at the substrate length of the single unite but it is little bit decreased in comparison to single. The resonance is also low shifted 1058.6 nm.

Now, it should observe the behavior of the reflectivity as a function of wavelengths for two other structure arrays NAs (3×3 and 4×4) respectively. The enhancement for both the behavior and the value of the reflectivity are observed in comparison to the (2×2) an array for the previous case. The resonance wavelength is short range shifted in comparison to the cases that is regarded the distance between two single NAs in one unit. The detected shift is about 1061.3 nm and 1061.9 nm, with reflectivity about (-33.84 dB) and (-33.75 dB) respectively.

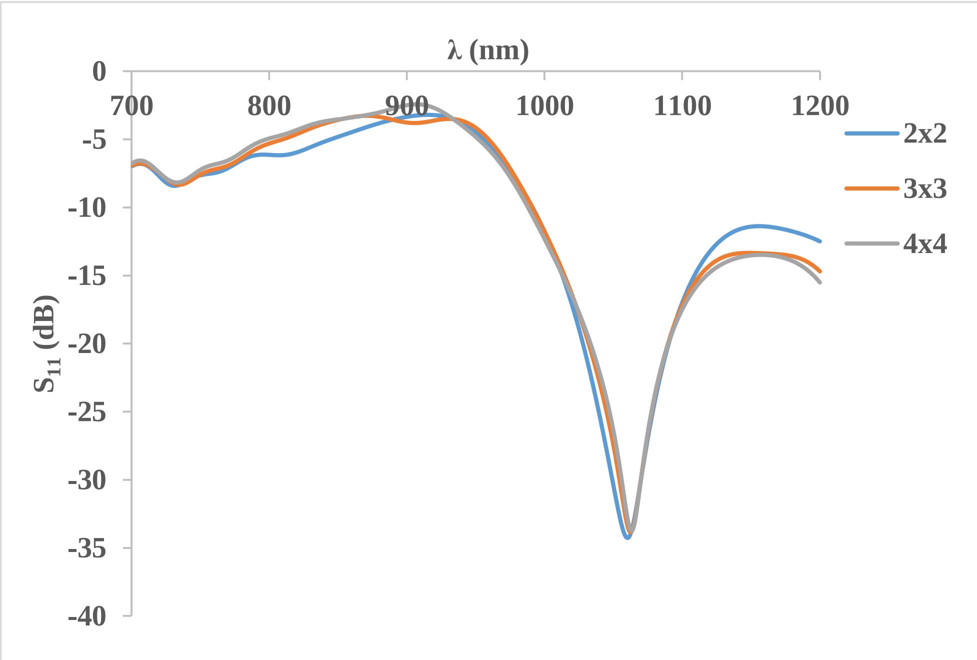

Fig. 3.10 The reflectivity profile of three arrays NAs (2×2, 3×3 and 4×4) as a function of the wavelength at the half wavelength 1064 nm.

The last Figure showed that the arrays (2×2, 3×3 and 4×4) NAs are affected clearly by the variation of changing the distance between two single unit of NAs and that may be where the the reflectivity for all are improved and the observed shift in the resonance wavelength is appeared arround 1064 nm. Those results indicate that the influence of the substrate wavelength (SiO_2) is clear which can be regarded a tunning factor with good profile and value of the reflectivity.

3.3.2 Near-Field of the designed nano-antennas

The intensity of the near-field represents one of the important indications for the performance of every NAs. All structures are subjected to the investigation for both resonance wavelengths.

3.3.2.1 Single unit at resonance wavelengths (532 and 1064) nm

Figure 3.11 shows the distribution of the near-field for single design at resonance wavelength 532 nm. The calculated field is 3.52×10^{8} V/m. It seems that the field is concentrated in the gap region.

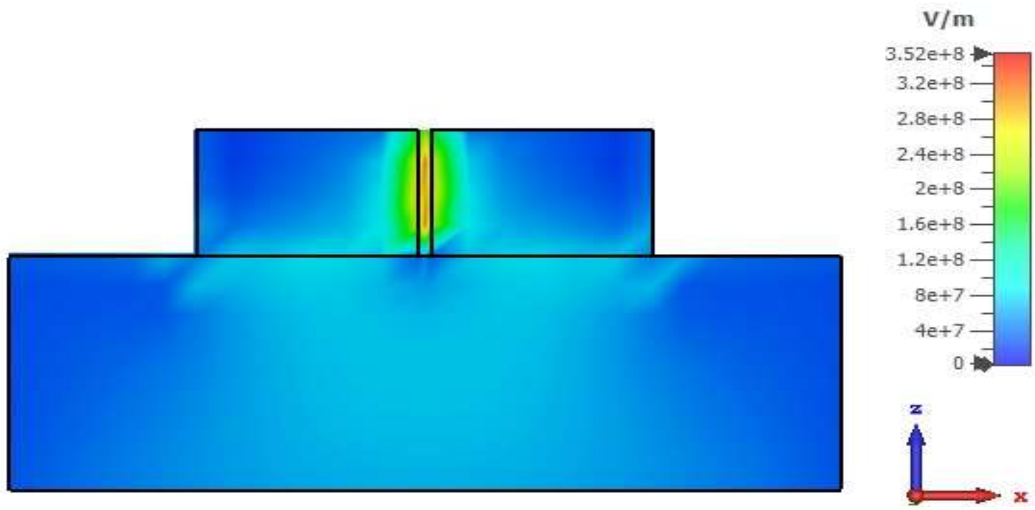

Fig. 3.11 The near-field distribution in the gap NA at 532 nm.

At the resonance wavelength 1064 nm, the field distribution of single NA is shown in Figure 3.12.The intensity field value is 2.77×10^{8} V/m which is less than that of 532 nm due to less absorption. The field is also concentrated in the gap area in addition to a little bit extension to the substrate which indicates the role of the substrate material.

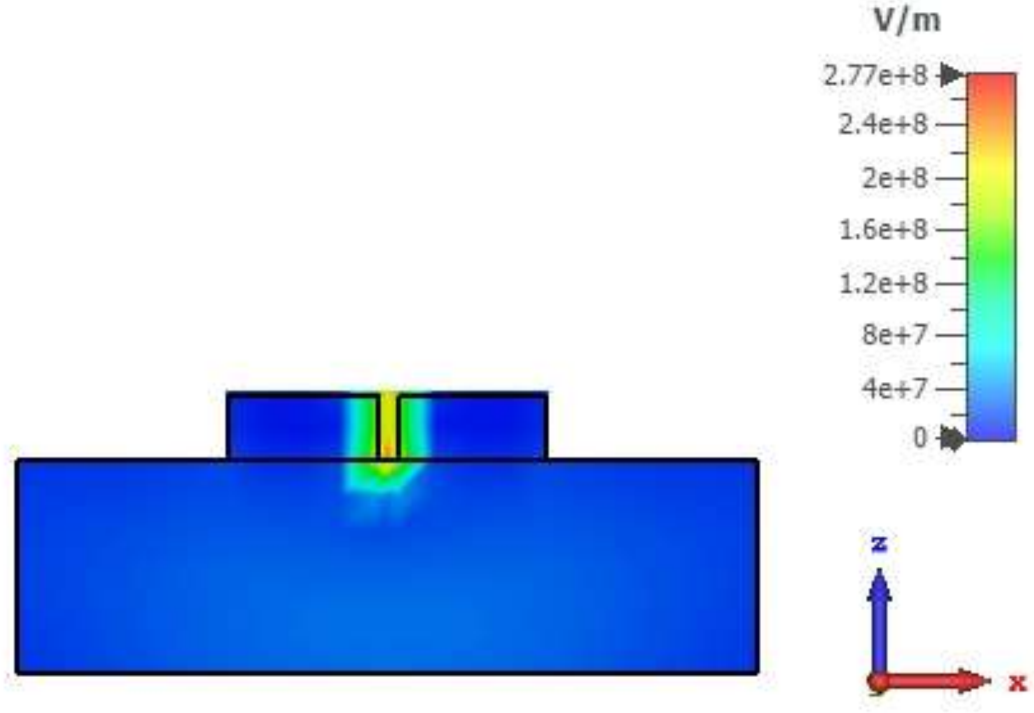

Fig. 3.12 The near-field distribution in the gap of optimum NA at 1064 nm.

3.3.2.2 An array (2×2, 3×3 and 4×4) nano-antennas at 532 nm

To study the effects of the near- field intensity for an array NAs, different structures (2×2, 3×3 and 4×4) are investigated. Figure 3.13 (a, b and c) shows the intensity distribution of the array (2×2, 3×3 and 4×4) NAs at resonance wavelength of 532 nm. It is well observed that the near-field increases at the array of (3×3 and 4×4) in comparison to the single design while it decreases at the array of (2×2). The highest value is for the array (3×3) where intensity field is (1.14×10^8, 6.49×10^8 and 4.77×10^8) V/m for the arrays of (2×2, 3×3 and 4×4) respectively.

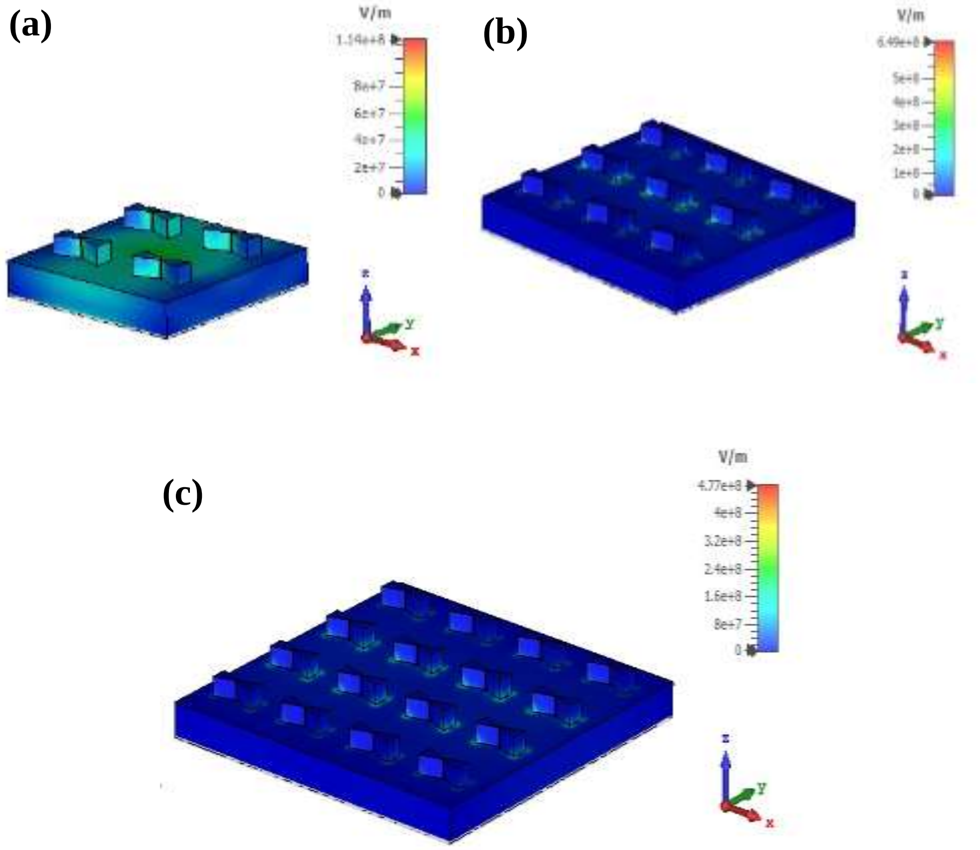

Fig. 3.13 (a)- (2×2), (b)- (3×3) and (c)- (4×4) an array near-field distribution at 532 nm.

3.3.2.3 Half wavelength array (2×2, 3×3 and 4×4) at 532 nm

The near-field distribution of the half wavelength resonance structures including an array of (2×2, 3×3 and 4×4) NAs are taken into account. Figure 3.14 (a, b and c) illustrates the intensity distribution of the array (2×2, 3×3 and 4×4) NAs at half resonance wavelength of 532 nm. The detected field is about (3.68×10^{8}, 2.01×10^{8} and 4.87×10^{8}) V/m for arrays (2×2, 3×3 and 4×4) respectively. The near-field is enhanced for the array (4×4) while it is about to similar for other arrays (2×2 and 3×3).

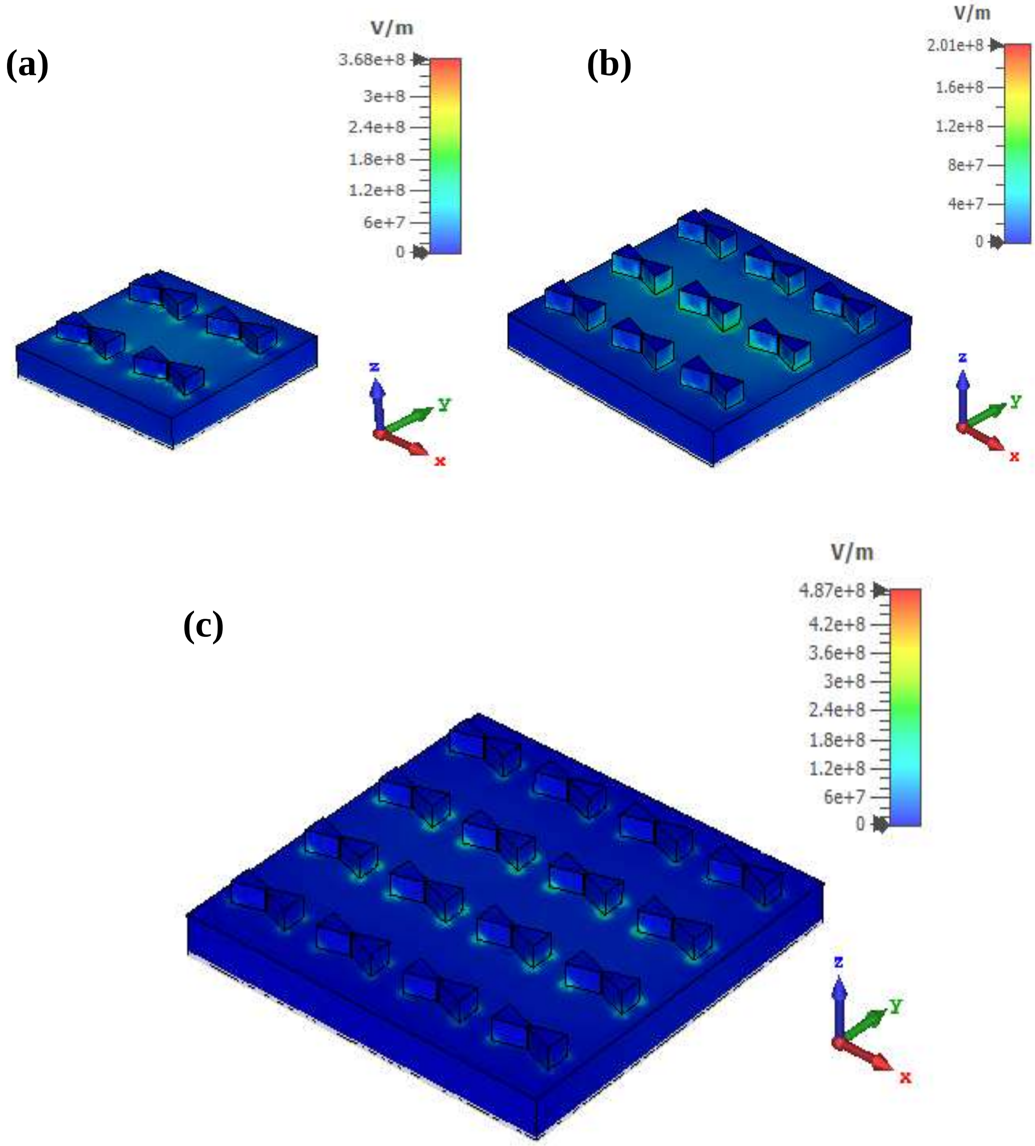

Fig. 3.14 (a)- (2×2), (b)- (3×3), and (c)- (4×4) an array near-field distribution at half resonance wavelength of 532 nm.

3.3.2.4 An array (2×2, 3×3 and 4×4) nano-antennas at 1064 nm

The intensity of near-field for different NAs structures at resonance wavelength 1064 is also presented. The calculated field is (3.27×10^8, 3.61×10^8 and 3.08×10^8) V/m for the array structures of (2×2, 3×3 and 4×4) respectively as illustrated in Figure 3.15. It is well observed that all detected fields are higher than the single unit but still the field of the array (3×3) is the highest which indicate clearly the improvement of the near-field at those arrays.

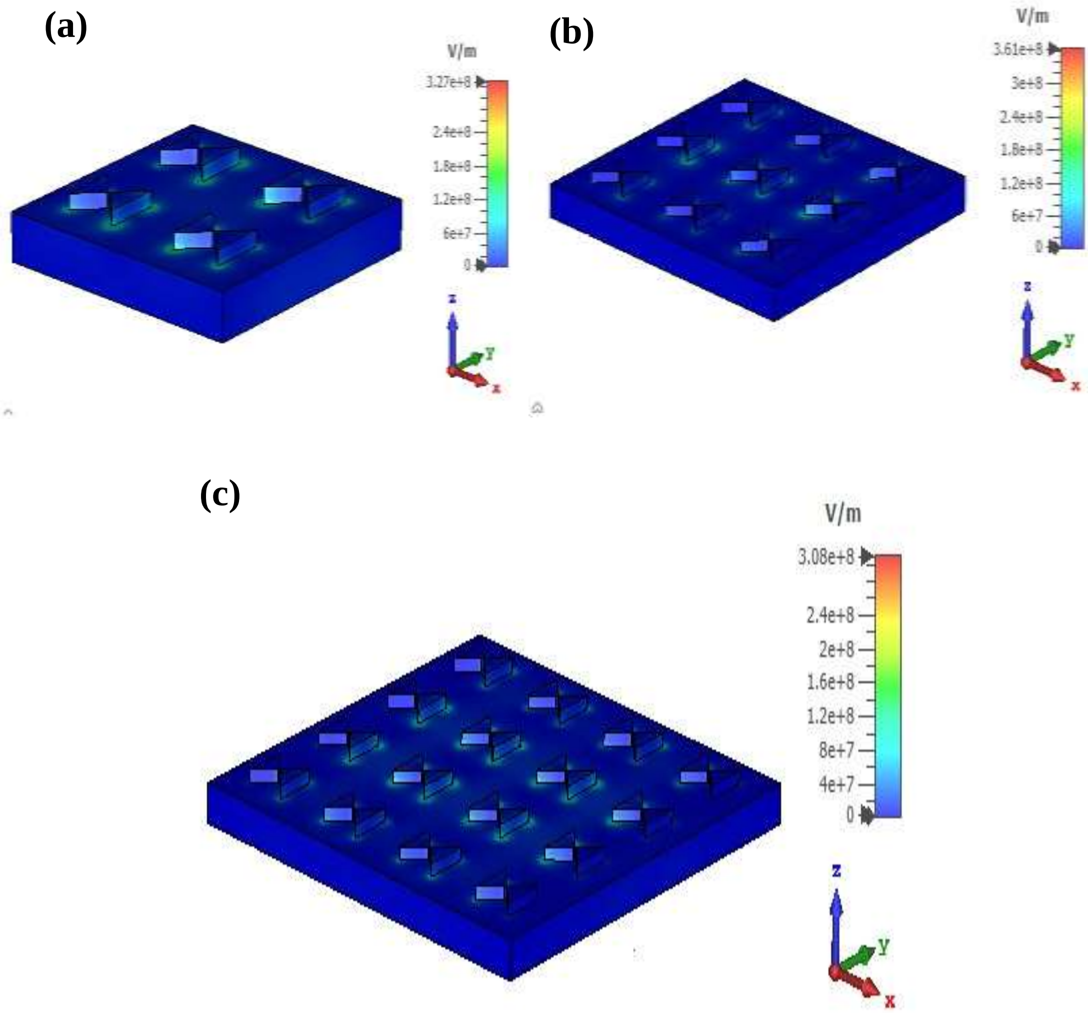

Fig. 3.15 Near-field distribution for an array (a)- (2×2), (b)- (3×3), and (c)- (4×4) at 1064 nm.

3.3.2.5 Half wavelength array (2×2, 3×3 and 4×4) at 1064 nm

The detected near field distribution for the array structures of (2×2, 3×3 and 4×4) at the half resonance wavelength is (7.28×10^{8}, 7.47×10^{8} and 5.39×10^{8}) V/m respectively as shown in Figure 3.16 (a, b and c).

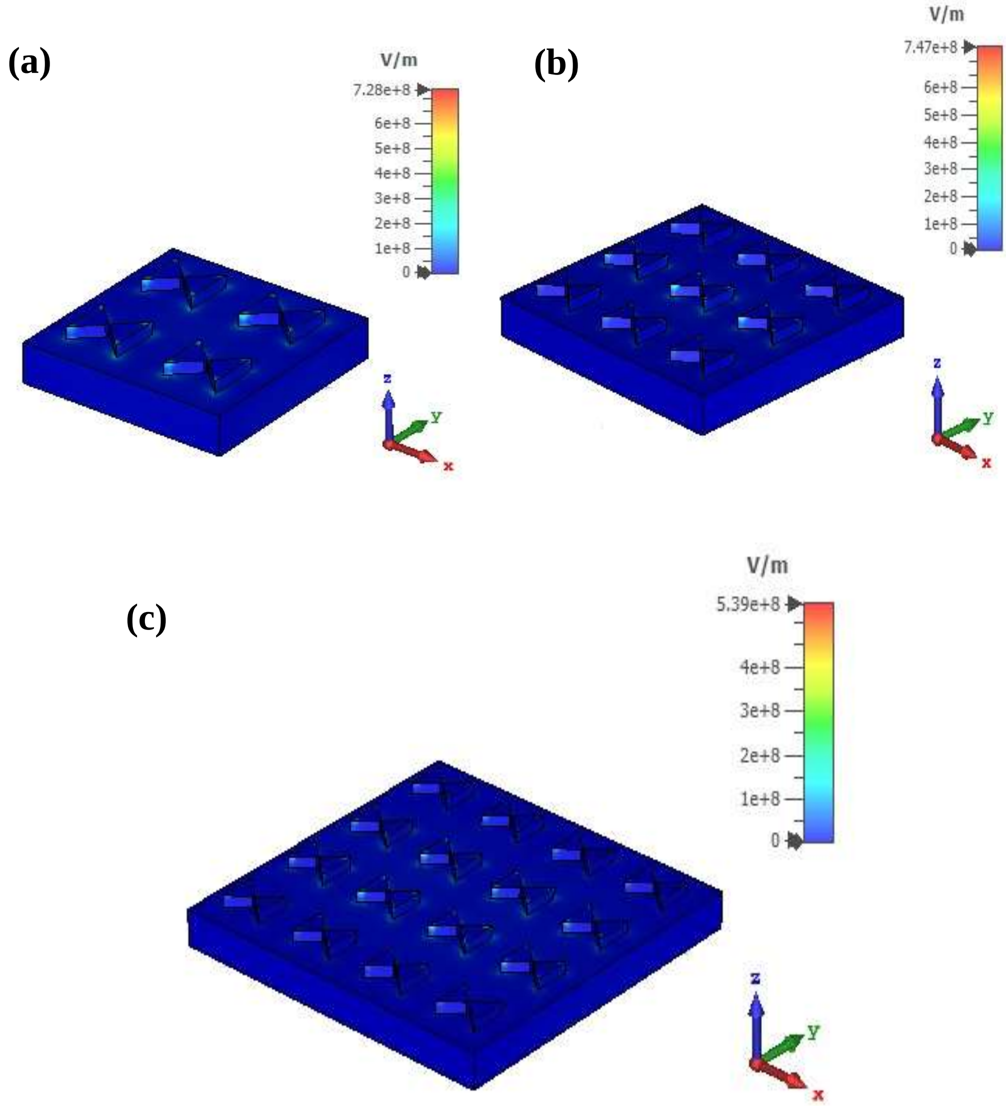

Fig. 3.16 Near-field distribution for an array (a)- (2×2), (b)- (3×3), and (c)- (4×4) at half resonance half wavelength of 1064 nm.

The detected field is similar for the array (2×2 and 3×3) while simple variation is noticed for other an array (4×4) which means that the new structure that regards the distance between two single ANs equal to the half of the resonance wavelength does not affect clearly. In general, the near-field distribution is improved clearly, in addition, it depends mainly on the absorption which is indicated by the reflectivity.

3.3.3 Far-Field of nano-antenna

The far-field intensity is considered one of the effective parameters to determine the effectiveness of the NA to be used in medical applications, so they are investigated for all designs.

3.3.3.1 Single design (532 and 1064) nm

The far-field of 3D optimum design of single NA is regarded for two resonance wavelengths (532 and 1064) nm.

Figure 3.17 shows the far-field distribution in 3D for the resonance wavelength 532 nm regarding the reference plane 1 um. It is observed the regular distribution in front of the gap region. The calculated field is 7.79×10^6 V/m.

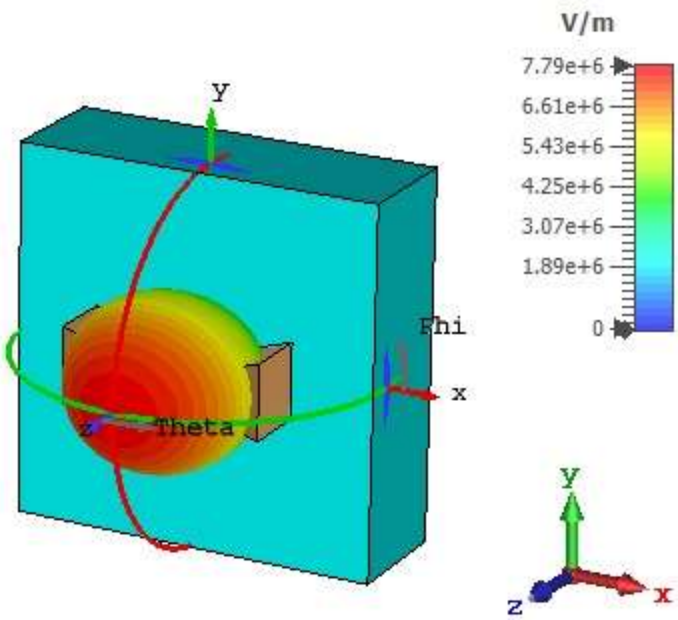

Fig. 3.17 3D far-field of the optimum design of single NA at 532 nm with a reference plane 1um.

The second far-field 3D distribution is for the single design of NA at 1064 nm.It is shown that the field is reduced to be 5.93×10^{6} V/m and the field is extended toward the substrate with similar reference plane as shown in Figure 3.18.

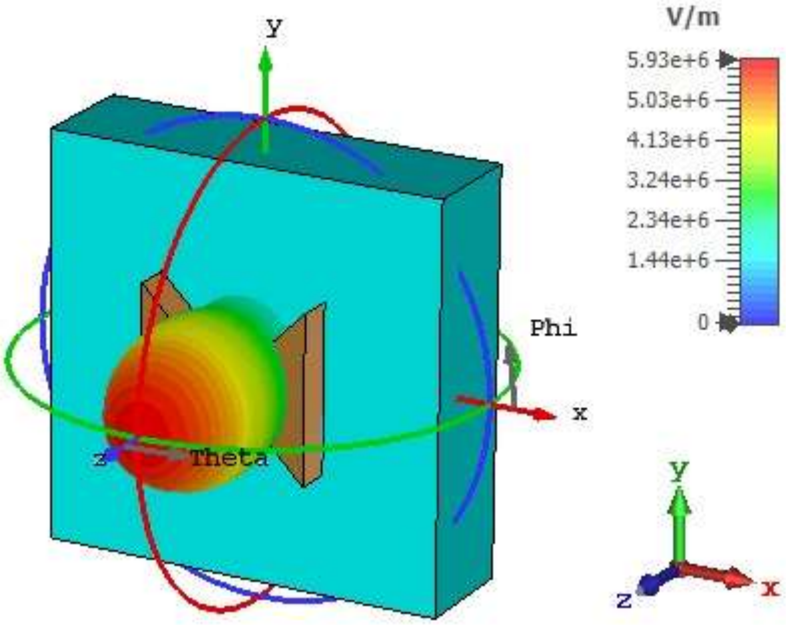

Fig. 3.18 3D far-field of the optimum design of single NA at 1064 nm with reference plane 1 µm.

3.3.3.2 An array (2×2, 3×3 and 4×4) nano-antennas at (532 and 1064) nm

The far-field behavior for an array NAs (2×2, 3×3 and 4×4) should be regarded and demonstrated.

Figure 3.19 (a, b and c) presents the 3D distribution of far-field for an array NAs (2×2, 3×3 and 4×4) patterns at 532 nm.

It is clear that the field is concentrated in the center of all patterns but with different values. The far-field intensity is (2.22×10^{7}, 2.03×10^{7} and 2.67×10^{7}) V/m for the array designs (2×2, 3×3 and 4×4) respectively where the higher value is detected for the array of (4×4) unit. The field intensity for (3×3) does not represent an increase rather than the pattern (2×2) which means the increment in the far-field does not depend on the number of arrays which affects clearly on the far-field increase in all cases.

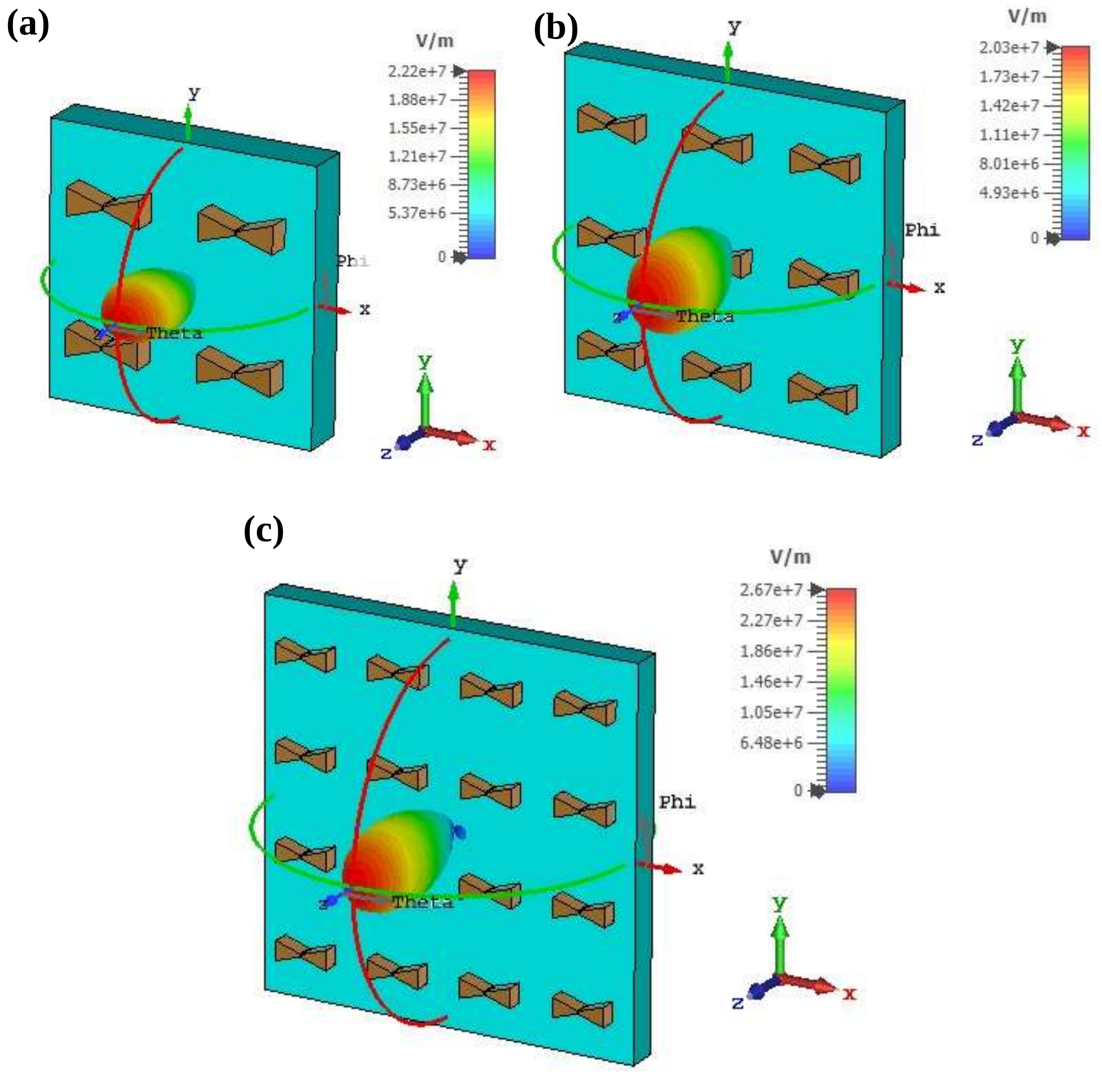

Fig. 3.19 3D far-field of the array NAs (a)- (2×2), (b)- (3×3), and (c)- (4×4) at 532 nm with reference plane 1 µm.

The 3D far-field pattern for arrays (2×2, 3×3 and 4×4) NAs at 1064 nm is shown in Figure 3.20 (a,b and c). It seems that the field is concentrated in the center of patters except the distribution of (2×2). The field intensities are (1.3×10^{7}, 2.23×10^{7} and 9.7×10^{6}) V/m for the distribution pattern of (2×2, 3×3 and 4×4) respectively. In comparison to the resonance 532 nm, a clear difference is observed and proved again that the far-field intensity does not depend on the number of arrays.

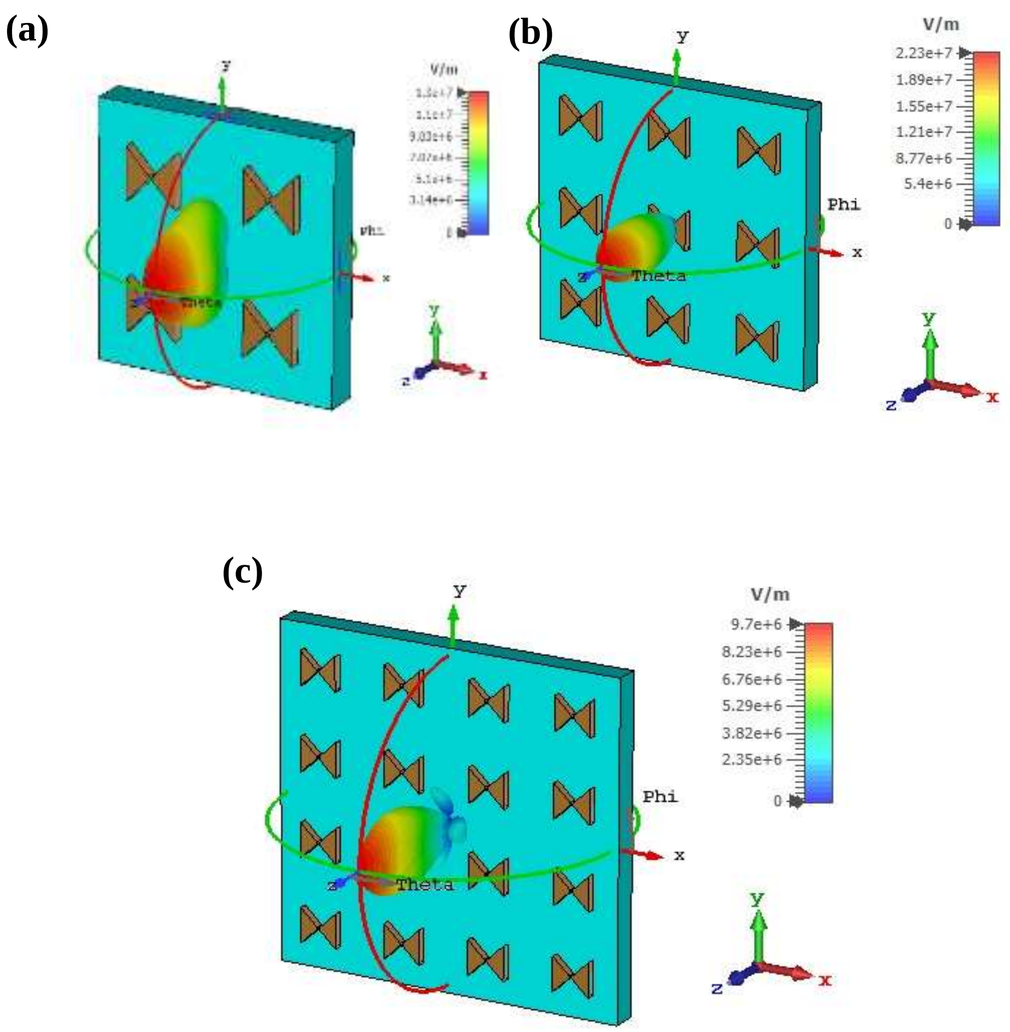

Fig. 3.20 3D far-field of the optimum an array (a)-(2×2), (b)- (3×3) and (c)- (4×4) NAs at 1064 nm with reference plane 1 µm.

3.3.3.3 Half wavelength array (2×2, 3×3 and 4×4) at (532 and 1064) nm

The far-field intensities at the resonance wavelength 532 nm are (9.76×10^6, 2.2×10^7 and 2.25×10^7) V/m for the distribution pattern of (2×2, 3×3 and 4×4) as illustrated in Figure 3.21 (a, b and c). It is observed that the far-field intensity increased as the number of an array increased although the field in general less than that detected in the structures do not depend on the distance between two adjacent single units . Linear increment is observed related to the number of arrays. The distribution field of all arrays are centered for all arrays (2×2, 3×3 and 4×4) which does not observed in the previous cases.

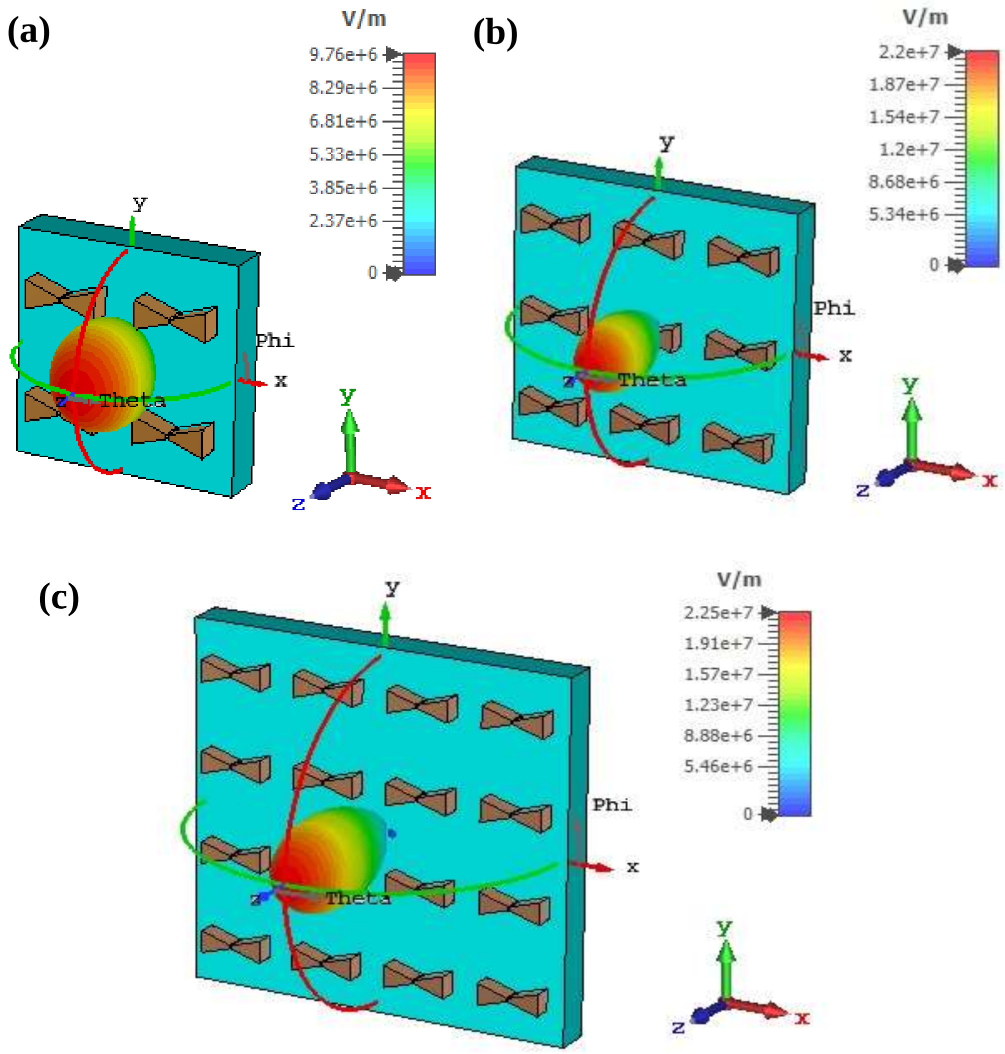

Fig. 3.21 3D far-field of the (a)- (2×2), (b)- (3×3) and (c)- (4×4) an array at the half wavelength of 532 nm with reference plane 1 μm.

The far-field intensities at the resonance wavelength (1064) nm are (1.2×10^7, 1.9×10^7 and 2.54×10^7) V/m as shown in Figure 3.22 (a, b and c) respectively. Again, the far-field intensity increases related to the number of arrays (i.e. the field increases as the number of arrays increases). The detected value of the field do not varied clearly except the far-field an array for (4×4) NAs where it becomes 2.54×10^7 V/m. The dependence of the far-field values on the number of arrays is more clear. The field distribution seems well concentrated in the center of the array structures.

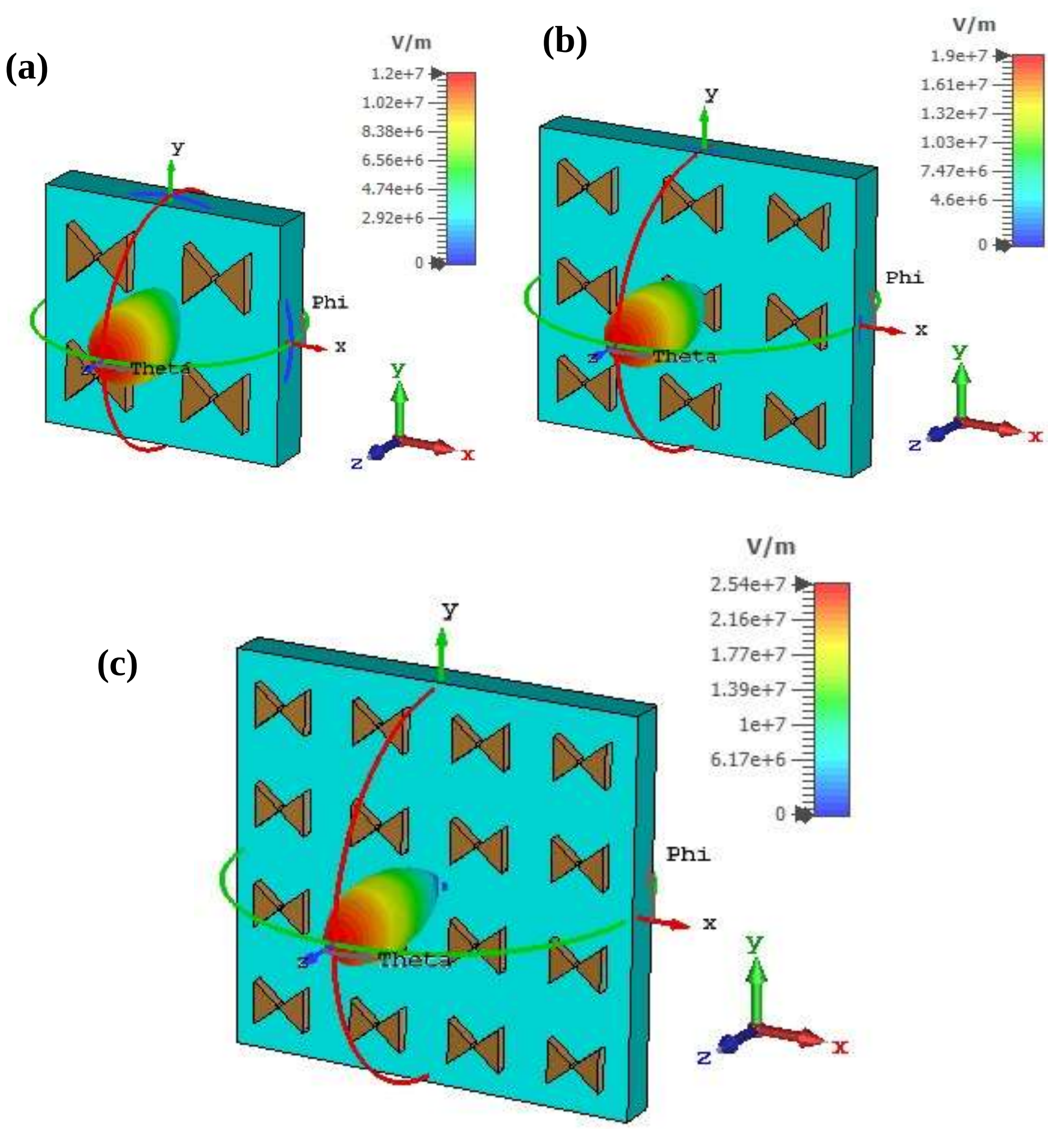

Fig. 3.22 3D far-field of the (a)- (2×2), (b)- (3×3) and (c)- (4×4) an array at half wavelength of 1064 nm with reference plane 1 µm.

From the previous results, it is well observed that the far-field distribution does not depend on the single or arrays structures for both wavelengths (532 and 1064) nm where the maximum far-field detected is 2.67×10^7 V/m for an array NAs (4×4) at 532 nm while it is 2.23×10^7 V/m for an array NAs (3×3) at 1064 nm. Regarding the half wavelength array, linear behavior is shown for 1064 nm while higher far-field for higher an array structure is observed for 532 nm which means that the far-field could be controlled by the arrays, as shown in Figure 3.23.

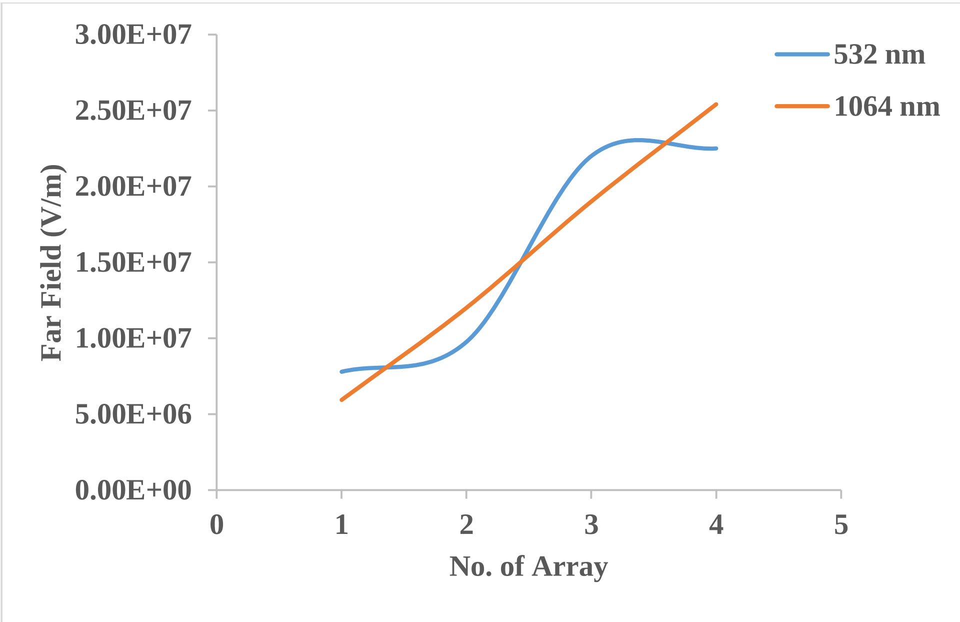

Fig. 3.23 The far-field as a function of single and three arrays (2×2, 3×3 and 4×4) for two wavelengths (532 and 1064) nm.

Generally, the spectral difference between far-field and near-field spectra is an interesting and fundamental property of plasmonic antennas. On the other hand, it needs to be taken into account when designing nano-photonic devices regarding its application**.**

3.4 Field distribution in proposed tumor tissue

The main purpose of the present work is to investigate the influence of different structures on a proposed skin tissue through the study of the far-field distribution in the tissue that is received from NAs after subjecting to the tissues. The tumor tissue dimensions are designed related to three parameters, the position of the tumor inside the skin, the location in the body (skin), and the distance between the NAs and the tumor cells. This part includes investigation the influence of the far-field pattern created by the designed NAs working at two resonance wavelengths (532 and 1064) nm for different distances (100, 200, 300, and 400) nm on the proposed tissues.

3.4.1 Single nano-antenna at 532 nm

The proposed tissue is subjected to the single NA for different distances at the resonance wavelength 532 nm as shown in Figure 3.24. The maximum far-field calculated is (1.3×10^{8}, 7.18×10^{7}, 4.71×10^{7}, and 3.29×10^{7}) V/m in the proposed tumor for the distances (100, 200, 300, and 400) nm respectively. It seems that the better field is detected at the distance 100 nm which represents the suitable distance where the field is concentrated in the tumor. It is well observed that the far-field strength increases for the closest distance from the NA.

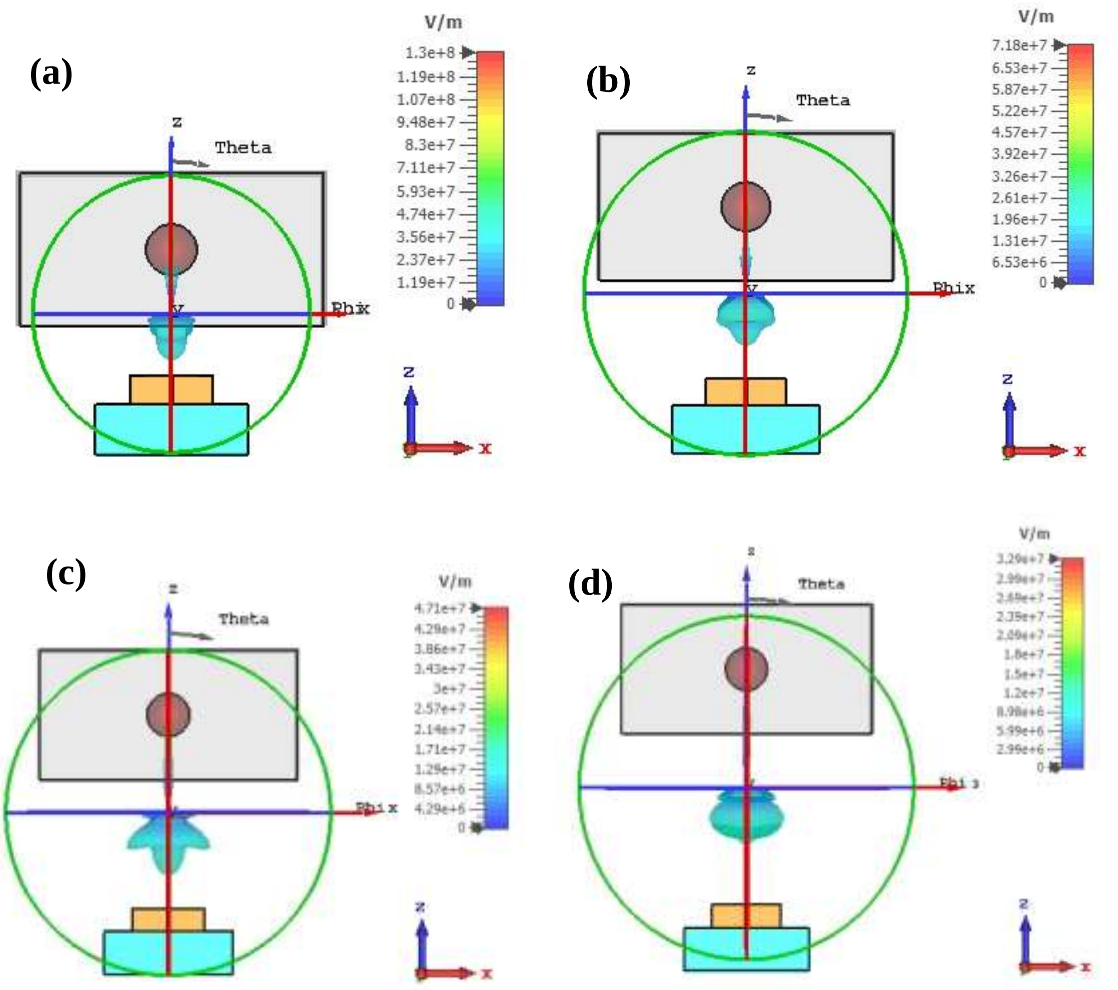

Fig. 3.24 The far-field pattern of 532 nm in the proposed tissue at different distances. (a) 100 nm, (b) 200 nm, (c) 300 nm and (d) 400 nm.

3.4.2 Single nano-antenna at 1064 nm

Figure 3.25 shows the far-field distribution in the tumor embedded in the skin tissue for various distances at the resonance wavelength 1064 nm. The maximum far-field calculated is (8.02×10^7, 3.74×10^7, 2.487×10^7, and 2.49×10^7) V/m in the proposed tumor for the distances (100, 200, 300, and 400) nm respectively. Two notes were detected, first, the far-field for all distances is less than the field calculated at 532 nm, second, the far-field is reduced with increasing the distance where the maximum field is calculated for 100 nm.

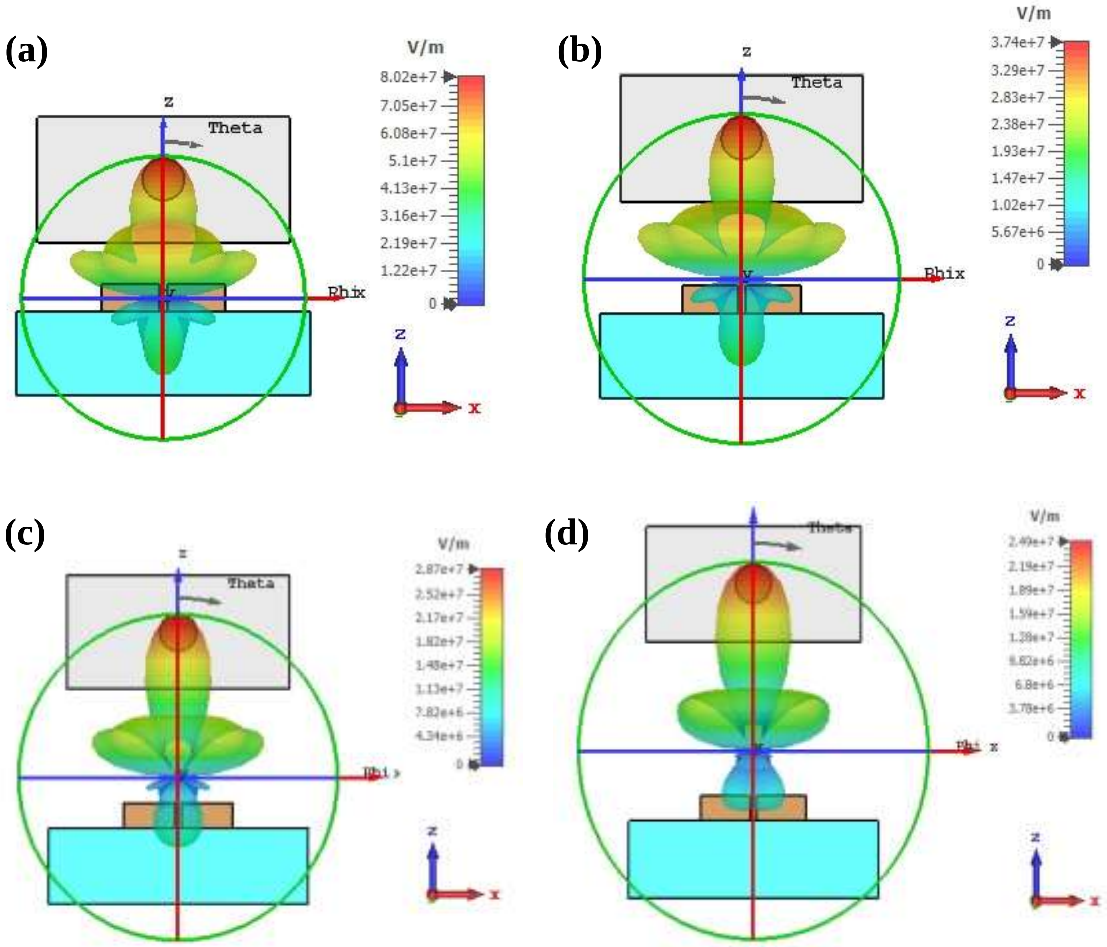

Fig. 3.25 The far-field pattern of 1064 nm in the proposed tissue at different distances. (a) 100 nm, (b) 200 nm, (c) 300 nm and (d) 400 nm.

Figures 3.24 and 3.25 illustrate clearly that tissue is affected strongly on the field. The distribution of the intensity field in the skin tissues is directly influenced by the resonance wavelength and hence its strength. The pattern of the field in the case of resonance wavelength 532 nm is much sharper than in 1064 nm. It is worth noticed that is the field in the tissue is larger, in general, than the incident far-field on the tissues which could be attributed as the reflectivity is varied due to the absorption of the tissues is different than that of the antennas used.

3.4.3 An array nano-antenna (2×2, 3×3 and 4×4) at 532 nm

The maximum far-field calculated is (3.46×10^8, 2.13×10^8, 1.19×10^8, and 1.12×10^8) V/m in the proposed tumor subjected to an array (2×2) NAs for the distances (100, 200, 300, and 400) nm respectively, as shown in Figure 3.26 (a, b, c, and d).

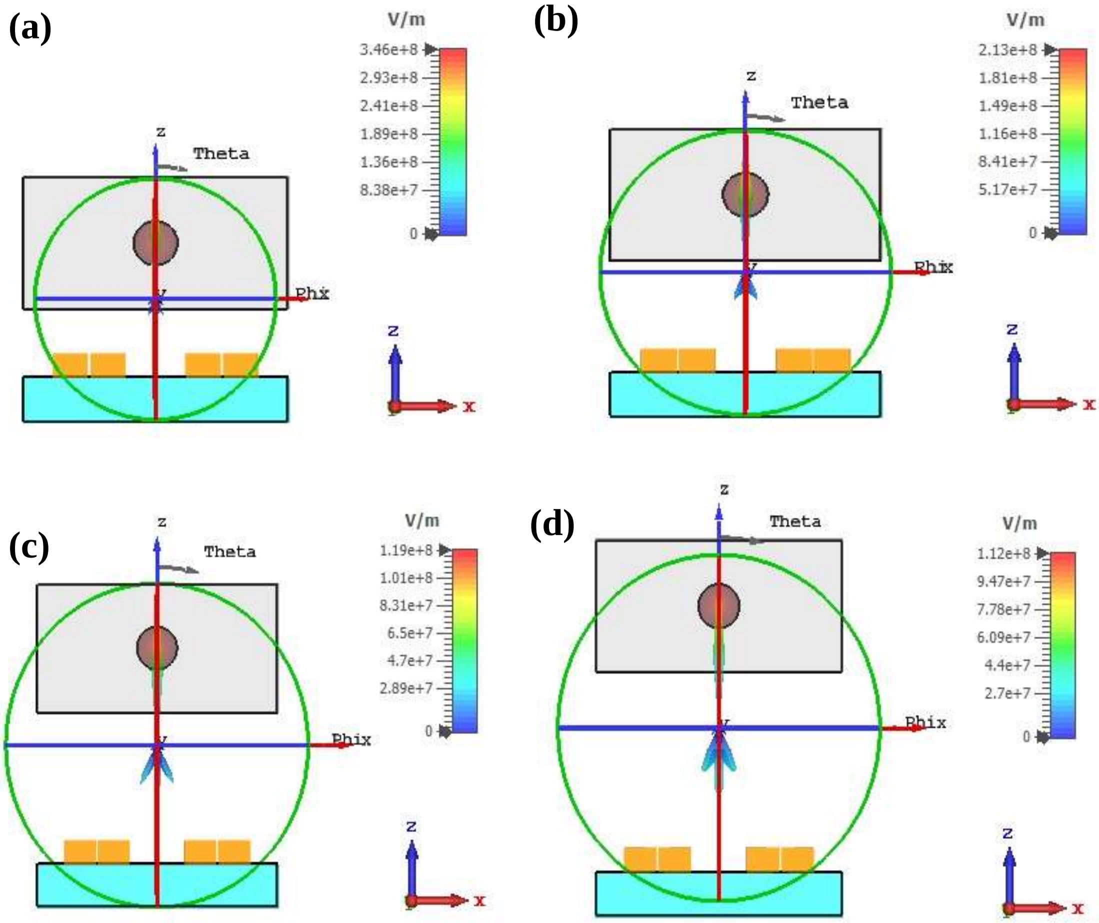

Fig. 3.26 Side view of the far-field pattern for (2×2) an array NAs in the proposed tissue at different distances. (a) 100 nm, (b) 200 nm, (c) 300 nm and (d) 400 nm.

It is observed that the field is enhanced in the tissue which could be interpreted as the collection effect of NAs in an array structures.

An array (3×3) NAs is located beyond the tumor tissue for the distances (100, 200, 300, and 400) nm respectively as shown in Figure 3.27

(a, b, c, and d). The maximum far-field calculated is (1.3×10^8, 7.83×10^7, 5.92×10^7, and 4.17×10^7) V/m. There is not clear enhancement in comparison to the array of (2×2) NAs.

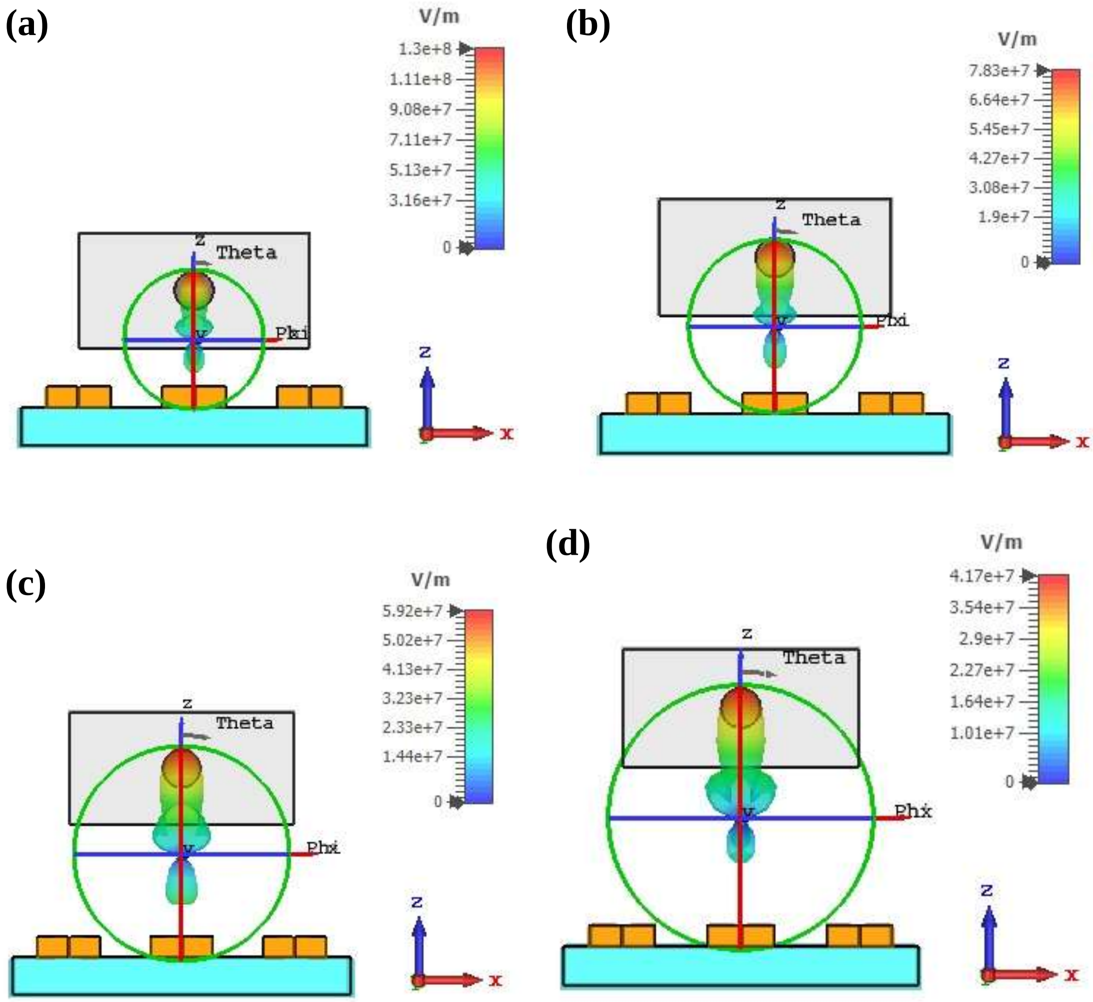

Fig. 3.27 Side view of the far-field pattern for (3×3) an array NAs in the proposed tissue at different distances. (a) 100 nm, (b) 200 nm, (c) 300 nm and (d) 400 nm.

Figure 3.28 (a, b, c and d) illustrates the maximum far-field distributed in the tumor tissue (1.76×10^8, 9.49×10^7, 5.69×10^7, and 4.61×10^7) V/m after exposed to the array NAs (4×4) for the distances (100, 200, 300, and 400) nm respectively.

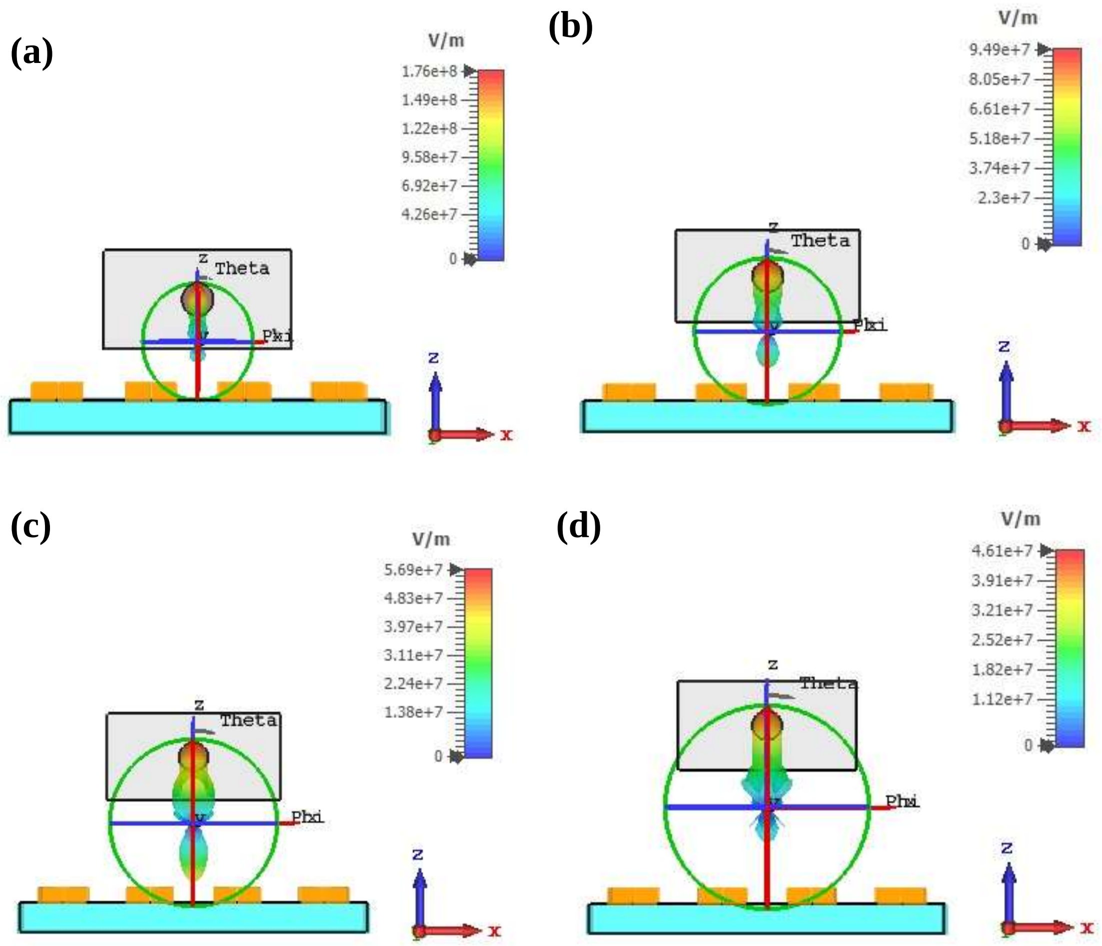

Fig. 3.28 Side view of the far-field pattern for (4×4) an array NAs in the proposed tissue at different distances. (a) 100 nm, (b) 200 nm, (c) 300 nm and (d) 400 nm.

It is noticed that the field is enhanced again in the tissue which improves the effect of number of arrays on the field intensity. As a result, it is shown clearly that the field in an array structures does not depend on the number of arrays although the detected field in the array (2×2) is the highest.

3.4.4 An array nano-antenna (2×2, 3×3 and 4×4) at 1064 nm

Figure 3.29 shows the far-field distribution in the tumor for an array of (2×2) NAs. The maximum far-field calculated is (1.7×10^{8}, 7.5×10^{7}, 4.53×10^{7}, and 3.49×10^{7}) V/m for the distances (100, 200, 300, and 400) nm respectively. It is observed the reduction in the field little bit in comparison to that detected in the normal case of NAs.

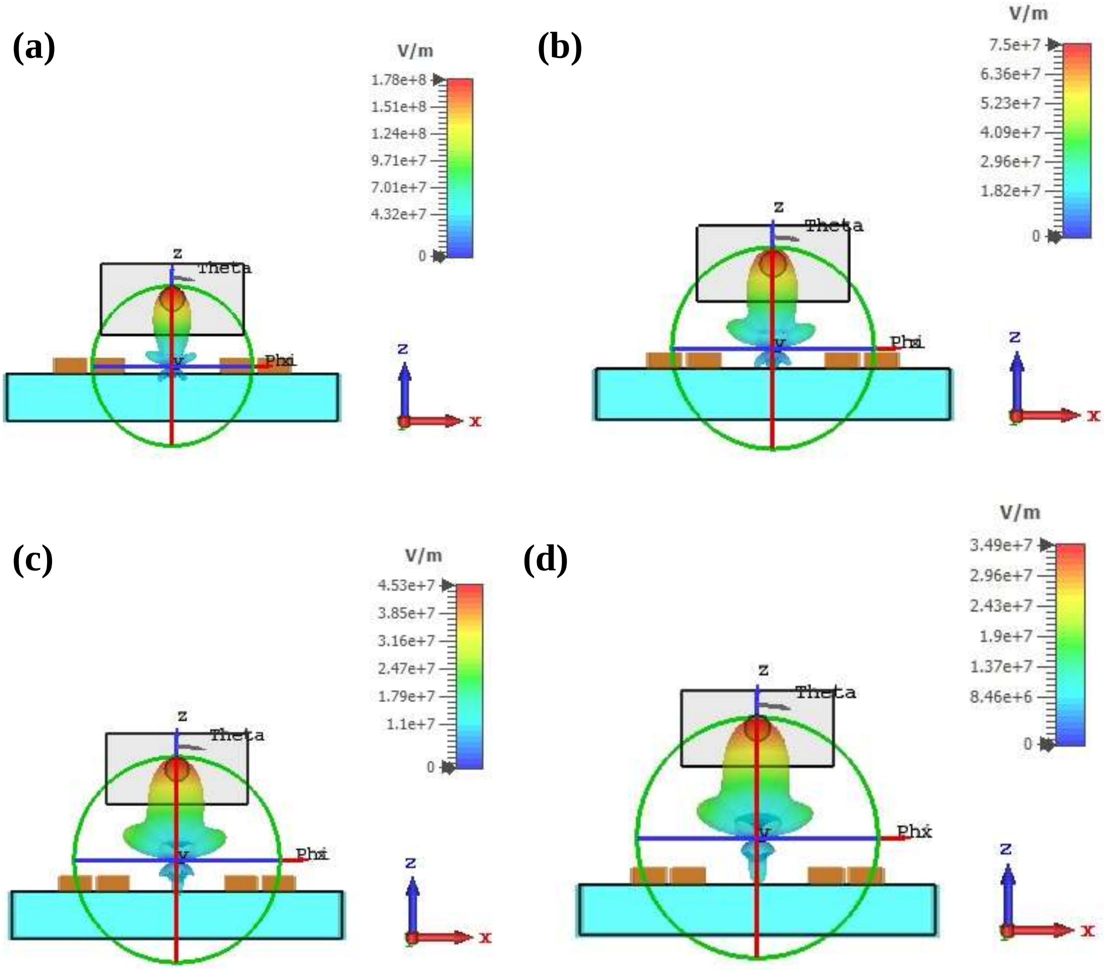

Fig. 3.29 Side view of the far-field pattern for (2×2) an array NAs in the proposed tissue at different distances. (a) 100 nm, (b) 200 nm, (c) 300 nm and (d) 400 nm.

The field distribution in the tumor tissue irradiated by an array NAs (3×3) for the distances (100, 200, 300, and 400) nm respectively is shown in Figure 3.30 (a, b, c, and d). The maximum far-field calculated is (1.5×10^{8}, 7.84×10^{7}, 5.65×10^{7}, and 4.76×10^{7}) V/m. No clear variation is observed in the field intensity but still the closest one is the highest value of field (100) nm similar to the previous one.

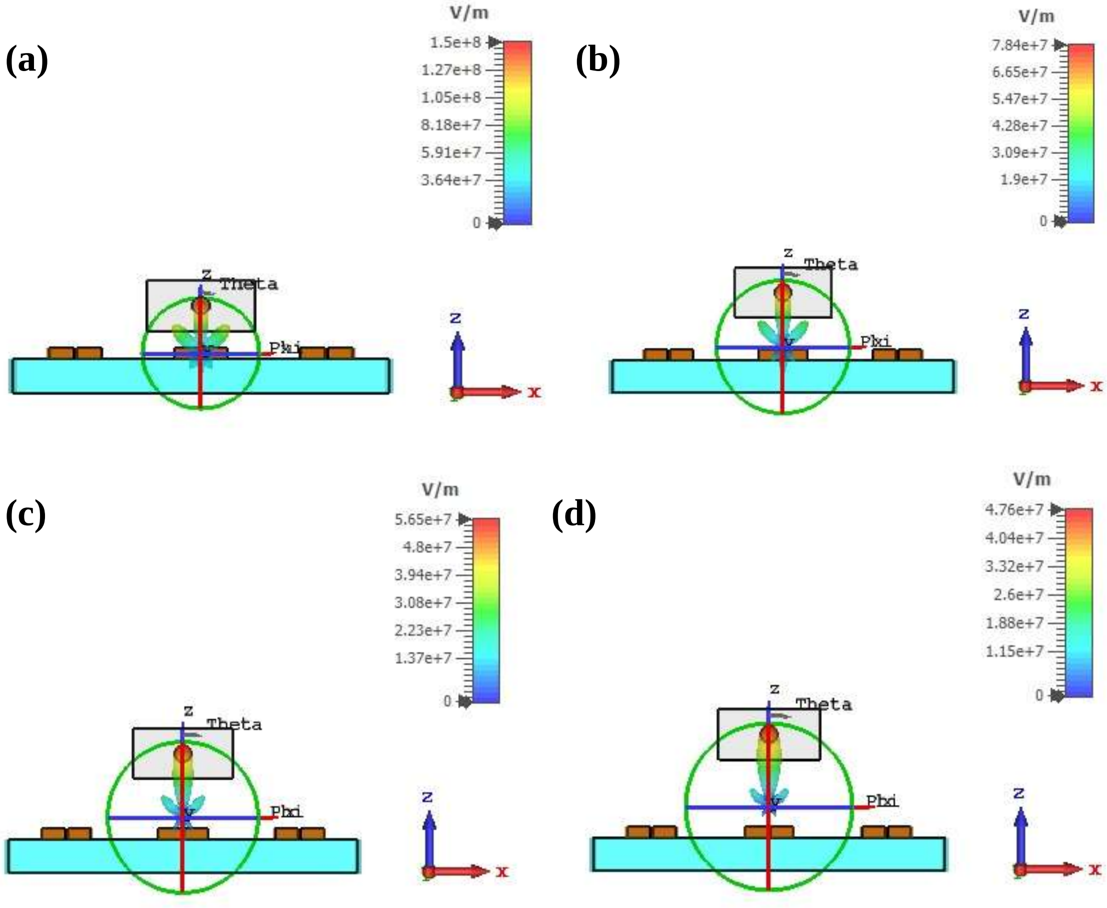

Fig. 3.30 Side view of the far-field pattern for (3×3) an array NAs in the proposed tissue at different distances. (a) 100 nm, (b) 200 nm, (c) 300 nm and (d) 400 nm.

Figure 3.31 (a, b, c and d) illustrates the maximum far-field distributed in the tumor tissue subjected to an array of (4×4) NAs. The intensity field is (1.76×10^8, 9.49×10^7, 5.69×10^7, and 4.61×10^7) V/m for the distances (100, 200, 300, and 400) nm respectively. It is observed a small increment in the field intensity and the highest value is detected at 100 nm.

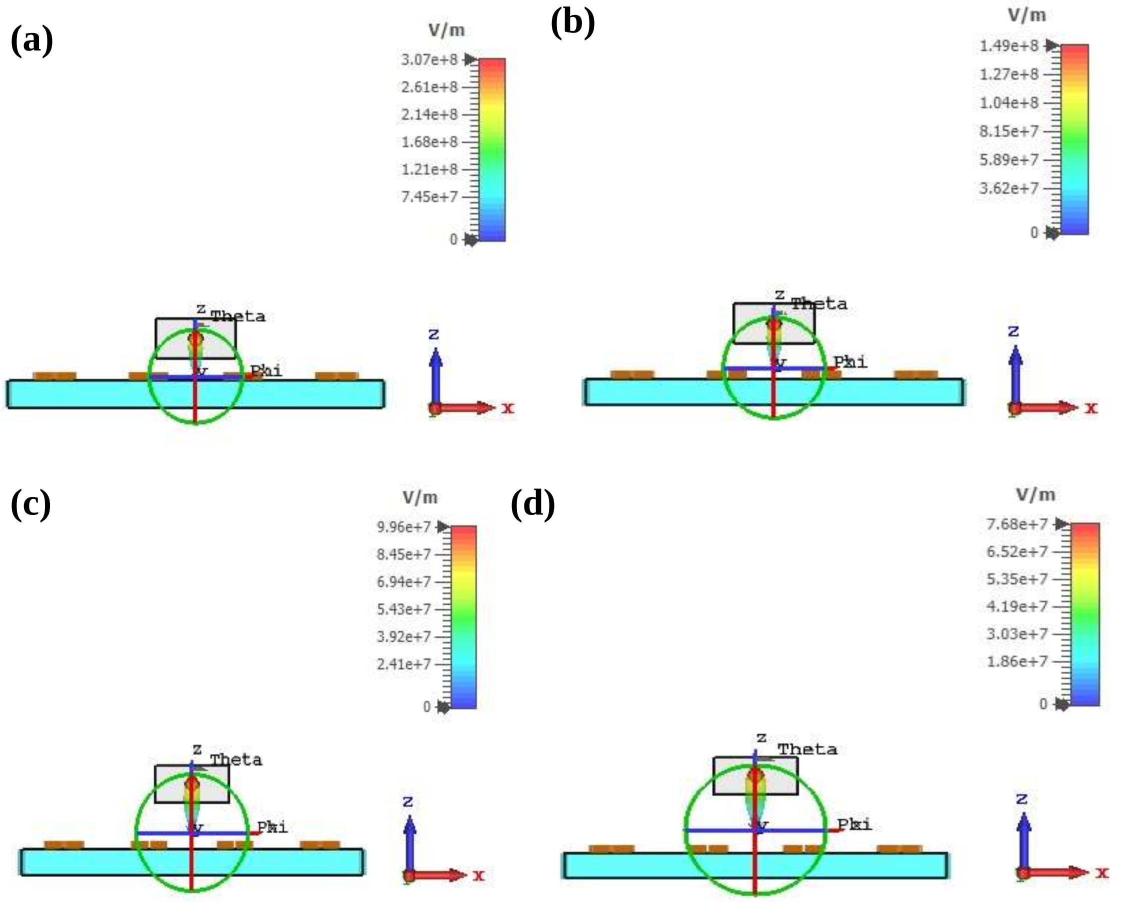

Fig. 3.31 Side view of the far-field pattern for (4×4) an array NAs in the proposed tissue at different distances. (a) 100 nm, (b) 200 nm, (c) 300 nm and (d) 400 nm.

3.4.5 Half wavelength array nano-antenna (2×2, 3×3 and 4×4) at 532 nm

The next step is to investigate the effect of the field pattern interaction with the proposed tumor tissue as indicated in the Figures 3.32, 3.33, 3.34.

From the optimal design for (2×2) an array NA at (100, 200, 300, and 400) nm distances as shown in Figure 3.32, it seems that the field was sharp and varied in the case of (2×2) an array NA. The field decreased as the distance increased it is about (1.28×10^{8}, 5×10^{7}, 3.08×10^{7} and 2.53×10^{7}) V/m for distance 100, 200, 300, and 400 nm respectively.

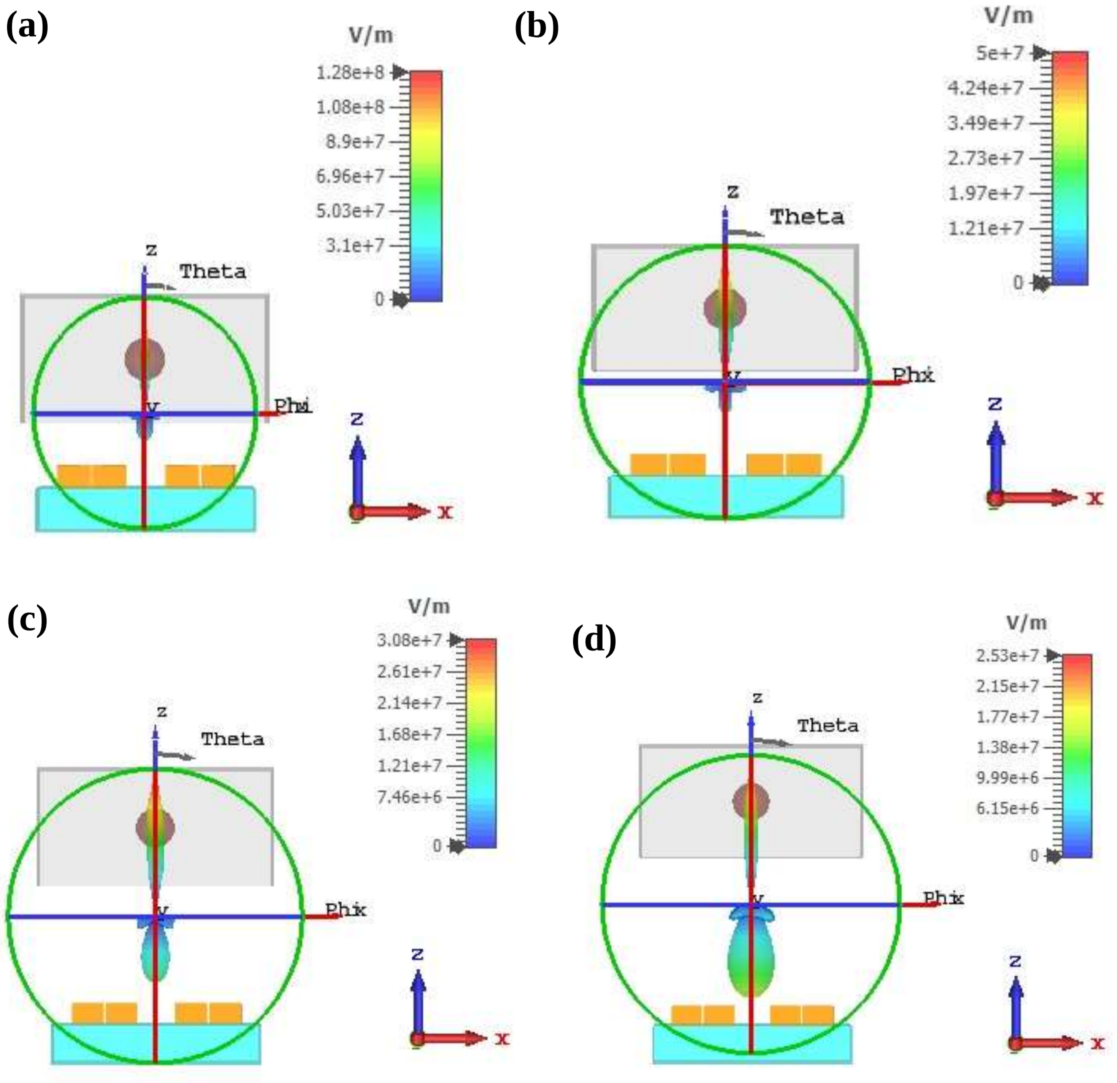

Fig. 3.32 Side view of the far-field pattern for (2×2) half wavelength array NAs in the proposed tissue at different distances. (a) 100 nm, (b) 200 nm, (c) 300 nm and (d) 400 nm.

The effect of field from (3×3) half wavelength array NAs on the tumor of the tissue is also investigated and the results are depicted in Fig. 3.33 for different distances (100, 200, 300 and 400) nm. The field distribution is varied in the tumor and decreased as the distance increased, it is about (1.3×10^{8}, 8.19×10^{7}, 5.78×10^{7} and 3.49×10^{7}) V/m.

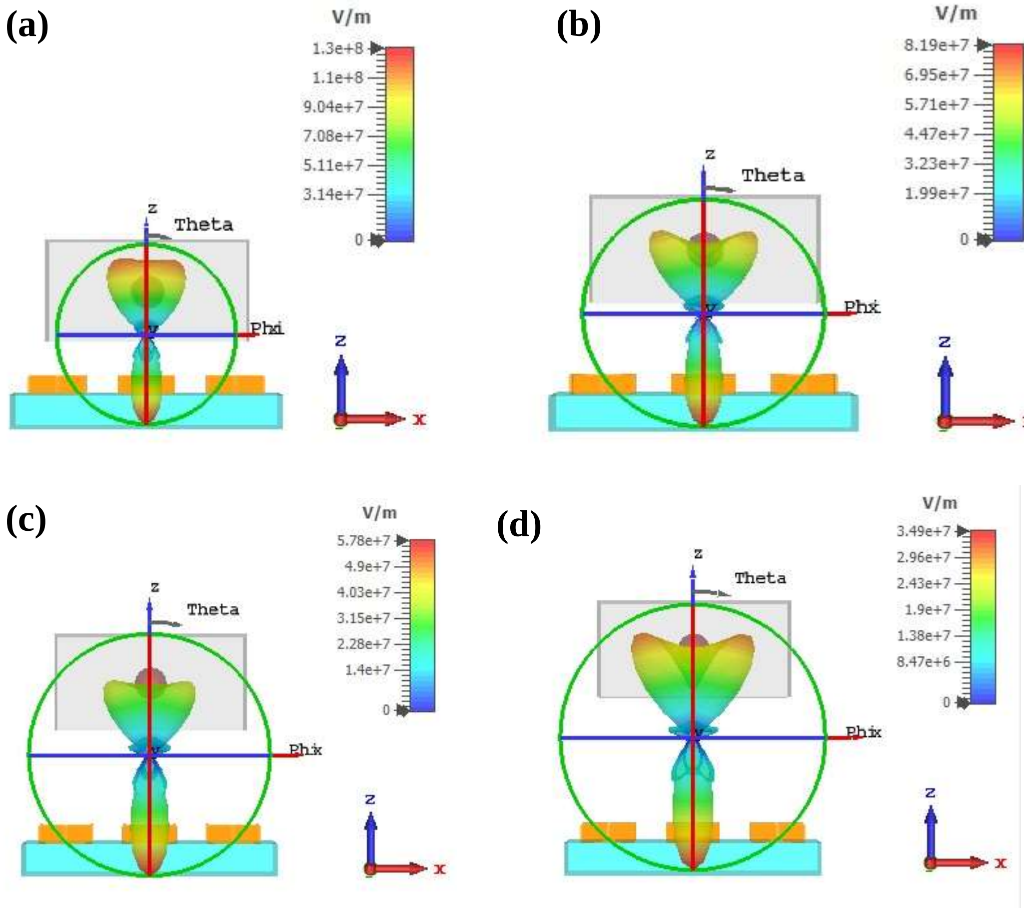

Fig. 3.33 Side view of the far-field pattern for (3×3) half wavelength array NAs in the proposed tissue at different distances. (a) 100 nm, (b) 200 nm, (c) 300 nm and (d) 400 nm.

Figure 3.34 shows the field interaction in the proposed tumor corresponding to the (4×4) half wavelength array NAs. The pattern of the field is observed in the tumor (1.63×10^{8}, 9.5×10^{7}, 7.16×10^{7} and 4.64×10^{7}) V/m for the distances (100, 200, 300 and 400) nm respectively.

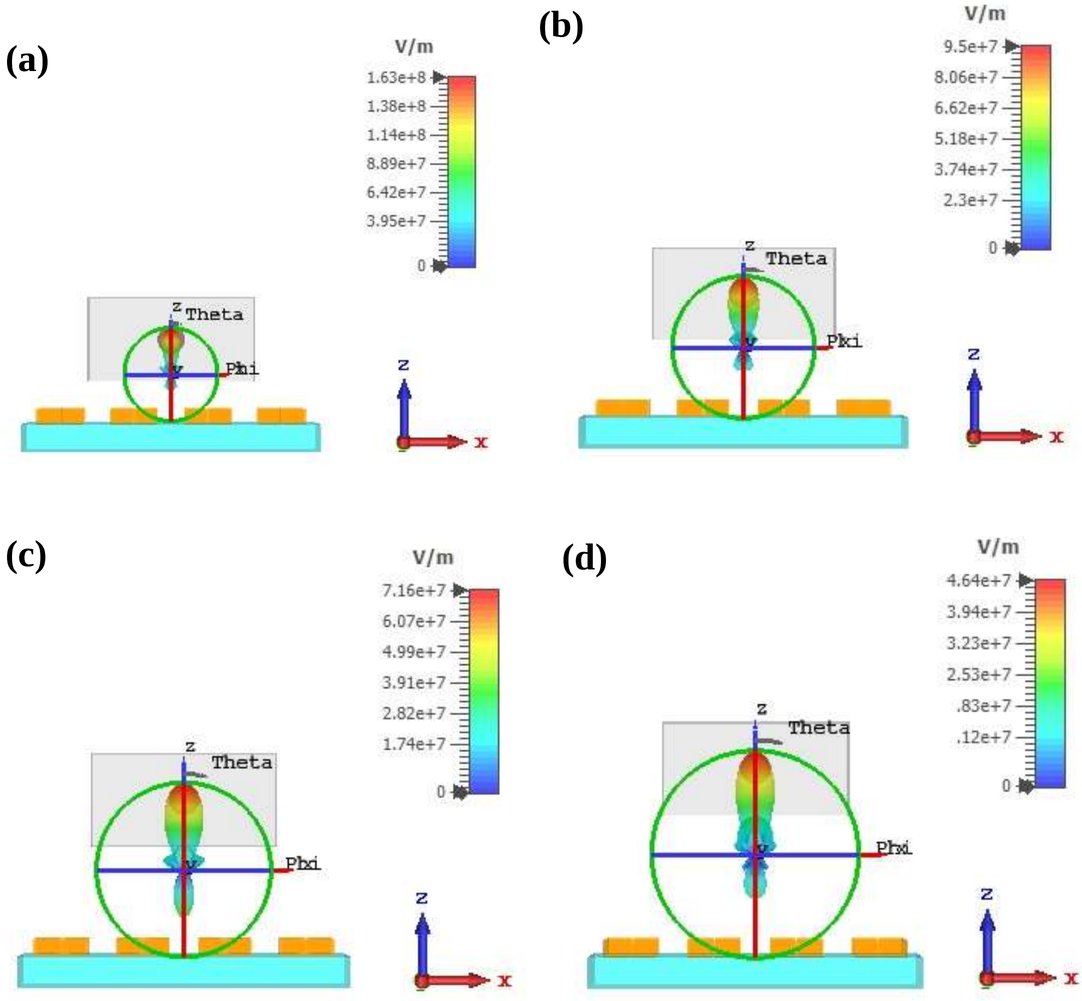

Fig. 3.34 Side view of the far-field pattern for (4×4) half wavelength array NAs in the proposed tissue at different distances. (a) 100 nm, (b) 200 nm, (c) 300 nm and (d) 400 nm.

In the three cases of the half wavelength array NAs (2×2, 3×3 and 4×4) at 532 nm, the results highlight the linear variation of the field with distance, the field decreased as the distance from the tumor increase but the pattern is different and varied for each case according to the number of the array. It observed also that higher arrays produce higher field in the tissue.

3.4.6 Half wavelength array nano-antenna (2×2, 3×3 and 4×4) at 1064 nm

To further demonstrate the interaction of the field with the proposed tumor in the half wavelength array NAs (2×2, 3×3 and 4×4) at 1064 nm as shown in Figures 3.35, 3.36, and 3.37.

Figure 3.35 shows the effect of an array NAs (2×2) on the field produced in the tumor at distances (100, 200, 300 and 400) nm where the maximum detected fields are (1.3×10^8, 6.9×10^7, 4.85×10^7 and 3.6×10^7) V/m respectively. It seems clearly that the field decreases as the higher distances. Also, no big difference is observed between 300 and 400 nm.

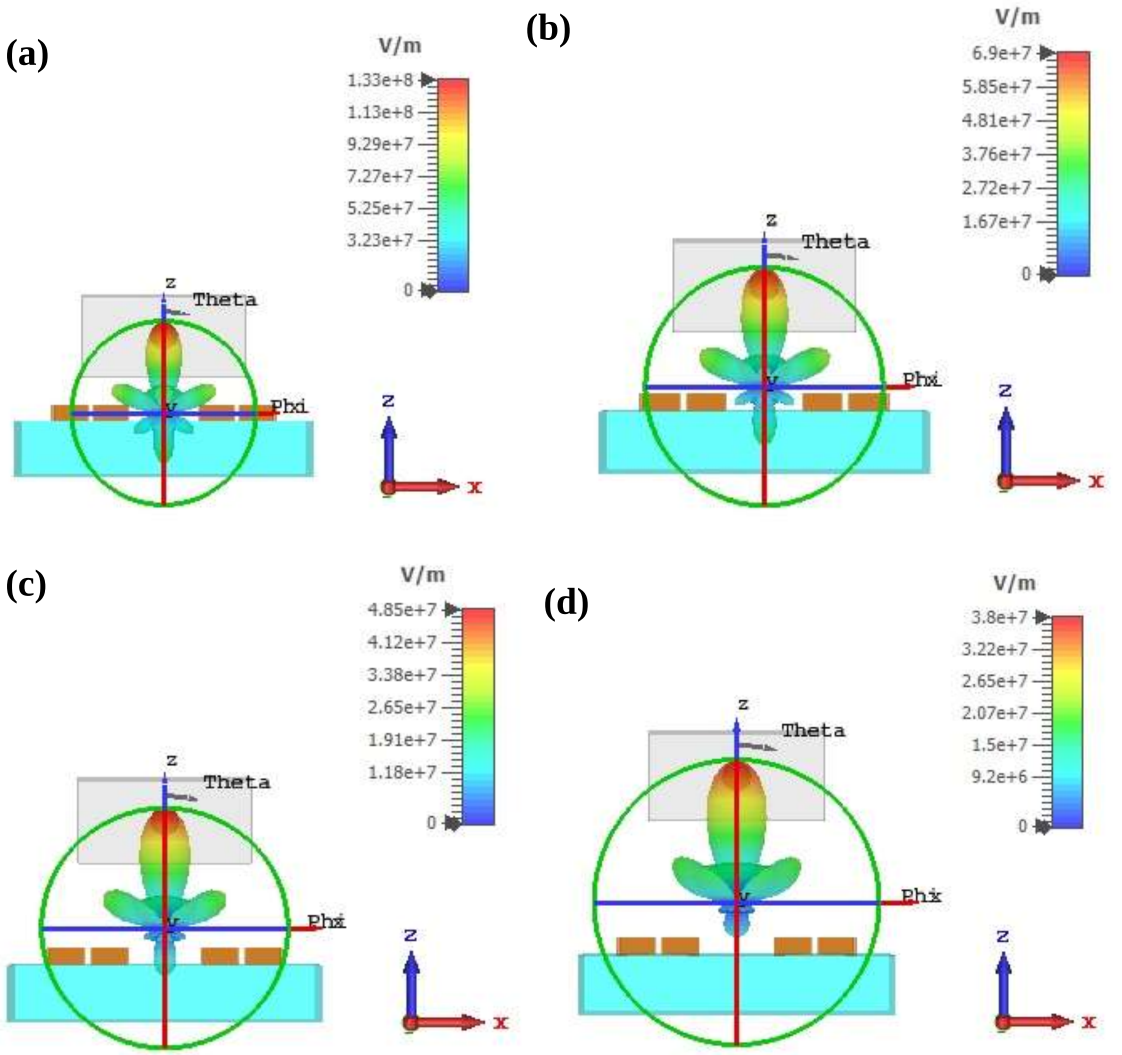

Fig. 3.35 Side view of the far-field pattern for (2×2) half wavelength array NAs in the proposed tissue at different distances. (a) 100 nm, (b) 200 nm, (c) 300 nm and (d) 400 nm.

In order to understand the optical behavior of the proposed tumor, it is useful to display the electrical field distributions of an array NA (3×3 and 4×4) at half wavelength as shown in Figures 3.36 and 3.37.

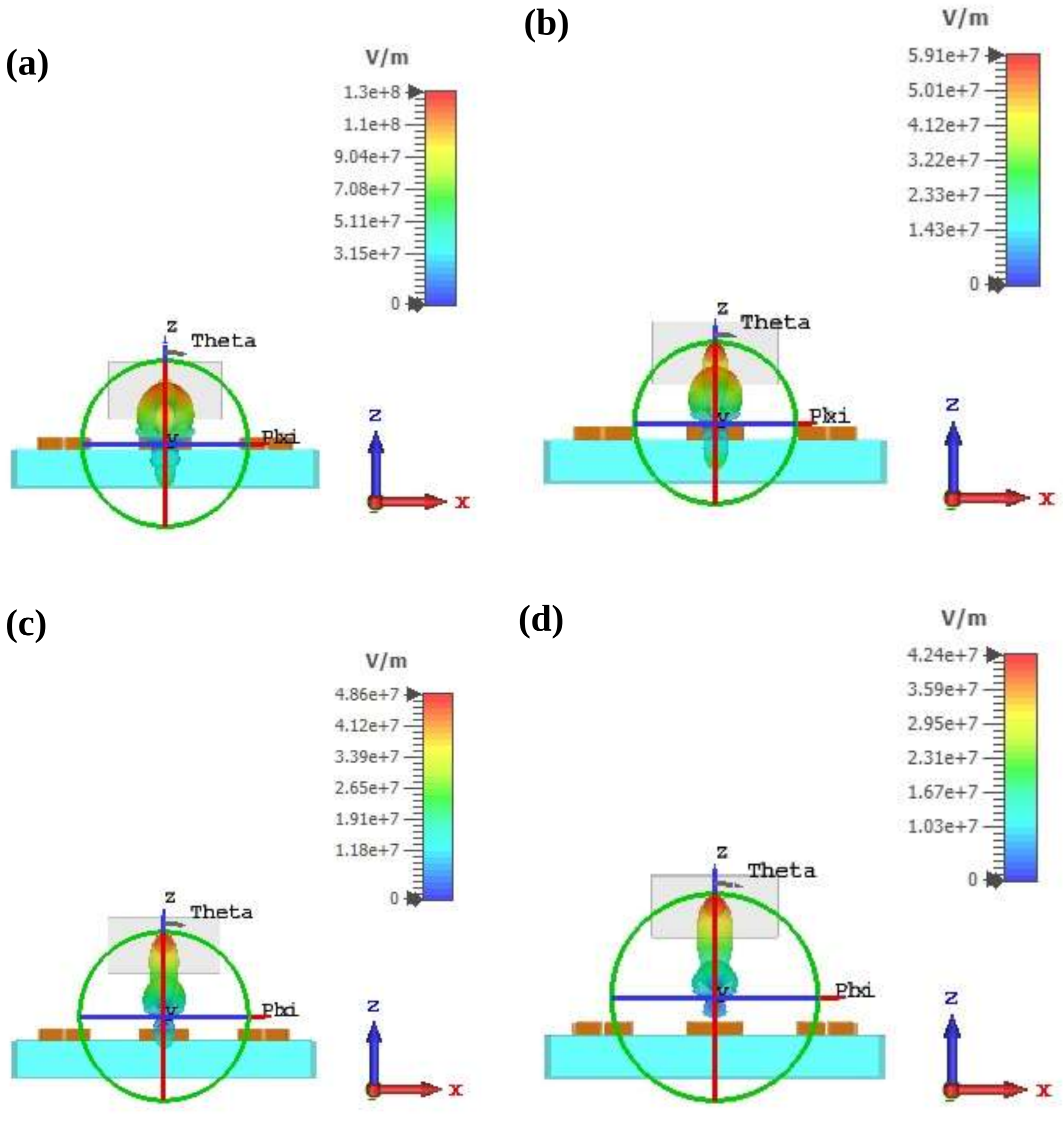

Fig. 3.36 Side view of the far-field pattern for (3×3) half wavelength array NAs in the proposed tissue at different distances. (a) 100 nm, (b) 200 nm, (c) 300 nm and (d) 400 nm.

The maximum detected fields are (1.3×10^8, 5.9×10^7, 4.86×10^7 and 4.24×10^7) V/m for the distances (100, 200, 300 and 400) nm which indicates that no effective difference in comparison to the array (2×2) is appeared, may be due to the distribution of the field is not concentrated in the center.

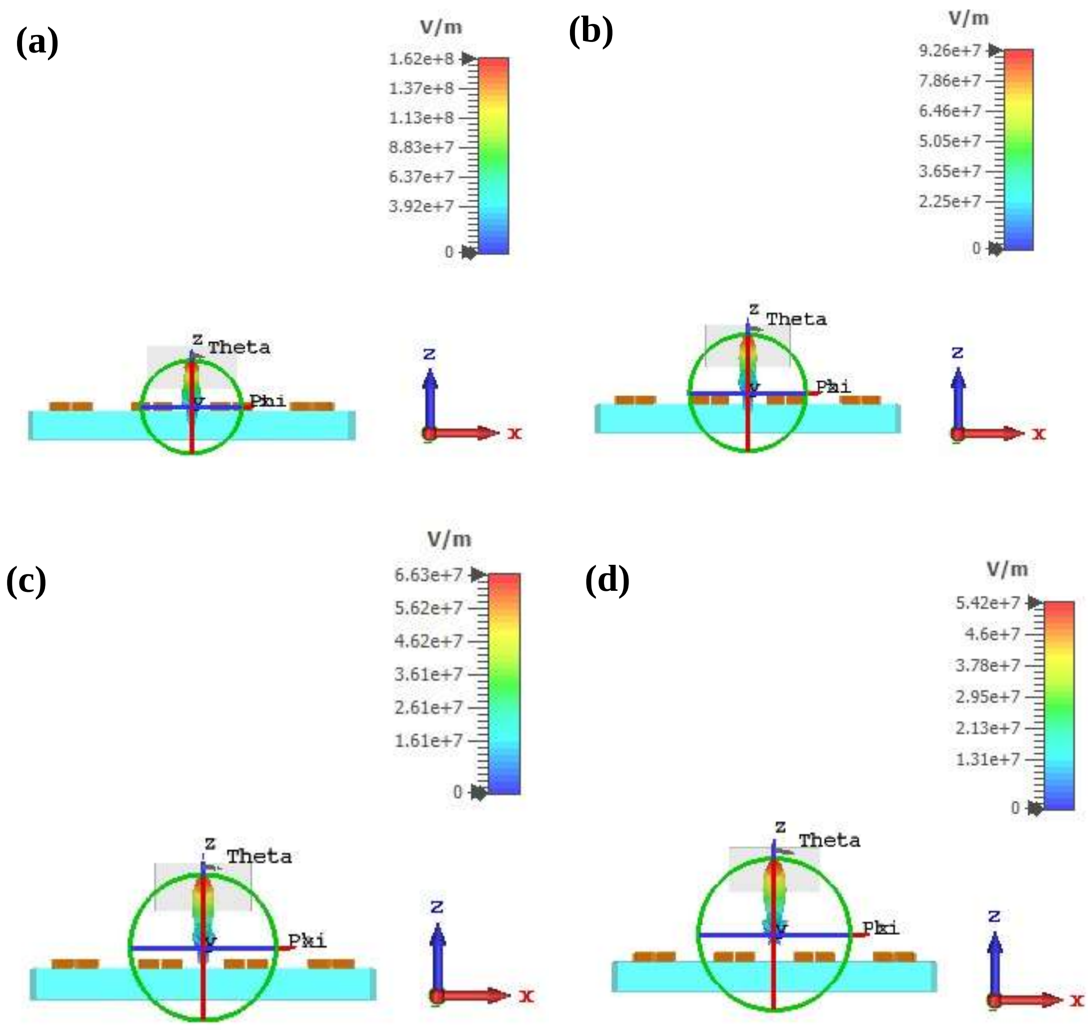

Fig. 3.37 Side view of the far-field pattern for (4×4) half wavelength array NAs in the proposed tissue at different distances. (a) 100 nm, (b) 200 nm, (c) 300 nm and (d) 400 nm.

Now, the far-field of the array (4×4) are (1.62×10^8, 9.26×10^7, 6.6×10^7 and 5.42×10^7) V/m for distances (100, 200, 300 and 400) nm respectively. The increment in the field is limited which shows the small effect of an array (4×4) in comparison to other arrays.

The pattern of the field was different and varied with distance and this dependent on the number of an array NA used with the proposed tissue, but it is well observed that the variations between the number of arrays are quite limited. This may be attributed to the absorption of the light field is different from that detected at the resonance wavelength 532.

3.5 Specific absorption rate calculations

The estimation of the temperature distribution of any tumor embedded in a tissue exposed to a light source is quite complicated due to the nature and the location of tissues. In the present study, the time of reaching the temperature to be fair enough for destroying the diseased cells is estimated through the calculation of SAR.

3.5.1 Specific absorption rate at 532 nm for single nano-antenna

The optimized single NA working at resonance wavelength 532 nm is located at different distances from the tissue (100, 200, 300 and 400) nm to calculate the SAR for each as illustrated in Figure 3.38 (a, b, c, and d). The point SAR inside the proposed tissue are (1.83×10^{11}, 1.19×10^{11}, 8.22×10^{10} and 4.72×10^{10}) W/kg for distances (100, 200, 300 and 400) nm respectively. It is observed clearly that the SAR reduces with increases the distance because the reduction of the strength of the receiving far-field. The field is concentrated in the center of the tumor which means that the surrounding tissues are not affected by the field.

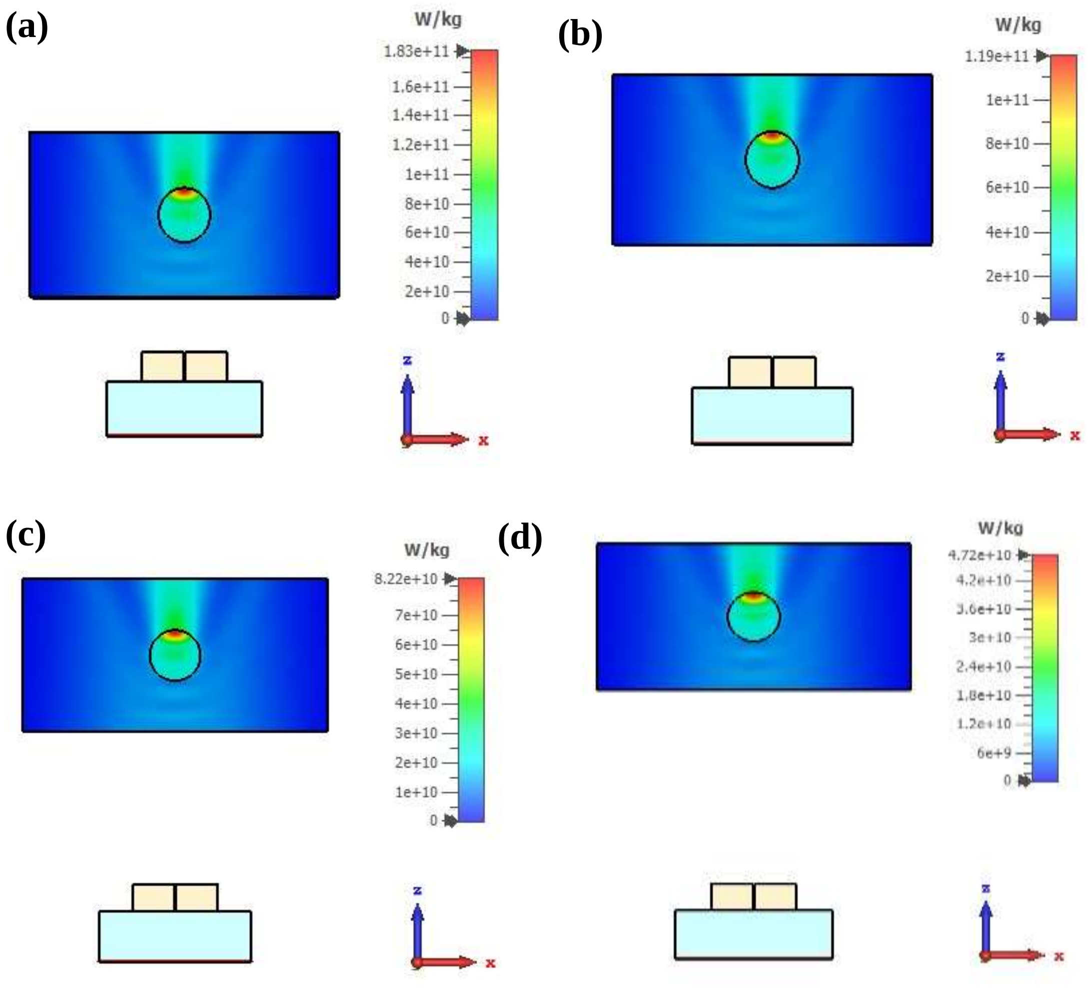

Fig. 3.38 The calculated SAR in the proposed tumor tissue exposed to a single NA at 532 nm for different distances. (a) 100 nm, (b) 200 nm, (c) 300 nm and (d) 400 nm.

The behavior of SAR related to the distance from the proposed tissue at the wavelength of 532 nm for single NAs is shown in Figure 3.39. The SAR is increased with closer distance and the maximum value of SAR is detected for single unit.

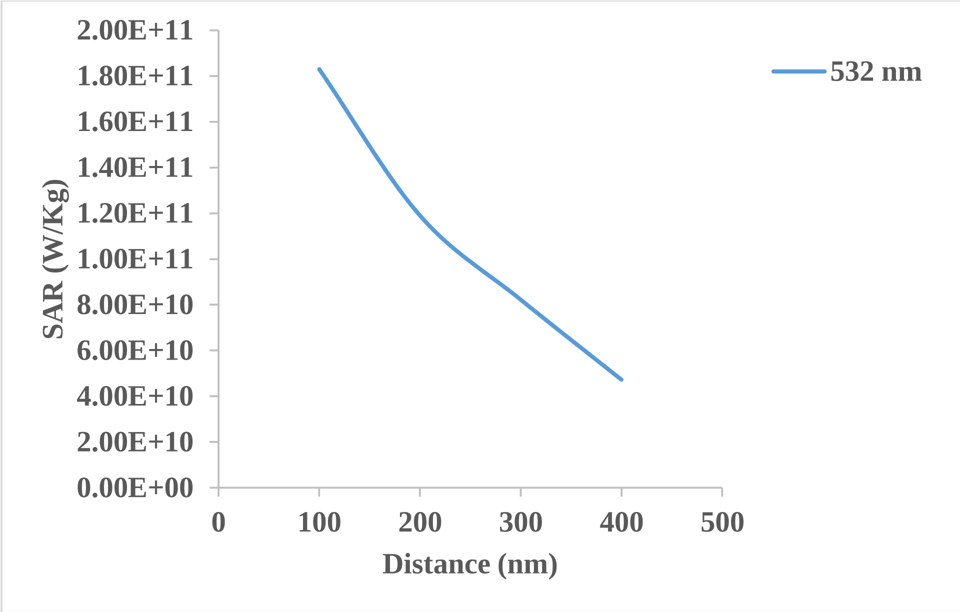

Fig 3.39 Specific absorption rate as a function of the distance from the tissue at single unit for 532 nm.

3.5.2 Specific absorption rate calculations at 1064 nm single nano-antenna

Figure 3.40 (a, b, c and d) shows the distribution of the field in the tissue after subjecting to single NA at 1064 nm for various distances (100, 200, 300 and 400) nm. The point SAR inside the proposed tissue could be calculated. The maximum values of SAR are (2.28×10^{11}, 1.17×10^{11}, 8.49×10^{10} and 8.11×10^{10}) W/kg for distances (100, 200, 300, and 400) nm respectively. It is noticed that the point SAR value is not varied clearly at this wavelength.

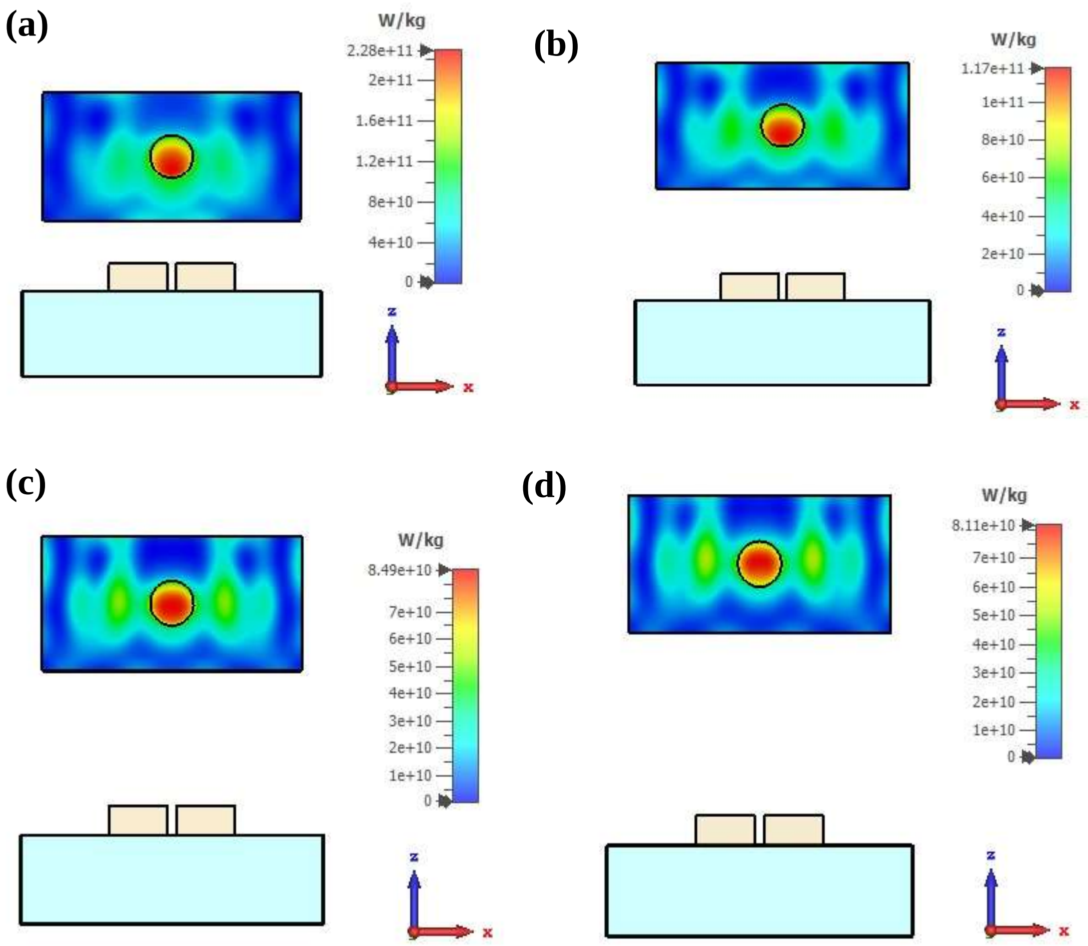

Fig. 3.40 The calculated SAR in the proposed tumor tissue subjected to single NA at 1064 nm at different distances (a) 100 nm, (b) 200 nm, (c) 300 nm and (d) 400 nm.

Figure 3.41 shows the behavior of SAR as a function of different distances at the wavelength of 1064 for single NAs. Similar behavior is detected for both wavelengths but it is noticed that sharp reduction from single to an array structures.

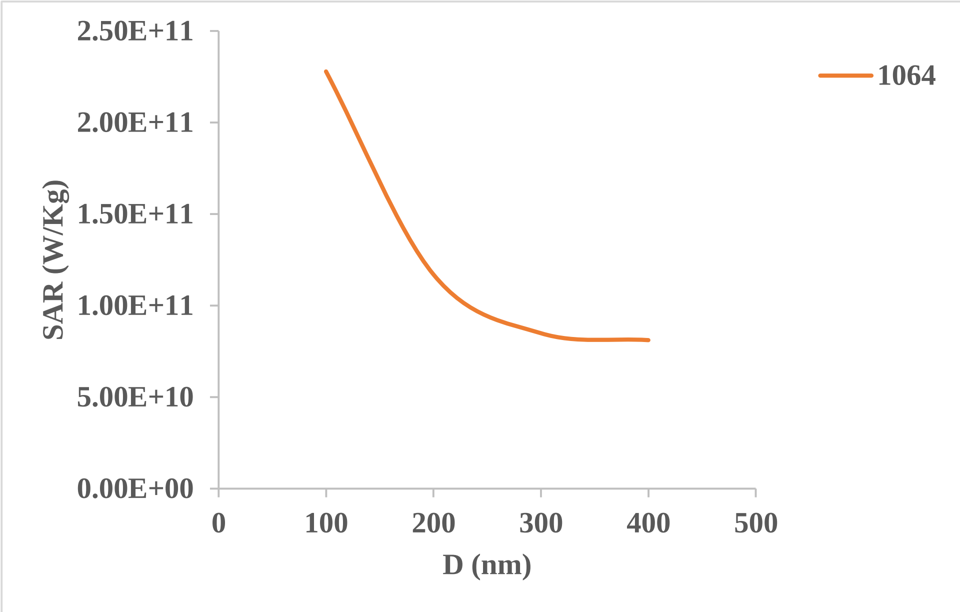

Fig 3.41 The specific absorption rate as a function of the distance from the proposed tissue at 1064 nm for single unit.

It is obvious that the distribution of the far-field in the tumor is varied for two resonance wavelengths (532 and1064) nm where the field is appeared out the tumor in the case of 1064 nm. This distribution may affect on the healthy surrounding tissues which are not preferred in this type of application although the strength of the field is suitable. In addition, it is well observed that the SAR increases with the closest distance.

3.5.3 Specific Absorption Rate calculations for (2×2, 3×3 and 4×4) an array nano-antennas at 532 nm

The point SAR inside the proposed tissue could be calculated for (2×2) an array NAs where the maximum values of SAR are (8.44×10^{11}, 8.27×10^{11}, 7.55×10^{11} and 4.19×10^{11}) W/kg for distances (100, 200, 300, and 400) nm respectively, as shown in Figure 3.42 (a, b, c, and c).

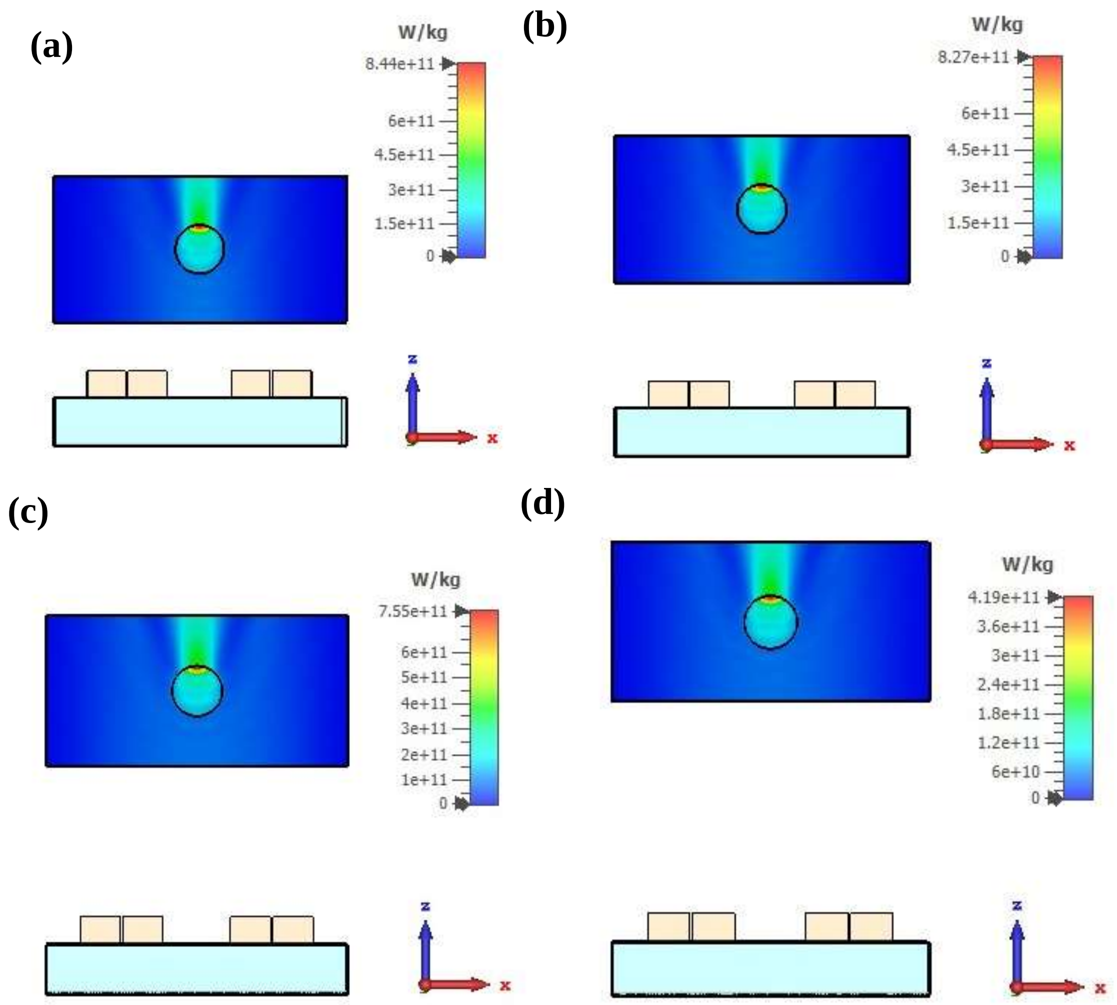

Fig. 3.42 The calculated SAR in the proposed tumor tissue subjected to (2×2) an array NAs at different distances (a) 100 nm, (b) 200 nm, (c) 300 nm and (d) 400 nm.

The point SAR value seems large than that calculated for single one. The distribution of the field is accepted.

If the array of (3×3) NAs is investigated, the field distribution is not concentrated on the tumor in spite of the increment in the SAR due to the large area of the array structure as shown in Figure 3.43. The maximum values of SAR are (5.13×10^{11},4.11×10^{11}, 3.93×10^{11} and 3.39×10^{11}) W/kg for distances (100, 200, 300, and 400) nm respectively.

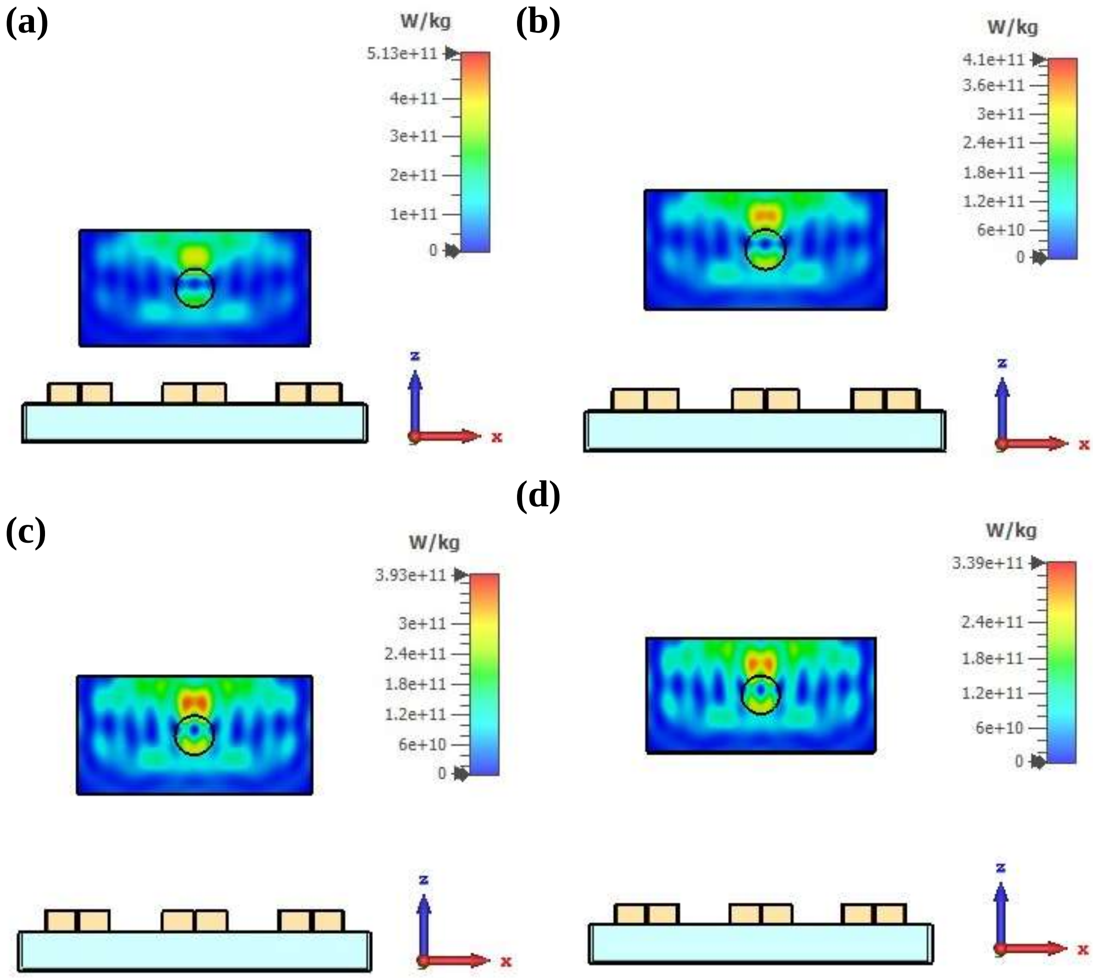

Fig. 3.43 The calculated SAR in the proposed tumor tissue subjected to (3×3) an array NAs for different distances (a) 100 nm, (b) 200 nm, (c) 300 nm and (d) 400 nm.

Figure 3.44 shows the distribution of the field in the tissue that exposed to an array of (4×4) NAs at different distances. The maximum values of the SAR are (8.15×10^{11}, 6.25×10^{11}, 5.15×10^{11} and 4.67×10^{11}) W/kg for distances (100, 200, 300, and 400) nm respectively. The field is almost distributed in all area of the tissue which is not desired due to the field effect may be transferred to the healthy tissue. The main reason of the un concentrated field in the tumor is the coming field from number of NAs.

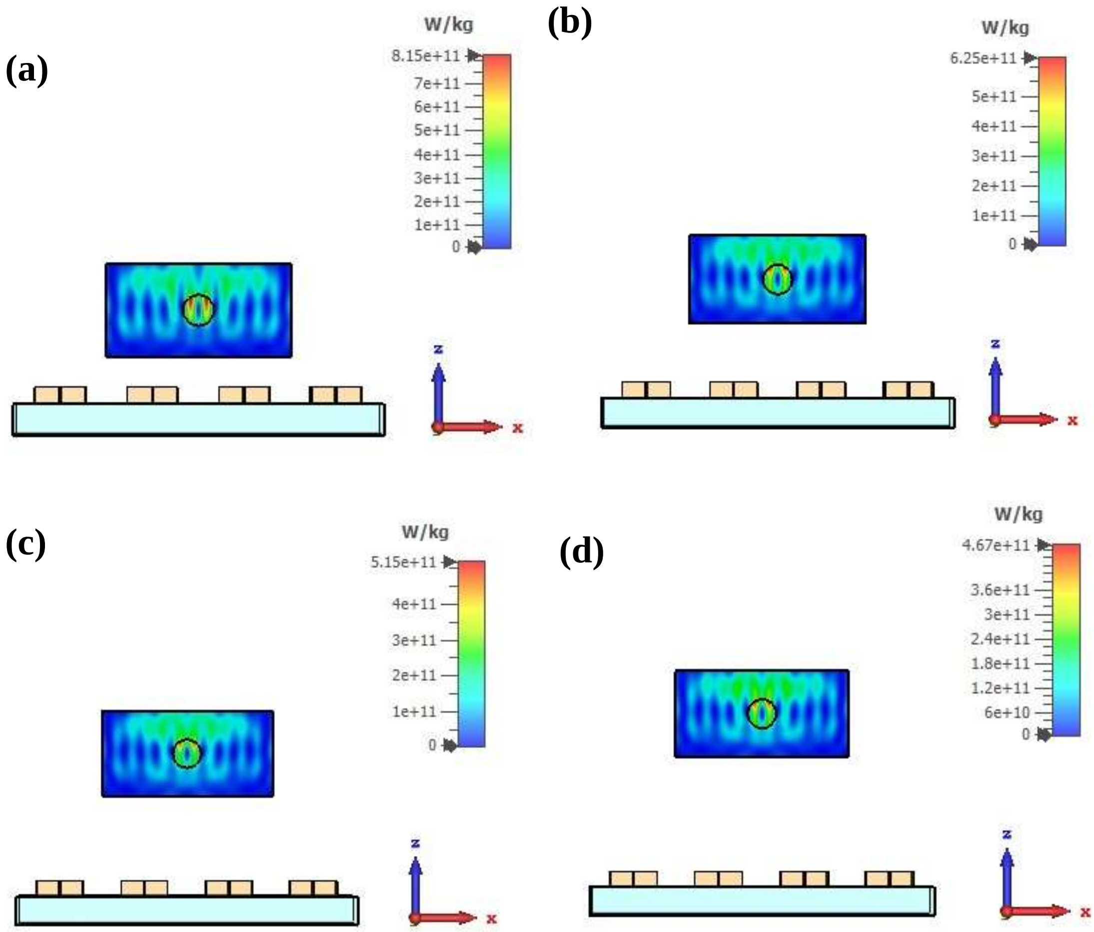

Fig. 3.44 The calculated SAR in the proposed tumor tissue subjected to (4×4) an array NAs for different distances (a) 100 nm, (b) 200 nm, (c) 300 nm and (d) 400 nm.

Figure 3.45 represents the single and three arrays as a function of different distances for 532 nm. It is clear that the distance plays an important role of the distance to increase the SAR. The minimum value is calculated for single unit while the maximum for the array (2×2) NAs.

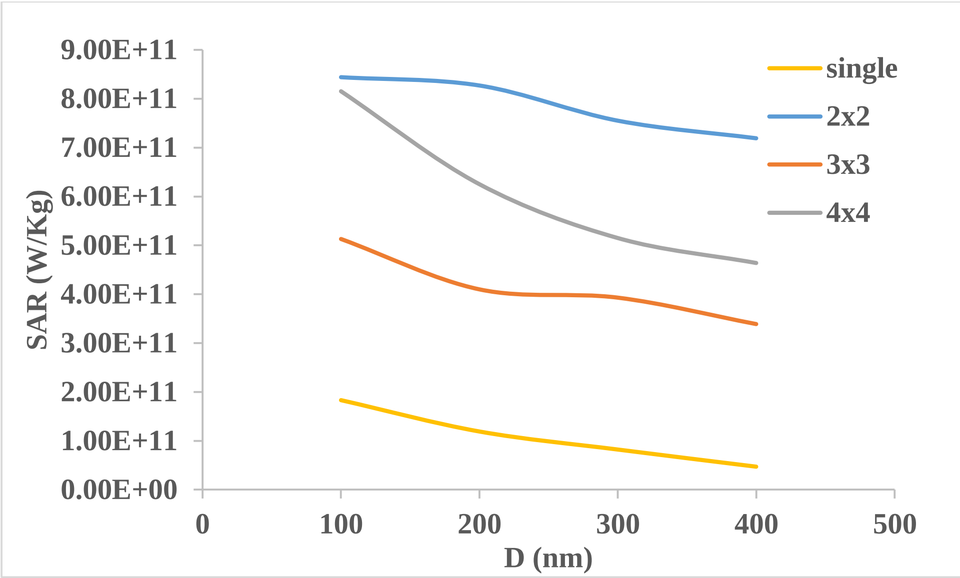

Fig.3.45 The SAR as a function for all design structures at four distances for 532 nm.

3.5.4 Specific absorption rate calculations (2×2, 3×3 and 4×4) an array nano-antennas at 1064 nm

Figure 3.46 (a, b, c, and c) illustrates the SAR inside the proposed tissue irradiated by (2×2) an array NAs. The maximum SAR values are (1.87×10^{11}, 1.16×10^{11}, 8.91×10^{10} and 8.56×10^{10}) W/kg for distances (100, 200, 300, and 400) nm respectively. It is observed that there is a reduction in the field intensity in comparison to the single antenna because of less absorption.

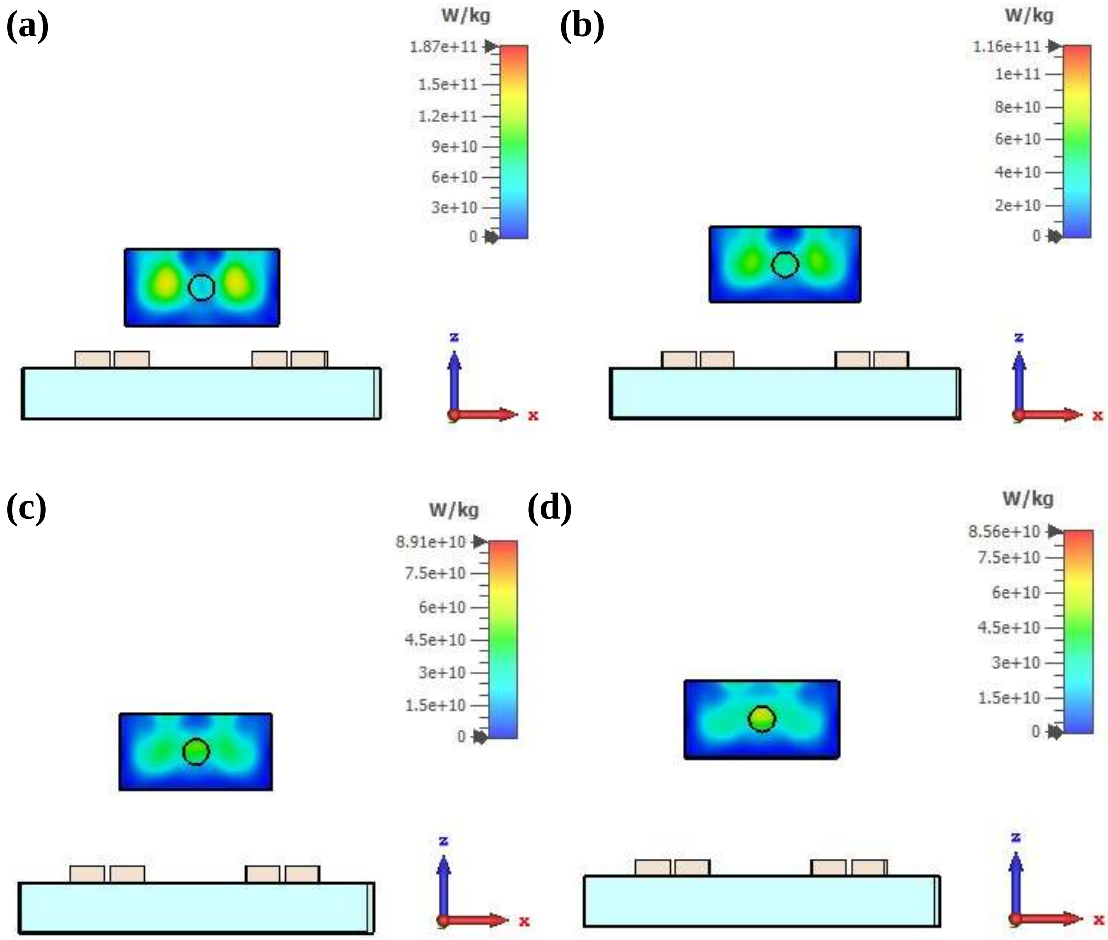

Fig. 3.46 The calculated SAR in the proposed tumor tissue subjected to (2×2) an array NAs at different distances (a) 100 nm, (b) 200 nm, (c) 300 nm and (d) 400 nm.

The distribution of the field is irregular inside the tissue although the received field is high for the shorter distance.

Regarding the array of (3×3) NAs, the distribution field is clearly diffused in all region of the tissue as illustrated in Figure 3.47. The maximum values of SAR are (1.31×10^{11}, 8.2×10^{10}, 7.54×10^{10} and 7.26×10^{10}) W/kg for distances (100, 200, 300, and 400) nm respectively.

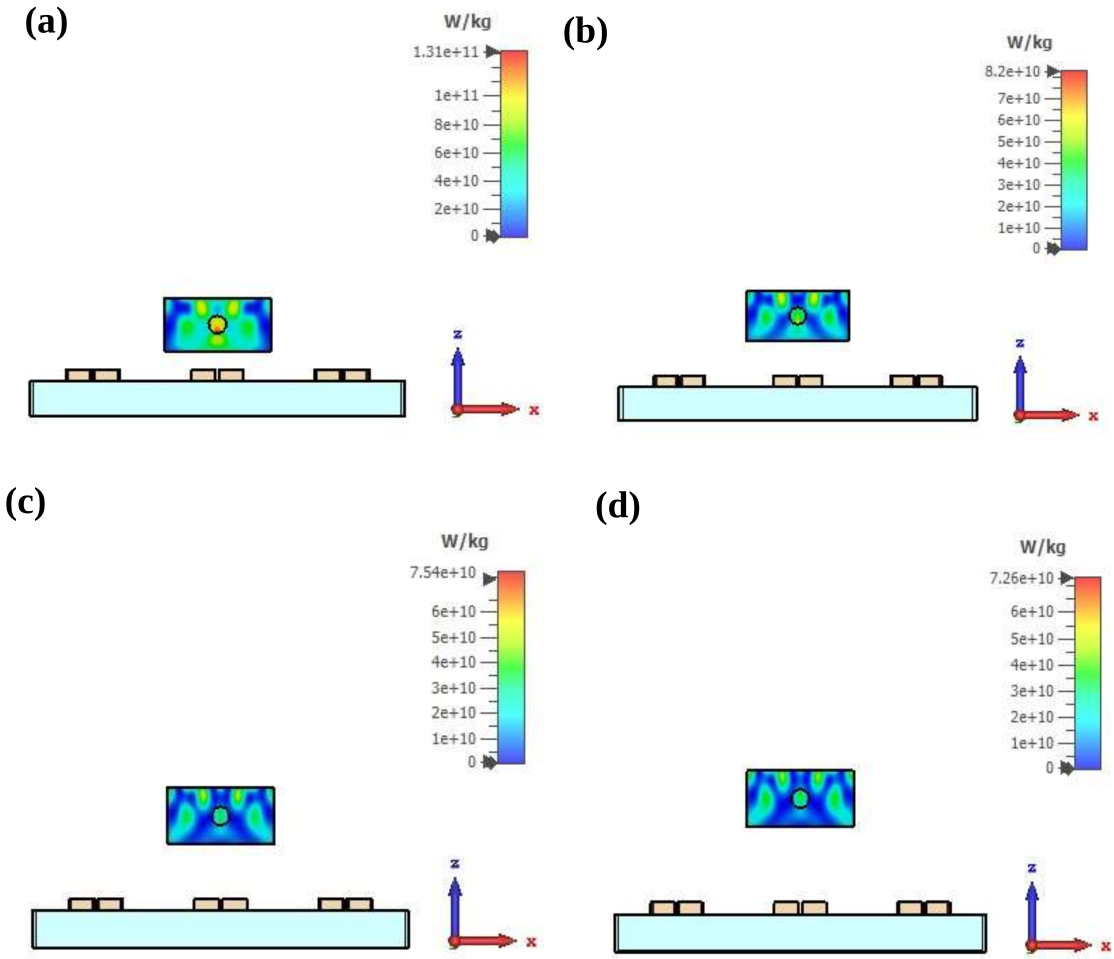

Fig. 3.47 The calculated SAR in the proposed tumor tissue subjected to (3×3) an array NAs at different distances (a) 100 nm, (b) 200 nm, (c) 300 nm and (d) 400 nm.

If the number of arrays is increased to be (4×4), the maximum SAR values of the SAR are (1.16×10^{11}, 5.4×10^{10}, 5.24×10^{10} and 5.16×10^{10}) W/kg for distances (100, 200, 300, and 400) nm respectively, as shown in Figure 3.48 (a, b, c, and c). Here the distribution of the field not clear at all due to the irradiated field is coming from the number of NAs which could not be collimated in the tumor tissue. These type of distribution is not convenient for the treatment of single tumor tissue because of the effect on the un diseased tissue.

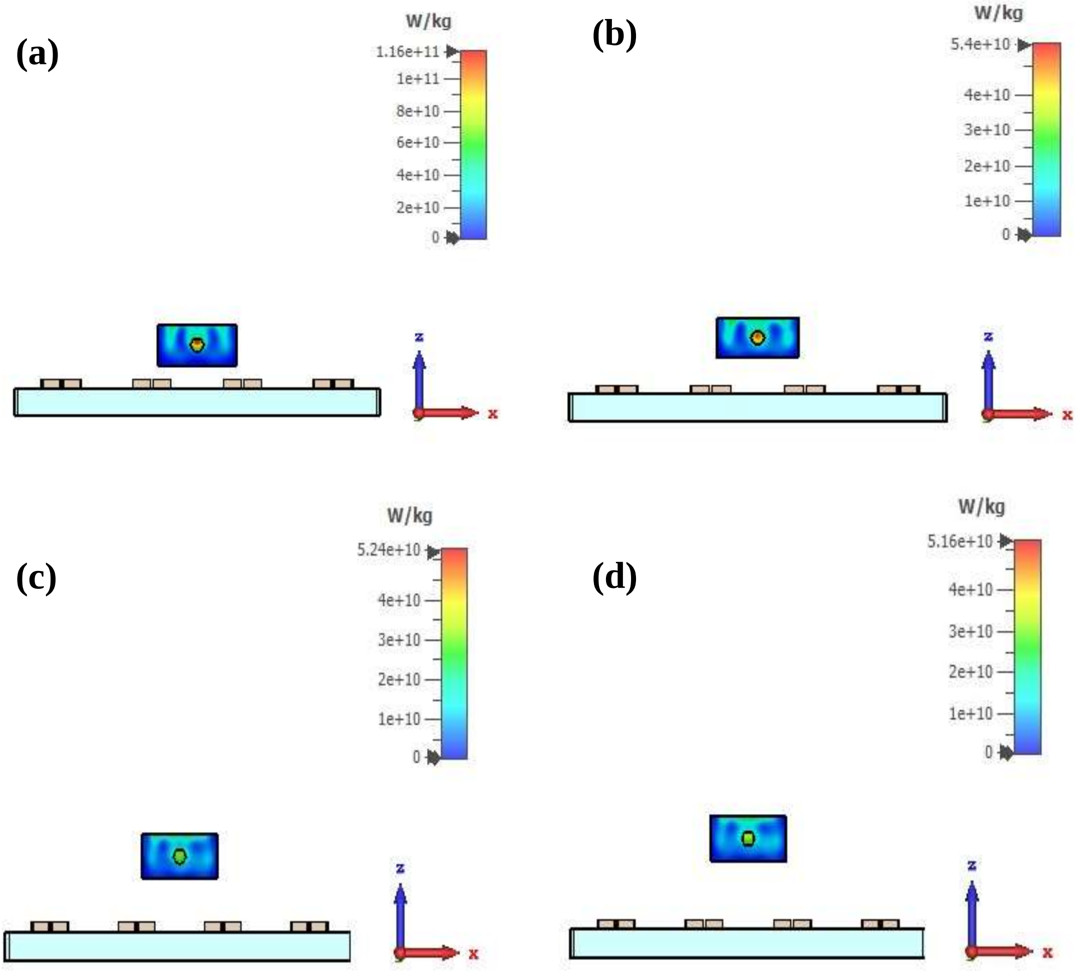

Fig. 3.48 The calculated SAR in the proposed tumor tissue subjected to (4×4) an array NAs at different distances (a) 100 nm, (b) 200 nm, (c) 300 nm and (d) 400 nm.

Similar behavior is observed for the array structures in comparison to the array NAs at the wavelength of 1064 nm with different values but it seems the SAR independent on the number of an array.

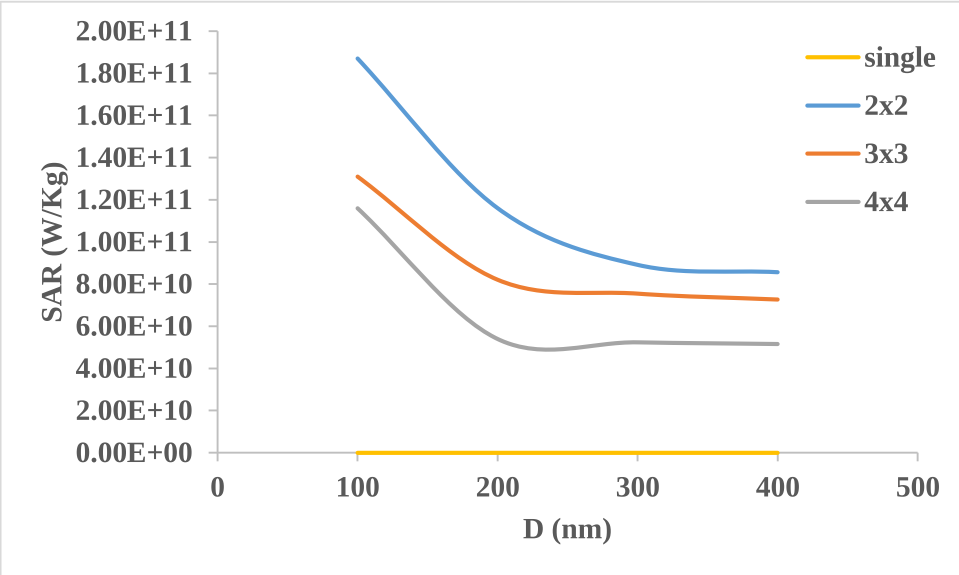

Fig .3.49 The SAR as a function of the distance from the proposed tissue for 1064 nm.

3.5.5 Specific absorption rate calculations for (2×2, 3×3 and 4×4) half wavelength array nano-antennas at 532 nm

Moreover, a variant of the SAR in the proposed tissue using half wavelength array NAs, as shown in Figs. 3.50, 3.51, and 3.52, were studied.

In case of (2×2) half wavelength array NAs the maximum point SAR in the tumor is about (4.18×10^{10}, 2.89×10^{10}, 2.83×10^{10}, and 2.73×10^{10}) W/kg for the distance (100, 200, 300 and 400) nm respectively.

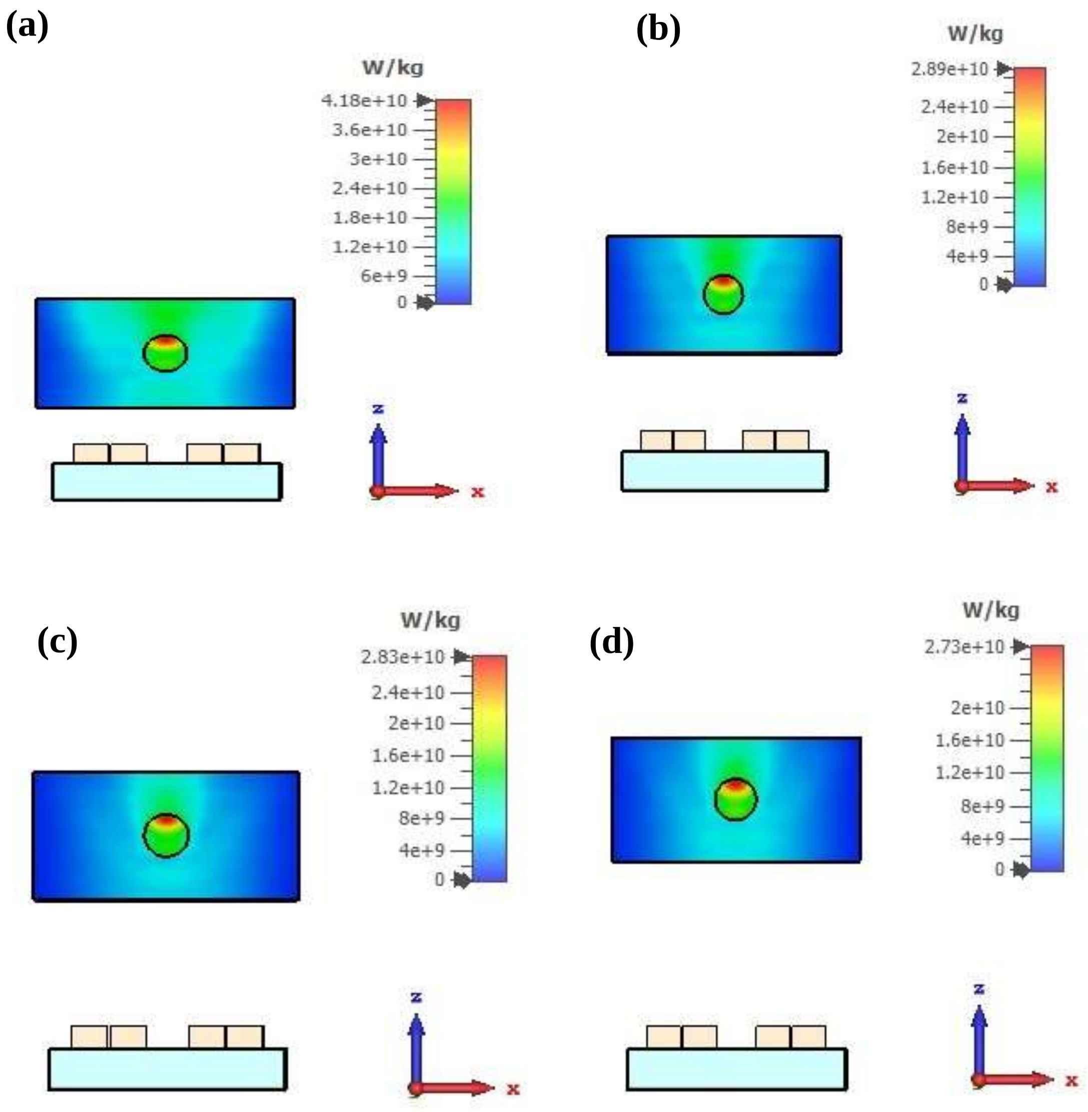

Fig. 3.50 The calculated SAR in the proposed tumor tissue subjected to (2×2) half wavelength array NAs at different distances (a) 100 nm, (b) 200 nm, (c) 300 nm and (d) 400 nm.

The value of the point SAR for an array (3×3) at half wavelength is shown in Fig. 3.46 was different in value when increased the distance from the tissue. It is about (4.78×10^{11}, 4.27×10^{11}, 3.06×10^{11}, and 2.66×10^{11}) W/Kg for distance (100, 200, 300 and 400) nm respectively.

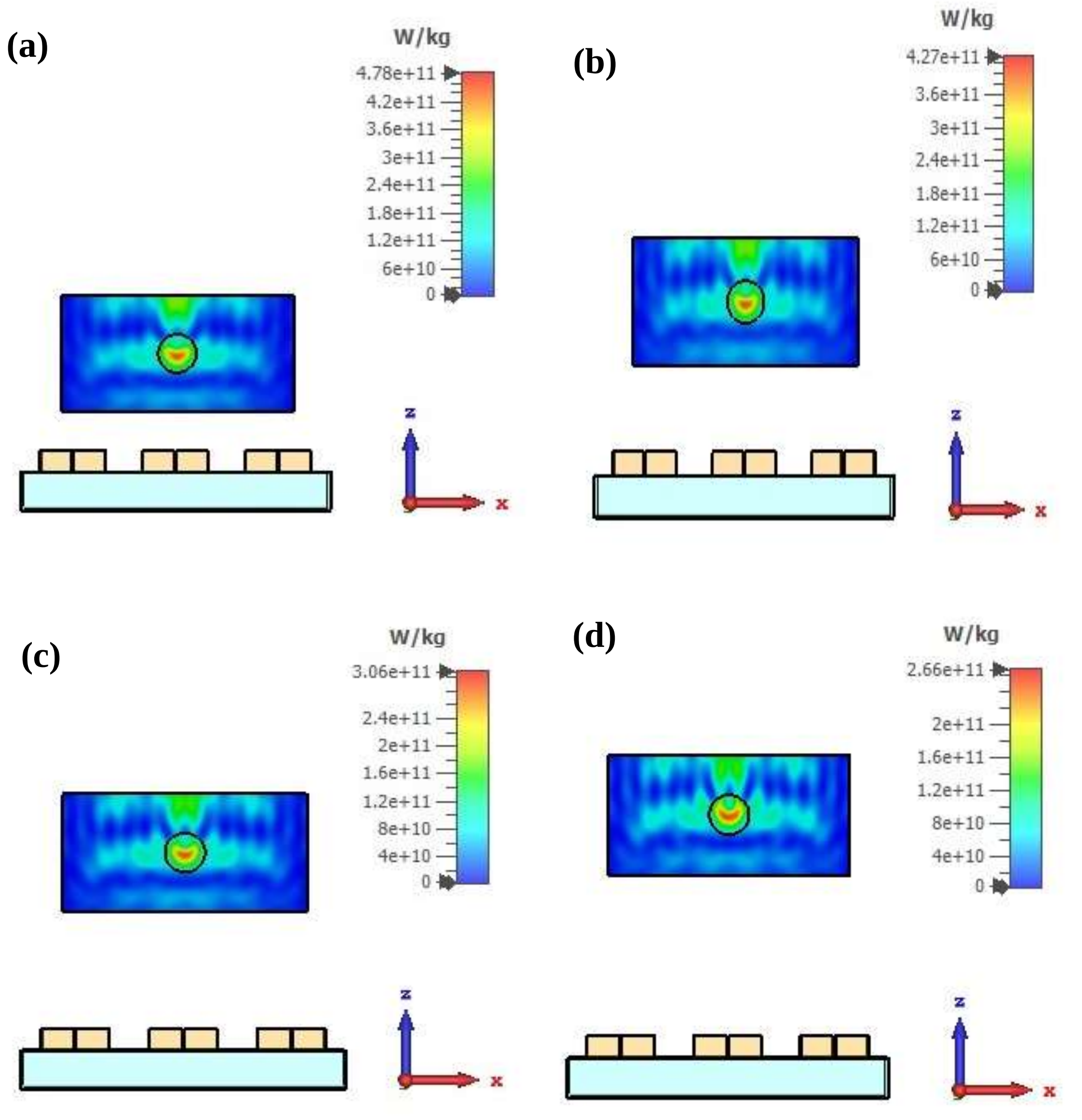

Fig. 3.51 The calculated SAR in the proposed tumor tissue subjected to (3×3) half wavelength array NAs at different distances (a) 100 nm, (b) 200 nm, (c) 300 nm and (d) 400 nm.

The increasing number of an array to (4×4) as shown in Fig 3.52 indicated the value of the point SAR was different (5.31×10^{11}, 3.6×10^{11}, 2.81×10^{11} and 2.75×10^{11}) W/Kg with increasing the distances (100, 200, 300, and 400) nm.

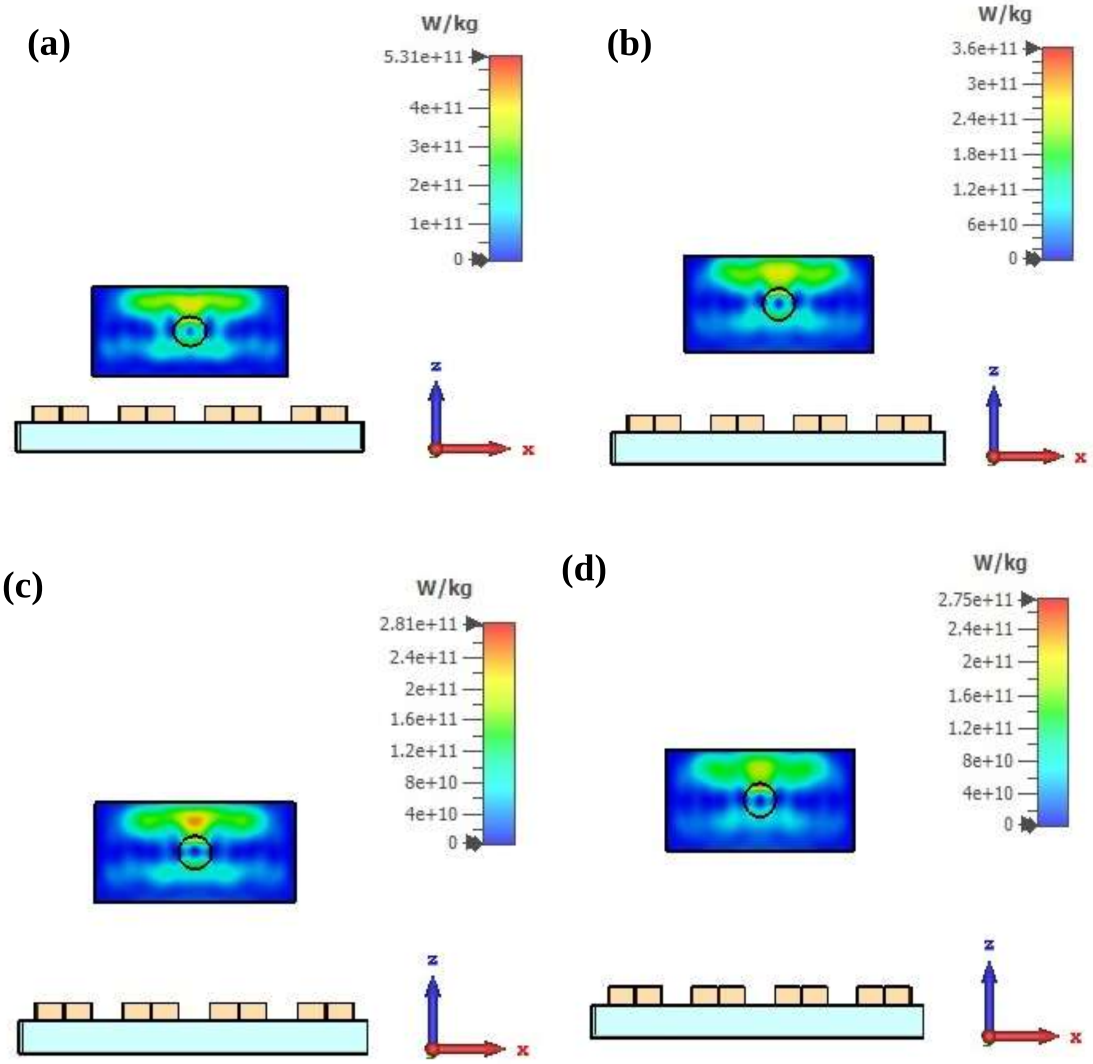

Fig. 3.52 The calculated SAR in the proposed tumor tissue subjected to (4×4) half wavelength array NAs at different distances (a) 100 nm, (b) 200 nm, (c) 300 nm and (d) 400 nm.

The SAR observed in the three cases (2×2, 3×3, 4×4) half wavelength array NAs is varied and dependent on the number of the array used and the type of the tissue proposed with distance separation.

Figure 3,53 illustrates the SAR behavior at different distances at half wavelength of 532 nm. Although the SAR decreases as the distances increases but it is clear that , it is independent neither on the distance nor on the number of arrays.

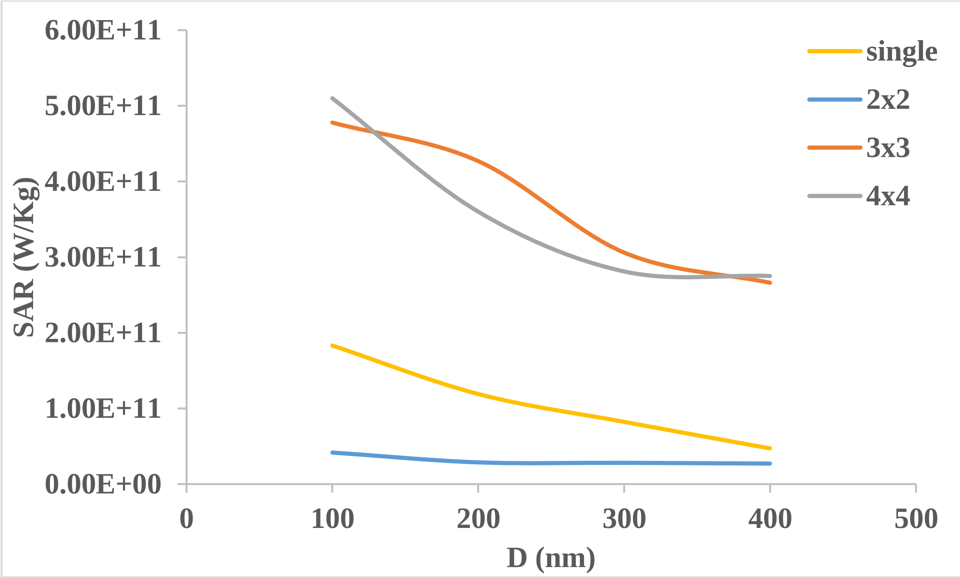

Fig. 3. 53 The SAR behavior as a function of the distance for all design arrays at half wavelength for 532 nm.

3.5.6 Specific absorption rate calculations for (2×2, 3×3 and 4×4) half wavelength array nano-antennas at 1064 nm

The second resonance wavelength (1064 nm) is also investigated, we observe from Figs. 3.54, 3.55, and 3.56 the maximum point SAR in the tumor exposed to the half wavelength array NAs (2×2, 3×3 and 4×4).

The calculation value in Fig 3.54 of the point SAR in the case (2×2) was decreased as the distance from tissue increased the maximum value of point SAR are (2.42×10^{11}, 1.82×10^{11}, 1.55×10^{11}, and 1.48×10^{11}) W/Kg for distances (100, 200, 300 and 400) nm respectively.

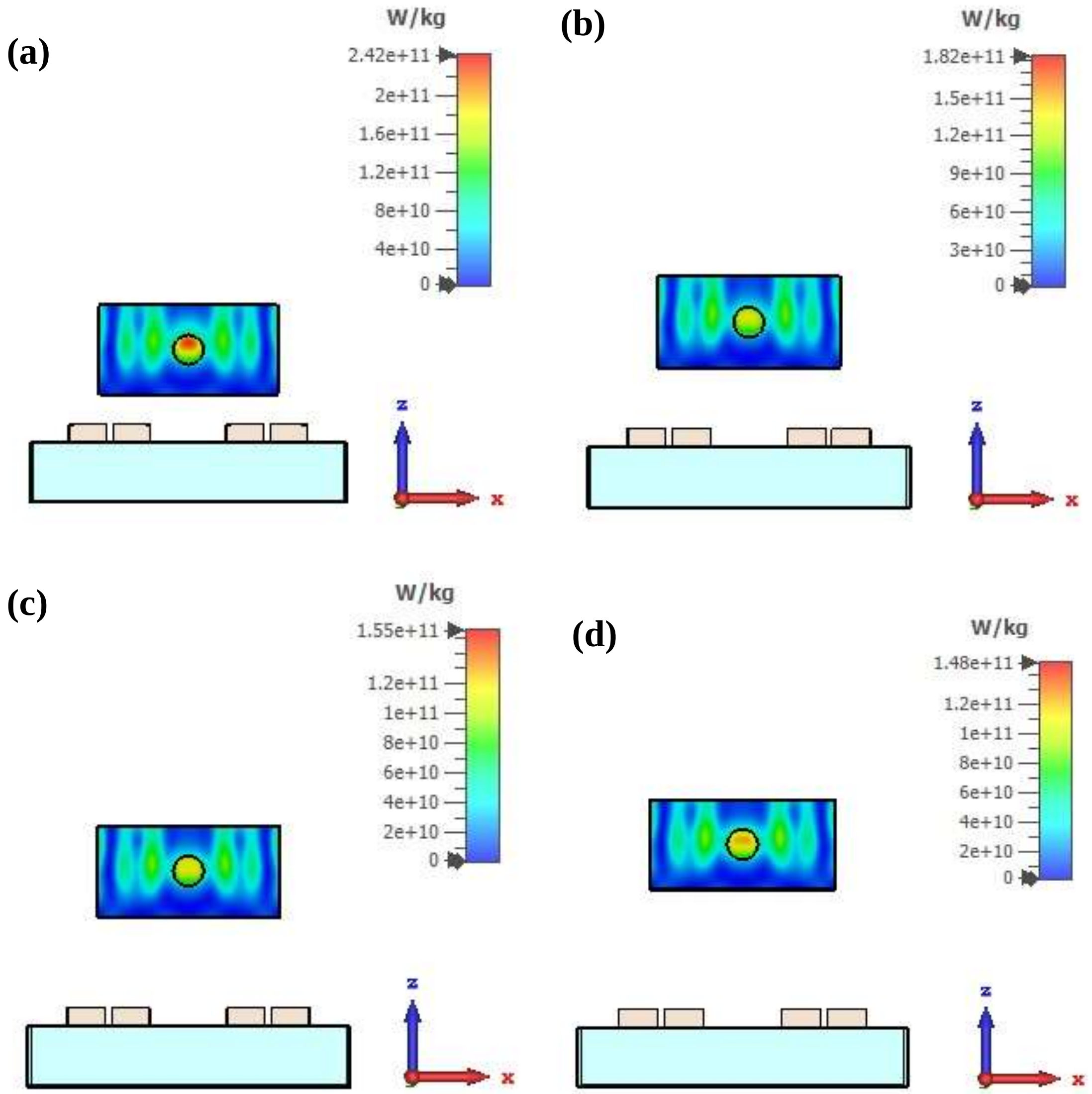

Fig. 3.54 The calculated SAR in the proposed tumor tissue subjected to (2×2) half wavelength array NAs at different distances (a) 100 nm, (b) 200 nm, (c) 300 nm and (d) 400 nm.

Figure 3.55 illustrates the maximum point SAR in the proposed tumor tissue for different distances, it showed that SAR value in case of (3×3) was decreased (4.47×10^{11}, 2.34×10^{11}, 1.65×10^{11}, and 1.5×10^{11}) W/Kg with increased the distance from 100 to 400 nm.

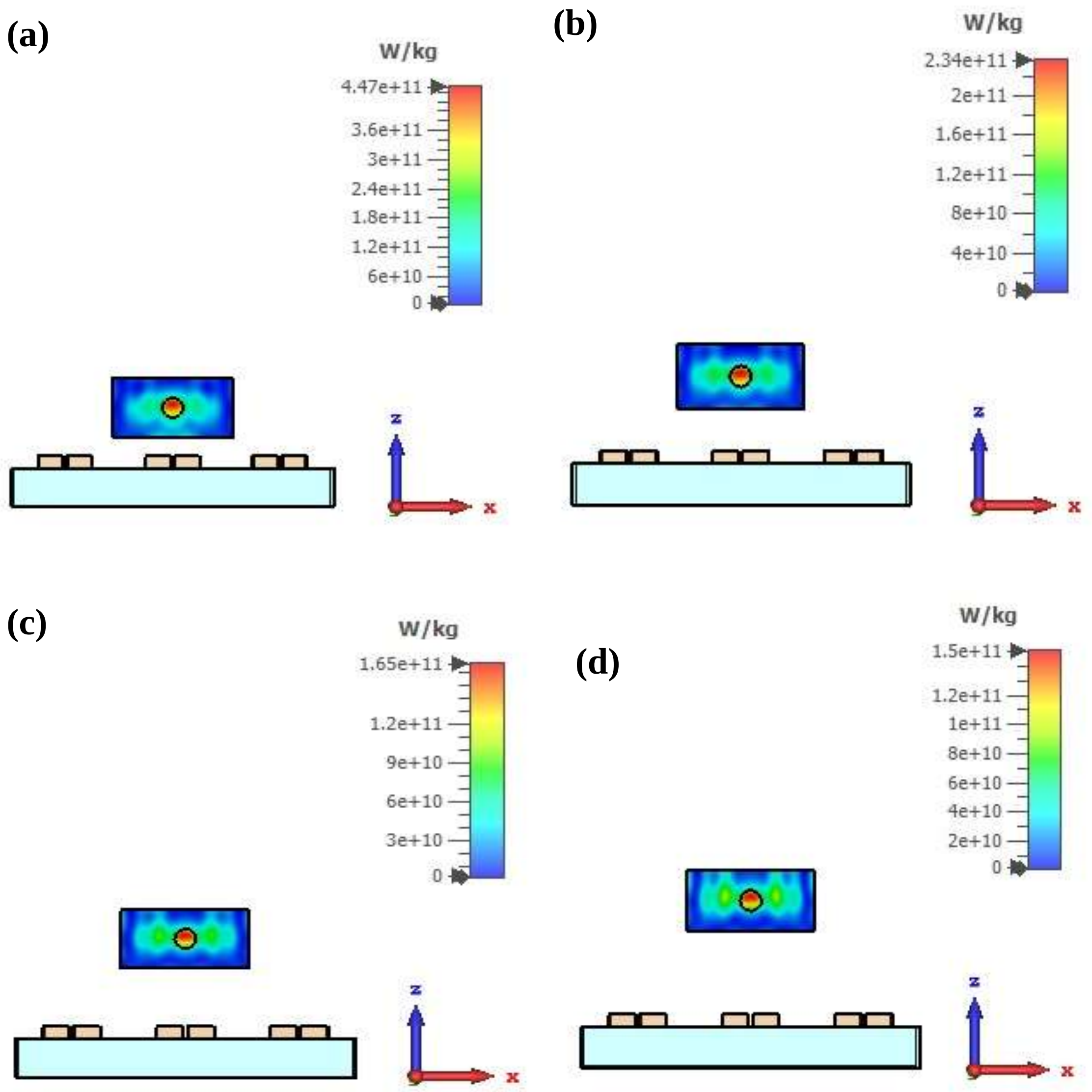

Fig. 3.55 The calculated SAR in the proposed tumor tissue subjected to (3×3) half wavelength array NAs at different distances (a) 100 nm, (b) 200 nm, (c) 300 nm and (d) 400 nm.

Figure 3.56 shows the point SAR when increased the number of the array to (4×4) in the proposed tumor (1.8×10^{11}, 1.19×10^{11}, 1.11×10^{11}, and 1×10^{11}) W/Kg for distances (100, 200, 300 and 400) nm respectively.

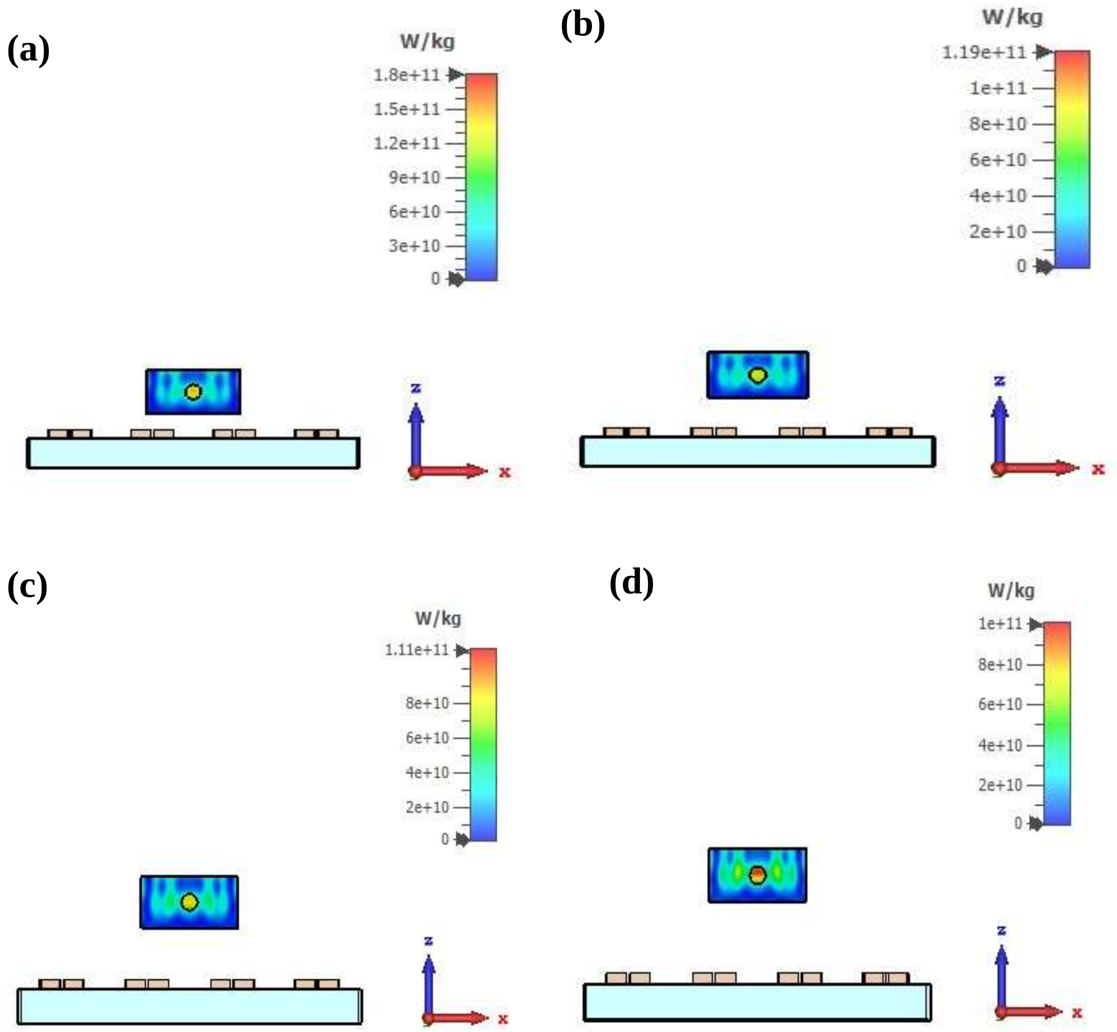

Fig. 3.56 The calculated SAR in the proposed tumor tissue subjected to (4×4) half wavelength array NAs at different distances (a) 100 nm, (b) 200 nm, (c) 300 nm and (d) 400 nm.

The calculation point SAR in the case of half wavelength array NA (2×2, 3×3 and 4×4) improved the SAR in the proposed tissue was dependent on the number of an array and distance separation from the tissue.

In the case of an array that used with a single tumor cell as illustrated previously showed the variation in the value and the distribution of the SAR in the proposed tissue which gives an indication for the variation in the temperature of the tumor.

To compare the array structures with single unit at half wavelength of 1064 nm, the behavior is not far from that detected at half wavelength of 532 nm.

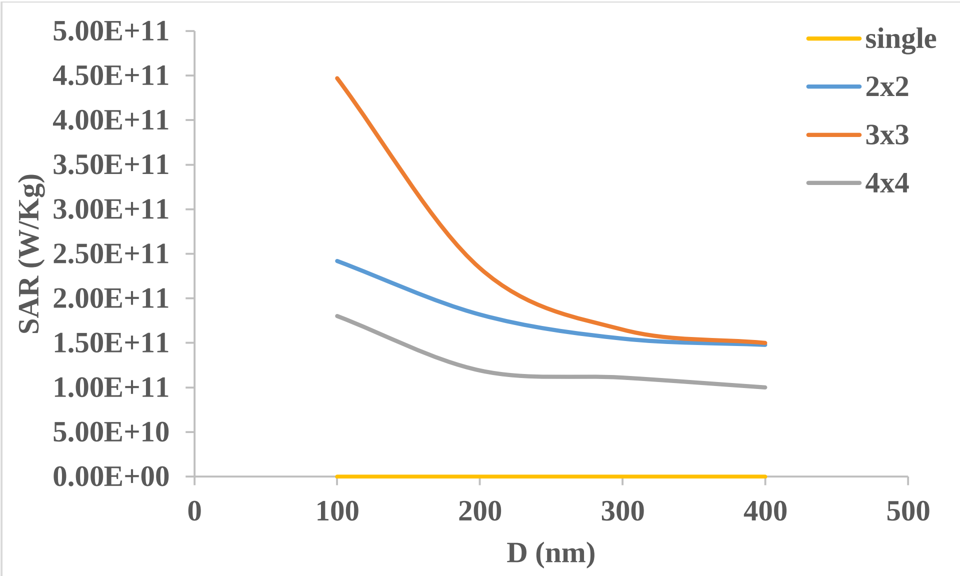

Fig. 3.57 The SAR calculations as a function of the distance for all design arrays for 1064 nm at half wavelength.

The results of SAR calculation proved that the recent results are more than that published by [83] where they stated that the NIR resonance wavelength is better than mm-wave region that generates less SAR.

3.6 Time period estimation

The temperature elevation in the irradiated tissues could be estimated easily related to the SAR calculations owing to equation (1.24). It is noticed from this equation that the temperature elevation in the tissue is depending mainly on the time period of exposing to NAs for a certain SAR, so the time period should be selected carefully to verify the wanted temperature for tumor cells killing.

3.6.1 Time period estimation in tumor tissue at single nano-antenna

The main goal of the treatment of the tumors is the temperature rise over the normal level to cause cells damage which could be estimated by (60^{o} C). Table (3.4) represents the time period estimation to attain the required temperature in the proposed tumor tissue for single NA at two wavelengths (532 and 1064) nm for different distances (100, 200, 300 and 400) nm from the tissue. It is clear that the time period is shorter for closer distance from the tissue for both wavelengths while it shortest for longer wavelength (1064 nm). It is observed from the results that the time period is varied related to the field distribution in the tissue and how much regular and hence for SAR calculation.

Table 3.4 The calculation of the time period in the proposed for distances (100, 200, 300 and 400) at two wavelengths (532 and 1064) nm for single nano-antenna.

Distance D (nm)	Time period (μs)	
	532 nm	**1064 nm**
100	6.55	5.26
200	10.1	10.2
300	14.6	14.1
400	25.4	14.8

3.6.2 Time period in proposed tumor for an array nano-antenna

The next step is to investigate the effect of the (2×2, 3×3 and 4×4) an array NAs in the two wavelengths (532, and 1064) nm on the tumor. The time period is calculated for three arrays (2×2, 3×3 and 4×4) regarding their SAR calculation as illustrated in Table (3.5). The obtain results showed that the time period is increased as the distance of NAS from the tissue which expected due to the reduction in the power intensity field. It is worth to mention that the main issue of an array NAs is the resonance wavelength shift which affects directly on the absorption and as a result on the impinging field in the tissue and hence the variation in the time period while in single NA the resonance wavelength is similar to the incident.

Table 3.5 The calculation of the time period in the proposed for distances (100, 200, 300 and 400) at two wavelengths (532 and 1064) nm for an array nano-antenna.

No. of an array	Distance D (nm)	Time period (μs)	
		532 nm	1064 nm
2×2	100	1.42	6.41
	200	1.45	10.3
	300	1.59	13.5
	400	1.67	14.0
3×3	100	2.34	9.15
	200	2.92	14.6
	300	3.05	15.9
	400	3.54	16.5
4×4	100	1.47	10.3
	200	1.92	22.2
	300	2.33	22.9
	400	2.58	23.2

Number of arrays does not affect on the calculated time period where the longer is detected for the array (3×3) while the shorter time was for an array (2×2) which gives an indication that the important role is for the distance and the SAR value. Also, it is observed that the time period is shorter for (532 nm) than (1064 nm) which ensures the role of the resonance wavelength and the absorption. In comparison to single NA, the calculated time period is much shorter in the array structure which could be attributed to the accumulation field of more than one unit in addition to the distribution of their field in the tissue. It is important to mention that the time period (in the case of 1064 nm) is increased as the number of an array increased where the low number of an array (2×2) needs shortest time to reach the temperature that destroys the tumor cells.

3.6.3 Time period in proposed tissue for half wavelength array nano-antenna

The time period behavior for the structure of half wavelength array NAs is considered also. Table (3.6) illustrates the calculation time period at half wavelength array NAs (2×2, 3×3 and 4×4) of two wavelengths (532 and 1064) nm at distances (100, 200, 300 and 400) nm. It is well observed that the time period is varied at all where it is much longer for an array (2×2) in 532 nm while shorter for 1064 nm, in addition, no clear variation for other arrays (3×3 and 4×4).

Table 3.6 The calculation of the time period in the proposed for distances (100, 200, 300 and 400) at two wavelengths (532 and 1064) nm for half wavelength an array nano-antenna.

No. of an array	Distance D (nm)	Time period (μs)	
		half 532 nm	**half 1064 nm**
2×2	100	28.7	4.95
	200	41.5	6.59
	300	42.4	7.73
	400	43.9	8.10
3×3	100	2.51	2.68
	200	2.81	5.12
	300	3.92	7.27
	400	4.51	7.99
4×4	100	2.35	6.66
	200	3.33	10.1
	300	4.27	10.8
	400	4.36	12.0

In general, the shortest period is detected for the array (3×3) at 1064 nm which means clearly again that the array number does not the main effective parameter due these results are related to the calculated SAR. In comparison for the used structures (single, an array, half wavelength array) ANs the time period is shorter for an array (2×2) NAs at 532 nm for all structures while the shorter is for half wavelength array (3×3) NAs at 1064 nm which mean the half wavelength structure does not improve the time at 532 nm while it is enhanced for 1064 nm.

It is worth to mention that the short time period is quite important in the treatment of the diseased tumor cells because of the generated heat does not dissipated to the surrounding healthy tissues, for this reason the calculated time period in this study does not possible unless using the laser either in pule mode or in chopped mode.

CHAPTER FOUR

Conclusions and Suggestions for Future Works

4.1 Conclusions

Plasmonic Bowtie nanoantennas are designed for both single and array structures at two resonance wavelengths (532, 1064) nm then applied to a proposed skin tissue with a certain environment. The temperature elevation in the tissues is evaluated to estimate its ability to use it as an effective tool for destroying the cancer cells. From the extracted results, it could be concluded:-

- The design parameters have a mutual effect on each other at various rates but the length of antennas seems the higher influence.
- The design of the single antenna showed higher reflectivity at the resonance wavelength 532 nm because it matches the peak absorption of the gold.
- The reflectivity is varied for array designs for both wavelengths at similar antennas dimensions depending on the number of arrays but when the half wavelength distance between two gap antennas is regarded, the resonance is shifted in spite of the enhancement of the reflectivity profile.
- Higher near field intensity is detected for single NA at 532 nm than for 1064 nm while the near-field is improved for the resonance wavelength 1064 nm more than 532 nm using pair of array antennas regarding the variation of the antennas dimensions toward half wavelength distance between two adjacent antennas.
- Array and half wavelength array structures produced higher near field intensity that that of a single unit.
- The detected far-field intensity is higher for 532 nm in single NA and a clear improvement for array NAs even using half wavelength considering the resonance wavelength shift.

- The distribution of the intensity field in the skin tissues is directly influenced by the resonance wavelength and hence its strength.
- The closest distance of different structures to the treated tissue the better field distribution that raises the temperature.
- The SAR results are higher for short distance (100 nm) according to the field intensity distribution in the tissue.
- The required time period is depending on the SAR taken into account the required temperature for killing tumor cells.
- Shorter time period is found for both array and half wavelength array than for single unit at two wavelengths but at different rates.
- It is finally concluded that this technique is encouraged to be an effective therapy for destroying the cancer cells.

4.2 Suggestions for future work

The recent subject is interested in the medical field so that to be practical and available for users, it needs so many steps, we can mention some of them:-

- The recommended structure of single or array antennas should be fabricated.
- This technique needs the application for a live case.
- Other resonance wavelengths could be investigated related to the absorption depth of tissues.
- The heat transfer process needs further investigation due to its importance to estimate the temperature elevation.
- The distribution of the field in the live tissue should be considered during the growth of the cancer cells.
- The shape design of the proposed tissue could taken into account to be close to the real tumor tissue.

REFERENCES

References

[1] Y. -F. C. Chau, C. -T. C. Chao, J. -Y. Rao, H. -P. Chiang, C. M. Lim, R. C. Lim and N. Y. Voo, “Tunable Optical Performances on a Periodic Array of Plasmonic Bowtie Nanoantennas with Hollow Cavities,” *Nanoscale Res. Lett.*, vol. 11, no. 1, p. 411, Sep. 2016.

[2] V. Giannini, A. I. Fernández-Domínguez, S. C. Heck, and S. A. Maier, “Plasmonic Nanoantennas: Fundamentals and Their Use in Controlling the Radiative Properties of Nanoemitters,” *Chem. Rev.*, vol. 111, no. 6, p. 3888–3912, Jun. 2011.

[3] P. J. Schuck, D. P. Fromm, A. Sundaramurthy, G. S. Kino, and W. E. Moerner, “Improving the Mismatch between Light and Nanoscale Objects with Gold Bowtie Nanoantennas,” *Phys. Rev. Lett.*, vol. 94, no. 1, p. 017402, Jan. 2005.

[4] N. Yu, E. Cubukcu, L. Diehl, D. Bour, S. Corzine, J. Zhu, G. Höfler, K. B. Crozier, and F. Capasso, “Bowtie plasmonic quantum cascade laser antenna,” Opt. Express, vol. 15, no. 20, p. 13272–13281, Oct. 2007.

[5] Y. -F. Chau, H.-H. Yeh, and D. P. Tsai, “A New Type of Optical Antenna: Plasmonics Nanoshell Bowtie Antenna with Dielectric Hole,” *J. Electromagn. Waves Appl.*, vol. 24, no. 11–12, p. 1621–1632, Jan. 2010.

[6] D. K. Gramotnev, A. Pors, M. Willatzen, and S. I. Bozhevolnyi, “Gap-plasmon nanoantennas and bowtie resonators,” *Phys. Rev. B*, vol. 85, no. 4, p. 045434, Jan. 2012.

[7] C. -C. Hu, W. Yang, Y. -T. Tsai, and Y. -F. Chau, “Gap enhancement and transmittance spectra of a periodic bowtie nanoantenna array buried in a silica substrate,” *Opt. Commun.*, vol. 324, p. 227–233, Aug. 2014.

[8] M. A. Garcia, “Surface plasmons in metallic nanoparticles: fundamentals and applications,” *J. Phys. Appl. Phys.*, vol. 44, no. 28, p. 283001, Jun. 2011.

[9] D. Guo, G. Xie, and J. Luo, “Mechanical properties of nanoparticles: basics and applications,” *J. Phys. Appl. Phys.*, vol. 47, no. 1, p. 013001, Dec. 2013.

[10] H. Raether, *Surface Plasmons on Smooth and Rough Surfaces and on Gratings*. Berlin Heidelberg: Springer-Verlag, 1988.

[11] W. L. Barnes, A. Dereux, and T. W. Ebbesen, “Surface plasmon subwavelength optics,” *Nature*, vol. 424, no. 6950, p. 824–830, Aug. 2003.

[12] M. Dragoman and D. Dragoman, “Plasmonics: Applications to nanoscale terahertz and optical devices,” *Prog. Quantum Electron.*, vol. 32, no. 1, p. 1–41, Jan. 2008.

[13] S. A. Maier, M. L. Brongersma, P. G. Kik, S. Meltzer, A. a. G. Requicha, and H. A. Atwater, “Plasmonics—A Route to Nanoscale Optical Devices,” *Adv. Mater.*, vol. 13, no. 19, p. 1501–1505, 2001.

[14] A. G. Schuchinsky, “Surface plasmons in noble metal films,” *Metamaterials*, vol. 4, p. 61–69, Aug. 2010.

[15] A. Ahmadivand and S. Golmohammadi, “Surface plasmon resonances and plasmon hybridization in compositional Al/Al2O3/SiO2 nanorings at the UV spectrum to the near infrared region (NIR),” *Opt. Laser Technol.*, vol. 66, p. 9–14, Mar. 2015.

[16] A. Noual, A. Akjouj, Y. Pennec, J.-N. Gillet, and B. Djafari-Rouhani, “Modeling of two-dimensional nanoscale Y-bent plasmonic waveguides with cavities for demultiplexing of the telecommunication wavelengths,” *New J. Phys.*, vol. 11, no. 10, p. 103020, Oct. 2009.

[17] S. Pillai, K. R. Catchpole, T. Trupke, and M. A. Green, “Surface plasmon enhanced silicon solar cells,” *J. Appl. Phys.*, vol. 101, no. 9, p. 093105, May 2007.

[18] J. N. Anker, W. P. Hall, O. Lyandres, N. C. Shah, J. Zhao, and R. P. Van Duyne, “Biosensing with plasmonic nanosensors,” *Nat. Mater.*, vol. 7, no. 6, p. 442–453, Jun. 2008.

[19] J. Henzie, M. H. Lee, and T. W. Odom, “Multiscale patterning of plasmonic metamaterials,” *Nat. Nanotechnol.*, vol. 2, no. 9, p. 549–554, Sep. 2007.

[20] O. Brzobohaty, M. Siler, J. Trojek, L. Chvatal, V. Karasek, A. Patak, Z. Pokorna, F. Mika and P. Zemanek. “Three-Dimensional Optical Trapping of a Plasmonic Nanoparticle using Low Numerical Aperture Optical Tweezers,” *Sci. Rep.*, vol. 5, p. 8106, Jan. 2015.

[21] Y. Li, T. Wen, R. Zhao, X. Liu, T. Ji, H. Wang, X. Shi, J. Shi, J. Wei, Y. Zhao, X. Wu, and G. Nie, “Localized electric field of plasmonic nanoplatform enhanced photodynamic tumor therapy,” *ACS Nano*, vol. 8, no. 11, p. 11529–11542, Nov. 2014.

[22] M. A. Mackey, M. R. K. Ali, L. A. Austin, R. D. Near, and M. A. El-Sayed, “The Most Effective Gold Nanorod Size for Plasmonic Photothermal Therapy: Theory and In Vitro Experiments,” *J. Phys. Chem. B*, vol. 118, no. 5, p. 1319–1326, Feb. 2014.

[23] Z. J. Coppens, W. Li, D. G. Walker, and J. G. Valentine, “Probing and controlling photothermal heat generation in plasmonic nanostructures,” *Nano Lett.*, vol. 13, no. 3, p. 1023–1028, Mar. 2013.

[24] H. T. Ngo, H. N. Wang, A. M. Fales, and T. Vo-Dinh, “Plasmonic SERS biosensing nanochips for DNA detection.,” *Anal. Bioanal. Chem.*, vol. 408, no. 7, p. 1773–1781, Mar. 2016.

[25] J. T. Hugall and J. J. Baumberg, "Demonstrating Photoluminescence from Au is Electronic Inelastic Light Scattering of a Plasmonic Metal: The Origin of SERS Backgrounds," *Nano Lett.*, vol. 15, no. 4, p. 2600–2604, Apr. 2015.

[26] E. Ozbay, "Plasmonics: merging photonics and electronics at nanoscale dimensions," *Science*, vol. 311, no. 5758, p. 189–193, Jan. 2006.

[27] Z. Zalevsky and I. Abdulhalim, *Integrated Nanophotonic Devices*. William Andrew, 2010.

[28] R. G. Chambers, *Electrons in Metals and Semiconductors*. Springer Netherlands, 1990.

[29] *Optical Properties of Solids*, Second Edition. Oxford, New York: Oxford University Press, 2010.

[30] A. Ahmadivand, "Plasmonic Nanoplatforms for Biochemical Sensing and Medical Applications," *FIU Electron. Theses Diss.*, Jan. 2018.

[31] D. Dregely, R. Taubert, J. Dorfmüller, R. Vogelgesang, K. Kern, and H. Giessen, "3D optical Yagi–Uda nanoantenna array," *Nat. Commun.*, vol. 2, p. 267, Apr. 2011.

[32] A. M. Ghanim, M. Hussein, M. F. O. Hameed, A. Yahia, and S. S. A. Obayya, "Highly Directive Hybrid Yagi-Uda Nanoantenna for Radition Emission Enhancement," *IEEE Photonics J.*, vol. 8, no. 5, p. 1–12, Oct. 2016.

[33] A. V. Kildishev, J. D. Borneman, K.-P. Chen, and V. P. Drachev, "Numerical Modeling of Plasmonic Nanoantennas with Realistic 3D Roughness and Distortion," *Sensors*, vol. 11, no. 7, p. 7178–7187, Jul. 2011.

[34] L. Novotny and N. van Hulst, "Antennas for light," *Nat. Photonics*, vol. 5, no. 2, p. 83–90, Feb. 2011.

[35] P. Mühlschlegel, H.-J. Eisler, O. J. F. Martin, B. Hecht, and D. W. Pohl, "Resonant optical antennas," *Science*, vol. 308, no. 5728, p. 1607–1609, Jun. 2005.

[36] T. H. Taminiau, R. J. Moerland, F. B. Segerink, L. Kuipers, and N. F. van Hulst, "λ/4 Resonance of an Optical Monopole Antenna Probed by Single Molecule Fluorescence," *Nano Lett.*, vol. 7, no. 1, p. 28–33, Jan. 2007.

[37] P. Ghenuche, S. Cherukulappurath, T. H. Taminiau, N. F. van Hulst, and R. Quidant, "Spectroscopic mode mapping of resonant plasmon nanoantennas," *Phys. Rev. Lett.*, vol. 101, no. 11, p. 116805, Sep. 2008.

[38] A. Kinkhabwala, Z. Yu, S. Fan, Y. Avlasevich, K. Müllen, and W. E. Moerner, "Large single-molecule fluorescence enhancements produced by a bowtie nanoantenna," *Nat. Photonics*, vol. 3, no. 11, p. 654–657, Nov. 2009.

[39] T. Kalkbrenner, U. Håkanson, A. Schädle, S. Burger, C. Henkel, and V. Sandoghdar, "Optical Microscopy via Spectral Modifications of a Nanoantenna," *Phys. Rev. Lett.*, vol. 95, no. 20, p. 200801, Nov. 2005.

[40] P. Anger, P. Bharadwaj, and L. Novotny, "Enhancement and Quenching of Single-Molecule Fluorescence," *Phys. Rev. Lett.*, vol. 96, no. 11, p. 113002, Mar. 2006.

[41] B. B. Yousif and A. S. Samra, "Modeling of Optical Nanoantennas," *Phys. Res. Int.*, vol. 2012, no. 321075, p. 10, 2012.

[42] Y. Li, D. Li, C. Chi, and B. Huang, "Achieving Strong Field Enhancement and Light Absorption Simultaneously with Plasmonic Nanoantennas Exploiting Film-Coupled Triangular Nanodisks," *J. Phys. Chem. C*, vol. 121, no. 30, p. 16481–16490, Aug. 2017.

[43] H. Fischer and O. J. F. Martin, "Engineering the optical response of plasmonic nanoantennas," *Opt. Express*, vol. 16, no. 12, p. 9144–9154, Jun. 2008.

[44] Z. Li, H. T Hattori1, P. Parkinson, J. Tian, L. Fu, H. H. Tan and C. Jagadish, "A plasmonic staircase nano-antenna device with strong electric field enhancement for surface enhanced Raman scattering (SERS) applications," *J. Phys. Appl. Phys.*, vol. 45, no. 30, p. 305102, Jul. 2012.

[45] Z. Yong, C. Gong, Y. Dong, S. Zhang, and S. He, "Broadband localized electric field enhancement produced by a single-element plasmonic nanoantenna," *RSC Adv.*, vol. 7, no. 4, p. 2074–2080, Jan. 2017.

[46] S. V. Boriskina, L. A. Weinstein, J. K. Tong, W.-C. Hsu, and G. Chen, "Hybrid Optical–Thermal Antennas for Enhanced Light Focusing and Local Temperature Control," *ACS Photonics*, vol. 3, no. 9, p. 1714–1722, Sep. 2016.

[47] G. Baffou, C. Girard, and R. Quidant, "Mapping Heat Origin in Plasmonic Structures," *Phys. Rev. Lett.*, vol. 104, no. 13, p. 136805, Apr. 2010.

[48] G. Chen, "Nonlocal and Nonequilibrium Heat Conduction in the Vicinity of Nanoparticles," *J. Heat Transf.*, vol. 118, no. 3, p. 539–545, Aug. 1996.

[49] M. T. Carlson, A. J. Green, and H. H. Richardson, "Superheating Water by CW Excitation of Gold Nanodots," *Nano Lett.*, vol. 12, no. 3, p. 1534–1537, Mar. 2012.

[50] B. J. Roxworthy, A. M. Bhuiya, V. V. G. K. Inavalli, H. Chen, and K. C. Toussaint, "Multifunctional Plasmonic Film for Recording Near-Field Optical Intensity," *Nano Lett.*, vol. 14, no. 8, p. 4687–4693, Aug. 2014.

[51] W. Ahn, S. V. Boriskina, Y. Hong, and B. M. Reinhard, "Electromagnetic field enhancement and spectrum shaping through plasmonically integrated optical vortices," *Nano Lett.*, vol. 12, no. 1, p. 219–227, Jan. 2012.

[52] S. V. Boriskina and B. M. Reinhard, "Adaptive on-chip control of nano-optical fields with optoplasmonic vortex nanogates," *Opt. Express*, vol. 19, no. 22, p. 22305–22315, Oct. 2011.

[53] W. Ahn, S. V. Boriskina, Y. Hong, and B. M. Reinhard, "Photonic-plasmonic mode coupling in on-chip integrated optoplasmonic molecules," *ACS Nano*, vol. 6, no. 1, p. 951–960, Jan. 2012.

[54] S. V. Boriskina and B. M. Reinhard, "Spectrally and spatially configurable superlenses for optoplasmonic nanocircuits," *Proc. Natl. Acad. Sci.*, vol. 108, no. 8, p. 3147–3151, Feb. 2011.

[55] G. Chen, "Nonlocal and Nonequilibrium Heat Conduction in the Vicinity of Nanoparticles," *J. Heat Transf.*, vol. 118, no. 3, p. 539–545, Aug. 1996.

[56] B. Gallinet, J. Butet, and O. J. F. Martin, "Numerical methods for nanophotonics: standard problems and future challenges," *Laser Photonics Rev.*, vol. 9, no. 6, p. 577–603, Nov. 2015.

[57] K. -Y. Jung, F. L. Teixeira, and R. M. Reano, "Au/SiO_2 Nanoring Plasmon Waveguides at Optical Communication Band," *J. Light. Technol.*, vol. 25, no. 9, p. 2757–2765, Sep. 2007.

[58] H. Gründemann, "Dhatt, G./ Touzot, G., The Finite Element Method, Displayed. Chichester et al., John Wiley & Sons 1984. XV-509 S., £ 18.95. ISBN 0 471 901105," *ZAMM - J. Appl. Math. Mech. Z. Für Angew. Math. Mech.*, vol. 65, no. 7, p. 326–326, 1985.

[59] T. Weiland, “A discretization model for the solution of Maxwell’s equations for six-component fields,” *Arch. Elektron. Uebertragungstechnik*, vol. 31, p. 116–120, Apr. 1977.

[60] M. Clemens and T. Weiland, “Discrete Electromagnetism with the Finite Integration Technique,” *Prog. Electromagn. Res.*, vol. 32, p. 65–87, 2001.

[61] T. Weiland, “Time Domain Electromagnetic Field Computation with Finite Difference Methods,” *Int. J. Numer. Model. Electron. Netw. Devices Fields*, vol. 9, no. 4, p. 295–319, 1996.

[62] D. Wang, D. Tan, and L. Liu, “Particle swarm optimization algorithm: an overview,” *Soft Comput.*, vol. 22, no. 2, p. 387–408, Jan. 2018.

[63] S. S. -Hayward and E. G. -Palacios, “Channel Time Allocation PSO for Gigabit Multimedia Wireless Networks,” *IEEE Trans. Multimed.*, vol. 16, no. 3, p. 828–836, Apr. 2014.

[64] S. Kiranyaz, T. Ince, and M. Gabbouj, *Multidimensional Particle Swarm Optimization for Machine Learning and Pattern Recognition*. Berlin Heidelberg: Springer-Verlag, 2014.

[65] L. Lakshmanan and D. C. Tomar, “OPTIMIZING LOCALIZATION ROUTE USING PARTICLE SWARM-A GENETIC APPROACH,” *Am. J. Appl. Sci.*, vol. 11, no. 3, p. 520–527, Jan. 2014.

[66] C. Grove, *Understanding Skin Cancer*. Australia: Cancer Council, 2016.

[67] S. R. Silpa, Chidvila, and M. Pharmacy, “A REVIEW ON SKIN CANCER,” 2013.

[68] J. L. Roti Roti, “Cellular responses to hyperthermia (40-46 degrees C): cell killing and molecular events,” *Int. J. Hyperth. Off. J. Eur. Soc.*

Hyperthermic Oncol. North Am. Hyperth. Group, vol. 24, no. 1, p. 3–15, Feb. 2008.

[69] N. P. O'Grady, P. S. Barie, J. G. Bartlett, T. Bleck, G. Garvey, J. Jacobi, P. Linden, D. G. Maki, M. Nam, W. Pasculle, M. D. Pasquale, D. L. Tribett, and H. Masur "Practice guidelines for evaluating new fever in critically ill adult patients. Task Force of the Society of Critical Care Medicine and the Infectious Diseases Society of America," *Clin. Infect. Dis. Off. Publ. Infect. Dis. Soc. Am.*, vol. 26, no. 5, p. 1042–1059, May 1998.

[70] J. W. Fisher, S. Sarkar, C. F. Buchanan, C. S. Szot, J. Whitney, H. C. Hatcher, S. V. Torti, C. G. Rylander, and M. N. Rylander, "Photothermal response of human and murine cancer cells to multiwalled carbon nanotubes after laser irradiation," *Cancer Res.*, vol. 70, no. 23, p. 9855–9864, Dec. 2010.

[71] A. Chicheł, J. Skowronek, M. Kubaszewska, and M. Kanikowski, "Hyperthermia – description of a method and a review of clinical applications," *Rep. Pract. Oncol. Radiother.*, vol. 12, no. 5, p. 267–275, Sep. 2007.

[72] D. Jaque, L. M. Maestro, B. del Rosal, P. H.-Gonzalez, A. Benayas, J. L. Plaza, E. M. Rodrıguez and J. G. Sole, "Nanoparticles for photothermal therapies," *Nanoscale*, vol. 6, no. 16, p. 9494–9530, Aug. 2014.

[73] D. Pissuwan, S. M. Valenzuela, and M. B. Cortie, "Therapeutic possibilities of plasmonically heated gold nanoparticles," *Trends Biotechnol.*, vol. 24, no. 2, p. 62–67, Feb. 2006.

[74] Y. Gao and Y. Li, "Gold Nanostructures for Cancer Imaging and Therapy," in *Advances in Nanotheranostics I: Design and Fabrication of Theranosic Nanoparticles*, Z. Dai, Ed. Berlin, Heidelberg: Springer Berlin Heidelberg, p. 53–101, 2016.

[75] G. V. Maltzahn, J. -H. Park, A. Agrawal, N. K. Bandaru, S. K. Das, M. J. Sailor, and S. N. Bhatia, “Computationally Guided Photothermal Tumor Therapy Using Long-Circulating Gold Nanorod Antennas,” *Cancer Res.*, vol. 69, no. 9, p. 3892–3900, May 2009.

[76] Y. -C. Ou, J. A. Webb, S. Faley, D. Shae, E. M. Talbert, S. Lin, C. C. Cutright, J. T. Wilson, L. M. Bellan, and R. Bardhan, “Gold Nanoantenna-Mediated Photothermal Drug Delivery from Thermosensitive Liposomes in Breast Cancer,” *ACS Omega*, vol. 1, no. 2, p. 234–243, Aug. 2016.

[77] K. Tayari, M. Chaoui, H. Ghariani, and M. Lahiani, “Influence of the cardiac activity on the surface impedance of a multilayer model,” in *2014 1st International Conference on Advanced Technologies for Signal and Image Processing (ATSIP)*, p. 340–345, 2014.

[78] J. L. Bolognia, J. L. Jorizzo, and R. P. Rapini, *Dermatology*. Gulf Professional Publishing, Mosby; 1 edition, Jun. 2003.

[79] K. Tayari, H. Werfelli, M. Chaoui, H. Ghariani, and M. Lahiani, “Study of the effects of human tissue on performance of a loop antenna,” *IOSR J. Electr. Electron. Eng.*, vol. 11, no. 04, p. 06–12, Aug. 2016.

[80] Z. Gajinov, M. Matić, S. Prćić, and V. Đuran, “Optical properties of the human skin / Optičke osobine ljudske kože,” *Serbian J. Dermatol. Venereol.*, vol. 2, no. 4, p. 131–136, Dec. 2010.

[81] V. Kumari, G. Sheoran, and T. Kanumuri, “SAR Analysis of Directive Antenna on Anatomically Real Breast Phantoms for Microwave Holography,” *ArXiv190304131 Eess*, Mar. 2019.

[82] M. Nour, M. Bougataya, E. Kengne, K. El Guemhioui, and A. Lakhssassi, “Framework of the Bio-heat Transfer for Laser/Cancer Treatment,” *Int. J. Pharma Med. Biol. Sci.*, vol. 5, no. 4, p. 194–200, Oct. 2016.

[83] T. Hamed and M. Maqsood, “SAR Calculation & Temperature Response of Human Body Exposure to Electromagnetic Radiations at 28, 40 and 60 GHz mmWave Frequencies,” *Prog. Electromagn. Res.*, vol. 73, p. 47–59, 2018.

[84] B. M. Hochwald, D. J. Love, S. Yan, and J. Jin, “SAR codes,” in *2013 Information Theory and Applications Workshop (ITA)*, p. 1–9, 2013.

[85] A. H. Sallomi. “A Theoretical Approach for SAR Calculation in Human Head Exposed to RF Signals,” J. of Engineering and Development, vol. 16, p. 10, 2012.

[86] H. Fischer and O. J. F. Martin, “Engineering the optical response of plasmonic nanoantennas,” *Opt. Express*, vol. 16, no. 12, p. 9144–9154, Jun. 2008.

[87] D. D. Gupta, G. V. Maltzahn, S. Ghosh, S. N. Bhatia, S. K. Das, and S. Chakraborty, “Probing nanoantenna-directed photothermal destruction of tumors using noninvasive laser irradiation,” *Appl. Phys. Lett.*, vol. 95, no. 23, p. 233701, Dec. 2009.

[88] S. V. Boriskina and L. D. Negro, “Multiple-wavelength plasmonic nanoantennas,” *Opt. Lett.*, vol. 35, no. 4, p. 538–540, Feb. 2010.

[89] J. Chen, P. Albella, Z. Pirzadeh, P. A.-Gonzalez, F. Huth, S. Bonetti, V. Bonanni, J. Akerman, J. Nogues, P. Vavassori, A. Dmitriev, J. Aizpurua, and R. Hillenbrand, “Plasmonic Nickel Nanoantennas,” *Small*, vol. 7, no. 16, p. 2341–2347, 2011.

[90] M. Mivelle, T. S. V. Zanten, L. Neumann, N. F. V. Hulst, and M. F. G. -Parajo, “Ultrabright Bowtie Nanoaperture Antenna Probes Studied by Single Molecule Fluorescence,” *Nano Lett.*, vol. 12, no. 11, p. 5972–5978, Nov. 2012.

[91] J. M. Jornet and I. F. Akyildiz, “Graphene-based Plasmonic Nano-Antenna for Terahertz Band Communication in Nanonetworks,” *IEEE J. Sel. Areas Commun.*, vol. 31, no. 12, p. 685–694, Dec. 2013.

[92] Z. J. Coppens, W. Li, D. G. Walker, and J. G. Valentine, “Probing and Controlling Photothermal Heat Generation in Plasmonic Nanostructures,” *Nano Lett.*, vol. 13, no. 3, p. 1023–1028, Mar. 2013.

[93] J. Calderón, J. Alvarez, J. M. -Pastor, and D. Hill, “Bowtie plasmonic nanoantenna arrays for polarimetric optical biosensing,” in *Frontiers in Biological Detection: From Nanosensors to Systems VI*, vol. 8933, p. 89330I, 2014.

[94] Q. Wang, L. Liu, Y. Wang, P. Liu, H. Jiang, Z. Xu, Z. Ma, S. Oren, E. K. C. Chow, M. Lu and L. Dong, “Tunable Optical Nanoantennas Incorporating Bowtie Nanoantenna Arrays with Stimuli-Responsive Polymer,” *Sci. Rep.*, vol. 5, p. 18567, Dec. 2015.

[95] Y. -F. C. Chau, J. -C. Jiang, C. -T. C. Chao, H.-P. Chiang, and C. M. Lim, “Manipulating near field enhancement and optical spectrum in a pair-array of the cavity resonance based plasmonic nanoantennas,” *J. Phys. Appl. Phys.*, vol. 49, no. 47, p. 475102, Nov. 2016.

[96 P. B. Savaliya, A. Thomas, R. Dua, and A. Dhawan, “Tunable optical switching in the near-infrared spectral regime by employing plasmonic nanoantennas containing phase change materials,” *Opt. Express*, vol. 25, no. 20, p. 23755–23772, Oct. 2017.

[97] V. F. Gili, L. Ghirardini, D. Rocco, G. Marino, I. Favero, I. Roland, G. Pellegrini, L. Duò, M. Finazzi, L. Carletti, A. Locatelli, A. Lemaître, D. Neshev, C. De Angelis, G. Leo and M. Celebrano, “Metal–dielectric hybrid nanoantennas for efficient frequency conversion at the anapole mode,” *Beilstein J. Nanotechnol.*, vol. 9, no. 1, p. 2306–2314, Aug. 2018.

[98] E. Sakat, L. Wojszvzyk, J. -P. Hugonin, M. Besbes, C. Sauvan, and J. -J. Greffet, “Enhancing thermal radiation with nanoantennas to create infrared sources with high modulation rates,” *Optica*, vol. 5, no. 2, p. 175–179, Feb. 2018.

[99] M. Hren, C. Campbell, A. Casey, and G. Triplett, “Simulation and design of plasmonic gold bowtie nanoantennas,” in *Nanoscale Imaging, Sensing, and Actuation for Biomedical Applications XVI*, vol. 10891, p. 108910M, 2019.

[100] S. V. Gaponenko, P. -M. Adam, D. V. Guzatov, and A. O. Muravitskaya, “Possible nanoantenna control of chlorophyll dynamics for bioinspired photovoltaics,” *Sci. Rep.*, vol. 9, no. 1, p. 1–14, May 2019.

[101] G. Jayaswal, A. Belkadi, A. Meredov, B. Pelz, G. Moddel, and A. Shamim, “A Zero-Bias, Completely Passive 28 THz Rectenna for Energy Harvesting from Infrared (Waste Heat),” in *2018 IEEE/MTT-S International Microwave Symposium - IMS*, p. 355–358, 2018.

[102] P. Biagioni, J. -S. Huang, and B. Hecht, “Nanoantennas for visible and infrared radiation,” *Rep. Prog. Phys.*, vol. 75, no. 2, p. 024402, Jan. 2012.

[103] M. K. A. Rahim, M. Z. A. Abdul Aziz and C. S. Goh, "Bow-tie microstrip antenna design," *2005 13th IEEE International Conference on Networks Jointly held with the 2005 IEEE 7th Malaysia International Conf on Communic*, Kuala Lumpur, p. 4, 2005.

[104] P. B. Johnson and R. W. Christy, “Optical Constants of the Noble Metals,” *Phys. Rev. B*, vol. 6, no. 12, p. 4370–4379, Dec. 1972.

[105] K. Shurrab, N. Kochaji, and W. Bachir, “Development of Temperature Distribution and Light Propagation Model in Biological Tissue Irradiated by 980 nm Laser Diode and Using COMSOL Simulation,” *J. Lasers Med. Sci.*, vol. 8, no. 3, p. 118–122, Jun. 2017.

الخلاصـــة

يواجــه العــلاج البصــري الحــراري للأنســجة الحيــة عقبــات معقــدة بســبب حــبس مصــادر الضــوء فــي الجانــب وطبيعــة خلايــا الأنســجة فــي مكــان آخــر. يــتم إجــراء محــاولات جــادة للتغلــب علــى هــذه المشــكلة جزئيًــا وخاصــةً اســتخدام الليــزر مباشــرة علــى الأنســجة المريضــة التــي تمثــل التقــدم فــي مجــال التطبيــق هــذا ، لكنهــا لا تــزال مقيــدة بحــدود الحيــود بينمــا أبعــاد الخلايــا فــي مقيــاس طــول الموجــة الفرعيــة. تجــدر الإشــارة إلــى أن الامتصــاص هــو عمــق الاختــراق الــذي يعتمــد علــى نســيج معــين. يعــد الهــوائي النــانوي البلازمــوني مرشــحاً مناســباً نظــراً لقدرتــه علــى توليــد كثافــة بصــرية عاليــة فــي مجــال الأبعــاد النانويــة. وقــد تــم اســتخدام الإصــدار المعبــأ فــي مجموعــة اســتوديو تقنيــات محاكــاة الكمبيــوتر(٢٠١٧، ٢٠١٨ و ٢٠١٩) لتنفيــذ تصــميم كــل مــن الهوائيــات النانويــة والجلــد المقتــرح الانســجة. البنيــة النانويــة الذهبيــة وثــاني أكســيد كربيــد الســيليكون هــي المــادة المســتخدمة فــي تصــميم شــكل ربطــة العنــق. تــم فحــص أطــوال مــوجتين (٥٣٢ و ١٠٦٤) نــانومتر، وهمــا أطــوال موجيــة مــن ليــزر Nd:YAG وثانيهــا التــوافقي لأنهــا تمثــل امتصــاص الجلــد الســطحي والعميــق علــى التــوالي. يشــتمل التصــميم علــى هياكــل مفــردة وأزواج مــن هياكــل صــفيف علــى شــكل ربطــة عنــق لـــ (٢×٢ ،٣×٣ و ٤×٤) ، بالإضــافة إلــى مســافة نصــف طــول موجيــة بــين هوائيــات فجــوة متجــاورة تــم اعتبارهــا أيضًــا لعينــات الصــفيف. تعرضــت جميــع التصــاميم لتحســين ســرب الجســيمات والعمليــات الشــاملة. وتمــت الدراســات المعلميــة لجميــع العينــات المصــممة. يــتم إنجــاز أداء جميــع العينــات بمــا فــي ذلــك الانعكــاس والحقــل القريــب والحقــل البعيــد لكــلا الطــولين المــوجي. تــم تقــدير الفتــرة الزمنيــة فــي الأنســجة المشــعة اللازمــة لقتــل الخلايــا الســـرطانية مـــن خـــلال حســـاب معـــدل الامتصـــاص المحـــدد. أوضـــحت النتـــائج أن أقصـــى انعكاســـية للهـــوائي النـــانوي المحســـن عنـــد الطـــول المـــوجي للـــرنين ٥٣٢ نـــانومتر هـــو (-٥٠,٥٧ ديســيبل)، فــي حــين أن الانعكاســية العليــا هــي (-٥٨,٣٩ ديســيبل) لهوائيــات الطــول المــوجي ، لوحظــت اختلافــات واضــحة للانعكاســات مــع تعزيــز فــي بعــض الصــفائف ولكــن يــتم تغييــر أطــوال موجــات الــرنين. تــم الكشــف عــن تحــول أحمــر مــع انعكــاس أعلــى لمجموعــة مــن أزواج للطــول المــوجي ٥٣٢ نــانومتر وخفضــت لأكثــر مــن زوجــين. كشــفت قياســات المجــال القريــب أن مجــالات الكثافــة هــي أعلــى (٣,٢٧×١٠^٨فولــت / م) عنــد ٥٣٢ نــانومتر للهــوائيين المنفــردة بينمــا فــي هياكــل المصــفوفة ، تكــون شــدة المجــال معــززة أكثــر لصــفيف نصـــف الطـــول المـــوجي (٣×٣) عنـــد ١٠٦٤ نـــانومتر (٧,٤٧×١٠^٨فولـــت / م). لـــوحظ توزيــع الحقــل البعيــد الأكثــر وضــوحاً عنــد ٥٣٢ نــانومتر مــن (٧,٧٩×١٠^٦فولــت / م). تــم

تحسين المجال البعيد لكلا الطولين الموجي باستخدام هياكل الصفيف المتعلقة بوحدة واحدة بينما لوحظ المزيد من التأثير في حالة نصف الطول الموجي (٢,٥٤×١٠^{٧}فولت / م) عند ١٠٦٤ نانومتر. تكون شدة المجال أكثر فاعلية على مسافة أقرب (١٠٠ نانومتر) حيث تكون (١,٣×١٠^{٨}فولت / م) عند ٥٣٢ نانومتر بينما تكون عند صفيف الطول الموجي (٤×٤) (٣,٠٤ ×١٠^{٨}فولت / م) بنصف الطول الموجي. الحد الأقصى لمعدل امتصاص السطح هو (٢,٢×١٠^{١١}واط / كجم) للهوائي الفردي (١٠٠ نانومتر) عند الطول الموجي للرنين ١٠٦٤ نانومتر ويوجد أعلى معدل لهياكل نصف الطول الموجي (٥,٣١ ×١٠^{١١}واط / كجم) عند ٥٣٢ نانومتر. الفترة الزمنية المحسوبة المطلوبة لتدمير خلية الورم تكون أقصر على مسافة أقرب (١٠٠ نانومتر) من الأنسجة. الفترة الزمنية الأقصر للوحدة المفردة هي (٥,٢٦ مايكرو ثانية) عند ١٠٦٤ نانومتر بينما (١,٤٢ مايكرو ثانية) للصفيف (٢×٢) عند ٥٣٢ نانومتر.

وزارة التعليم العالي والبحث العلمي
جـــامـــــعـــــة بـــــغــــداد
مــعهد الليـــزر للدراســـات العليـــا

دراســـة التـدرج الحـراري في الـــورم المعـرض لهوائـــي نانـــوي بمســاعدة الليـــزر

أطـــروحة مــقدمة الـــى

معهد الليزر للدراسات العليا / جامعة بغداد / لاستكمال متطلبات نيل شهادة دكتوراه فلسفة في الليزر/ الهندسة الالكترونية والاتصالات

مــــن قبل

رشـــا هاشـــم مـــهدي

بكالوريوس هندسة الليزر و الالكترونيات البصرية - ٢٠١٠
ماجســـتير هندسة الليزر و الالكترونيات البصرية - ٢٠١٤

بإشـــراف

الأستاذ المساعد الدكتور حســين علـي جــواد

١٤٤٠ هـ **٢٠١٩ م**